

**Single Molecule Investigation of the Structural Aspects and
Mass Transport Dynamics of Mesoporous Silica Nanopores**

By

Ruwandi Kumarasinghe

B.S., University of Peradeniya, Sri Lanka, 2010

AN ABSTRACT OF A DISSERTATION

Submitted in partial fulfillment of the requirements for the degree

DOCTOR OF PHILOSOPHY

**Department of Chemistry
College of Arts and Sciences**

**KANSAS STATE UNIVERSITY
Manhattan, Kansas**

2019

Abstract

This dissertation describes single-molecule tracking (SMT) studies for the quantitative characterization of one-dimensional (1D) solvent-filled surfactant-templated mesoporous silica (STMS) materials and other nanostructured materials, such as double stranded DNA. SMT permits the simultaneous and quantitative assessment of the nanoscale and microscale morphologies and mass-transport properties of the materials with nanometer-scale spatial resolution. The efficiency and selectivity of catalytic reactions and chemical separations occurring in liquid-filled mesoporous materials are governed by the translational and orientational mobilities and surface interactions of the incorporated reagents and analytes. Polarization dependent SMT results demonstrate that the dye molecules used as probes of materials nanostructure are tightly confined within the one-dimensional (1D) pores of surfactant-templated mesoporous silica films. Spectroscopic single molecule tracking (sSMT) data reveal that the hydrophobic probe dyes are confined within nonpolar regions of the nanomaterials.

For this dissertation, surfactant templated mesoporous silica films were prepared by the spin coating of acid catalyzed tetramethoxysilane (TMOS)-based silica sols on glass substrates in the presence of Cetyltrimethylammonium bromide (CTAB). Cylindrical CTAB micelles formed during evaporation of the solvent acted as a structure directing template, forming nanometer-sized one-dimensional pores within the silica films. SMT experiments were performed using a wide-field fluorescence microscope that was sufficiently sensitive to allow detection of the fluorescence from individual dye molecules. A series of perylene diimide (PDI) dyes was employed for basic structural characterization of the silica materials. Single molecule fluorescence was recorded in the form of fluorescence videos. These videos revealed the presence of immobile dye molecules, along with those diffusing in one and two dimensions (1D and 2D). The 1D diffusing molecules provided basic evidence for the confinement mass transport of the dye molecules within the silica mesopores.

Spectroscopic single molecule tracking (sSMT) studies served as an extension of basic SMT experiments and were employed to determine the location of the molecules. The polarity sensitive dye Nile Red (NR) was employed in these studies. It exhibits 1D diffusion, consistent with its confinement to the cylindrical pores, as was also the case for the PDI dyes. The sSMT data revealed that the majority of NR molecules were found in nonpolar environments having polarities similar to that of n-hexane. Single molecule emission polarization (SMEP) measurements were employed to explore the orientational confinement of the dyes. The results of these experiments demonstrated that the PDI and NR molecules diffuse with their long axes aligned parallel to the long axis of the pores. All of the dyes employed were found to be orientationally confined to ~ 1 nm diameter pathways within the pores. The diffusion coefficient for the dyes was also shown to be $\sim 10^3$ -fold smaller than in bulk solution. The results of the NR studies demonstrate that the dye molecules were confined to the hydrophobic cores of the micelles, and provide support for the conclusion that the PDI dyes are similarly confined. These studies afford an enhanced understanding of how nanostructuring of the pore-filling medium in solvent- and surfactant-filled mesoporous materials governs the mass transport and surface interactions of incorporated reagents and analytes.

The dependence of molecular confinement on dye charge and structure was also explored in this dissertation. The confined translational and orientational motions of a series of four different PDI dyes diffusing along one dimension (1D) within individual cylindrical silica mesopores were investigated in these studies. Specifically, the motions of cationic and anionic PDI dyes were compared to those of two uncharged PDIs having different alkane tail lengths. All four dyes exhibited populations that were immobile, along with separate populations that diffused in either 1D or 2D. The anionic and cationic PDI dyes exhibited the largest and smallest populations, respectively, of immobile molecules, suggesting that electrostatic interactions between the charged dyes and the cationic surfactant head groups play a significant role in limiting molecular motion.

The cationic and anionic PDI dyes also exhibit the largest populations of 2D diffusing molecules, suggesting they may more readily pass between the cylindrical micelles and through the silica pore walls. All four dyes also emit strongly polarized fluorescence as they move in 1D, indicating they are orientationally confined within the nanochannels.

Nile Red dye was used to determine the dielectric constant, ϵ , of nonpolar microenvironments in double stranded DNA (ds-DNA) single molecules both in aqueous buffer solution and when adsorbed on amine-modified chemical gradient surfaces. The value of ϵ within the DNA decreased with increasing buffer concentration. Values of $\epsilon \sim 6.75$ and ~ 3.00 were obtained in 0.1 mM phosphate buffered saline (PBS) and in 10 mM PBS, respectively. Similar effects were observed upon adsorption to chemically graded amine-modified silica surfaces. Under 1 mM buffer, ϵ was measured to be ~ 2.84 and ~ 1.90 at the low amine (high silica), and high amine (low silica) ends of the gradient, respectively. An increase in the buffer concentration again led to a decrease in ϵ , but only at the low amine end. It is concluded that high buffer concentrations and binding to an amine surface cause a condensation of the ds-DNA, forming less polar microenvironments within its structure. These results provide important knowledge of the factors governing the polarity of DNA microenvironments to which intercalators bind.

**Single Molecule Investigation of the Structural Aspects and
Mass Transport Dynamics of Mesoporous Silica Nanopores**

By

Ruwandi Kumarasinghe

B.S., University of Peradeniya, Sri Lanka, 2010

A DISSERTATION

Submitted in partial fulfillment of the requirements for the degree

DOCTOR OF PHILOSOPHY

**Department of Chemistry
College of Arts and Sciences**

**KANSAS STATE UNIVERSITY
Manhattan, Kansas**

2019

**Approved by:
Major Professor
Dr. Daniel A. Higgins**

Copyright

© Ruwandi Kumarasinghe 2019.

Abstract

This dissertation describes single-molecule tracking (SMT) studies for the quantitative characterization of one-dimensional (1D) solvent-filled surfactant-templated mesoporous silica (STMS) materials and other nanostructured materials, such as double stranded DNA. SMT permits the simultaneous and quantitative assessment of the nanoscale and microscale morphologies and mass-transport properties of the materials with nanometer-scale spatial resolution. The efficiency and selectivity of catalytic reactions and chemical separations occurring in liquid-filled mesoporous materials are governed by the translational and orientational mobilities and surface interactions of the incorporated reagents and analytes. Polarization dependent SMT results demonstrate that the dye molecules used as probes of materials nanostructure are tightly confined within the one-dimensional (1D) pores of surfactant-templated mesoporous silica films. Spectroscopic single molecule tracking (sSMT) data reveal that the hydrophobic probe dyes are confined within nonpolar regions of the nanomaterials

For this dissertation, surfactant templated mesoporous silica films were prepared by the spin coating of acid catalyzed tetramethoxysilane (TMOS)-based silica sols on glass substrates in the presence of Cetyltrimethylammonium bromide (CTAB). Cylindrical CTAB micelles formed during evaporation of the solvent acted as a structure directing template, forming nanometer-sized one-dimensional pores within the silica films. SMT experiments were performed using a wide-field fluorescence microscope that was sufficiently sensitive to allow detection of the fluorescence from individual dye molecules. A series of perylene diimide (PDI) dyes was employed for basic structural characterization of the silica materials. Single molecule fluorescence was recorded in the form of fluorescence videos. These videos revealed the presence of immobile dye molecules, along with those diffusing in one and two dimensions (1D and 2D). The 1D diffusing molecules provided basic evidence for the confinement mass transport of the dye molecules within the silica mesopores.

Spectroscopic single molecule tracking (sSMT) studies served as an extension of basic SMT experiments and were employed to determine the location of the molecules. The polarity sensitive dye Nile Red (NR) was employed in these studies. It exhibits 1D diffusion, consistent with its confinement to the cylindrical pores, as was also the case for the PDI dyes. The sSMT data revealed that the majority of NR molecules were found in nonpolar environments having polarities similar to that of n-hexane. Single molecule emission polarization (SMEP) measurements were employed to explore the orientational confinement of the dyes. The results of these experiments demonstrated that the PDI and NR molecules diffuse with their long axes aligned parallel to the long axis of the pores. All of the dyes employed were found to be orientationally confined to ~ 1 nm diameter pathways within the pores. The diffusion coefficient for the dyes was also shown to be $\sim 10^3$ -fold smaller than in bulk solution. The results of the NR studies demonstrate that the dye molecules were confined to the hydrophobic cores of the micelles, and provide support for the conclusion that the PDI dyes are similarly confined. These studies afford an enhanced understanding of how nanostructuring of the pore-filling medium in solvent- and surfactant-filled mesoporous materials governs the mass transport and surface interactions of incorporated reagents and analytes.

The dependence of molecular confinement on dye charge and structure was also explored in this dissertation. The confined translational and orientational motions of a series of four different PDI dyes diffusing along one dimension (1D) within individual cylindrical silica mesopores were investigated in these studies. Specifically, the motions of cationic and anionic PDI dyes were compared to those of two uncharged PDIs having different alkane tail lengths. All four dyes exhibited populations that were immobile, along with separate populations that diffused in either 1D or 2D. The anionic and cationic PDI dyes exhibited the largest and smallest populations, respectively, of immobile molecules, suggesting that electrostatic interactions between the charged dyes and the cationic surfactant head groups play a significant role in limiting molecular motion.

The cationic and anionic PDI dyes also exhibit the largest populations of 2D diffusing molecules, suggesting they may more readily pass between the cylindrical micelles and through the silica pore walls. All four dyes also emit strongly polarized fluorescence as they move in 1D, indicating they are orientationally confined within the nanochannels.

Nile Red dye was used to determine the dielectric constant, ϵ , of nonpolar microenvironments in double stranded DNA (ds-DNA) single molecules both in aqueous buffer solution and when adsorbed on amine-modified chemical gradient surfaces. The value of ϵ within the DNA decreased with increasing buffer concentration. Values of $\epsilon \sim 6.75$ and ~ 3.00 were obtained in 0.1 mM phosphate buffered saline (PBS) and in 10 mM PBS, respectively. Similar effects were observed upon adsorption to chemically graded amine-modified silica surfaces. Under 1 mM buffer, ϵ was measured to be ~ 2.84 and ~ 1.90 at the low amine (high silica), and high amine (low silica) ends of the gradient, respectively. An increase in the buffer concentration again led to a decrease in ϵ , but only at the low amine end. It is concluded that high buffer concentrations and binding to an amine surface cause a condensation of the ds-DNA, forming less polar microenvironments within its structure. These results provide important knowledge of the factors governing the polarity of DNA microenvironments to which intercalators bind.

Table of Contents

List of Figures.....	xiv
List of Tables.....	xxi
Acronyms and Definitions.....	xxii
Variables and Descriptions.....	xxiv
Acknowledgements	xxv
Dedication.....	xxvii
Chapter 1 - General Introduction.....	1
1.1 Mesoporous Silica Materials.....	1
1.2 Single Molecule Tracking Methods Applied to Mesoporous Silica.....	4
1.3 Objectives and Motivations of the Present Research.....	6
1.4 Overview of Thesis.....	8
Chapter 2 -Mass Transport and Nano-Structure of Surfactant-Templated Mesoporous Silica Materials.....	11
2.1 Surfactant-Templated Mesoporous Silica.....	12
2.1.1 Properties and Applications of Mesoporous Silica.....	13
2.1.2 Silica Sol-Gel Process.....	14
2.1.3 Evaporation Induced Self Assembly.....	16
2.2 Properties of Nanoconfined Solvents.....	18
2.3 Mass Transport in Nanostructured Materials.....	20
Chapter 3 – Optical, Microscopic, and Single Molecule Methods for Investigating Mass Transport in Nanostructured Materials.....	22
3.1 Ensemble Methods for Mass Transport Nanostructured Materials.....	22
3.2 Single-Molecule Methods for Mass Transport Studies.....	24
3.3 Single-Molecule Fluorescence Methods.....	24

3.3.1 Wide-Field Fluorescence Video Microscopy and Single Molecule Tracking (SMT).....	26
3.3.1.1 Single Molecule Emission Polarization (SMEP).....	29
3.3.1.2 Spectroscopic Single Molecule Tracking (sSMT).....	31
Chapter 4 - Experimental Considerations.....	33
4.1 Preparation of Surfactant-Templated Mesoporous Silica: Formation of the Hexagonal Mesophase.....	33
4.2 Perylene Diimide (PDI) Dyes.....	35
4.3 Nile Red Dye and its Solvatochromic Properties.....	36
4.4 Instrumentation.....	38
4.4.1 Wide-Field Fluorescence Microscopy.....	38
4.5 Single Molecule Trajectory Analysis.....	39
4.5.1 Orthogonal Regression.....	39
4.5.2 Trajectory Angle Order Parameter.....	42
4.5.3 Emission Polarization Measurements.....	44
Chapter 5 - Spectroscopic and Polarization-Dependent Single-Molecule Tracking Reveal the One-Dimensional Diffusion Pathways in Surfactant-Templated Mesoporous Silica.....	47
5.1 Introduction.....	47
5.2 Experimental Section.....	50
5.2.1 Sample Preparation.....	50
5.2.2 Quantum Mechanical Calculations.....	51
5.2.3 Partition Coefficient Measurements.....	53
5.2.4 Monte Carlo Simulations.....	53
5.2.5 Single Molecule Tracking.....	54

5.2.6 Trajectory Analysis.....	56
5.2.7 Assessing Molecular Mobility and Dimensionality of Motion.....	56
5.3 Results and Discussion.....	57
5.3.1 Spectroscopic Single Molecule Tracking (sSMT).....	57
5.3.2 Single Molecule Emission Polarization (SMEP) Studies.....	66
5.3.3 Monte Carlo Simulations of Nile Red in a Model Silica Pore.....	69
5.4 Conclusion.....	72
Chapter 6 - Single-Molecule Tracking Studies of Charged and Neutral Perylene Diimide Probes within Surfactant-Filled Silica Mesopores Reveal Differences in Mass Transport Behavior and Orientational Confinement.....	73
6.1 Introduction.....	73
6.2 Experimental Section.....	76
6.2.1 Sample Preparation.....	76
6.2.2 Single Molecule Tracking.....	77
6.2.3 Trajectory Analysis.....	78
6.3 Results.....	78
6.3.1 Populations of Mobile and Immobile Molecules.....	83
6.3.2 Rate of Molecular Motion.....	85
6.3.3 Molecule Confinment.....	87
6.3.4 Mechanistic Insights into Single-Molecule Diffusion.....	89
6.4 Conclusion.....	92
Chapter 7 - Probing the Local Dielectric Constant of Plasmid DNA in Solution and Adsorbed on Chemically Graded Aminosilane Surfaces.....	93
7.1 Introduction.....	93
7.2 Experimental Section.....	95

7.2.1 Chemicals and Materials.....	95
7.2.2 Sample Preparation	96
7.2.3 Gradient Characterization.....	97
7.2.4 AFM Imaging of DNA.....	98
7.2.5 Single Molecule Tracking	99
7.2.6 Calibration of Nile Red Response.....	100
7.3 Results and Discussion.....	101
7.3.1 Gradient Preparation and Characterization.....	101
7.3.2 AFM Imaging of Surface-Adsorbed Plasmid DNA.....	102
7.3.3 Dielectric Constant Measurements for Plasmid DNA in Solution.....	103
7.3.4 Dielectric Constant Measurements for Surface-Adsorbed Plasmid DNA.....	106
7.4 Conclusion	110
Chapter 8 - General Conclusions and Future Directions.....	111
8.1 General Conclusions	111
8.2 Future Directions.....	116
References.....	118

List of Figures

- Figure 2.1** General mechanisms of hydrolysis and condensation of alkoxy silane precursors to form silica under (a) acid catalyzed conditions and (b) base catalyzed conditions. **Copyright © 2013, Royal Society of Chemistry.**⁹²15
- Figure 2.2** Structures of mesoporous M41S materials: a) MCM-41 (2D hexagonal, space group *p6mm*), b) MCM-48 (cubic, space group *Ia3̄d*), and c) MCM-50 (lamellar, space group *p2*). **Copyright © 2006 WILEY-VCH Verlag GmbH & Co. KGaA, Weinheim.**⁹⁵17
- Figure 2.3** Formation of mesoporous materials by structure-directing agents: a) true liquidcrystal template mechanism, b) cooperative liquid crystal template mechanism. **Copyright © 2006 WILEY-VCH Verlag GmbH & Co. KGaA, Weinheim.**⁹⁵18
- Figure 2.4** Model for partitioning and mass transport (e.g., diffusion) in solvent-filled 1D nanoporous media such as solvent and surfactant filled mesoporous silica.....20
- Figure 3.1** Common components often found in wide-field microscopes. Some optics have been omitted for simplicity. Abbreviations: CCD, charge-coupled device.....27
- Figure 3.2** Common components often found in SMEP wide-field microscopes setup.....29
- Figure 3.3** SMEP images acquired simultaneously in two orthogonal polarizations for Nile Red-doped CTAB-template mesoporous silica films. The images depict the maximum signal level observed at each pixel across the 200 frame long videos. **Copyright © 2016, American Chemical Society.**¹⁴⁶30
- Figure 3.4** Common components often found in sSMT wide-field microscopes setup.....31
- Figure 3.5** sSMT images acquired simultaneously in (a) 625nm and (b) 580 nm wavelength detection channels for Nile Red-doped CTAB-template mesoporous silica films. The images depict the maximum signal level observed at each pixel across the 200 frame long videos. **Copyright © 2016, American Chemical Society.**¹⁴⁶32

Figure 4.1 Chemical structures of (left) CTAB and (right) TMOS.....	33
Figure 4.2 The ternary CTAB/water/ethanol phase diagram ¹⁰¹ . The sol compositions were adjusted to form hexagonal mesophase in phase diagrams.....	35
Figure 4.3 Molecular structures;	
(a.) N,N'- bis(octyloxypropyl)perylene-3,4,9,10-tetracarboxylic diimide	36
(b.) N,N'-bis(methoxypropyl)perylene-3,4,9,10-tetracarboxylic diimide.....	36
(c.) N,N'-bis(3-sulfonatopropyl)perylene-3,4,9,10-tetracarboxylic diimide,.....	36
(d.) N,N'-bis(2-(trimethylammonio)ethyl)-perylene-3,4,9,10-tetracarboxylic diimide.....	36
Figure 4.4.a Nile Red molecular structure and intramolecular charge transfer process.....	37
4.4.b. Fluorescence spectra of NR in hexane (red), heptanes (orange), cyclohexane (yellow), toluene (dark green), chloroform(light green), dichloromethane (dark blue), acetone (light blue), and acetonitrile (dark purple) obtained with a 488-nm excitation. Copyright © 2013, American Chemical Society ⁴²	37
Figure 4.5 Wobbling motion of dye molecule inside a nanochannel.....	45
Figure 5.1 Nile Red structure. The red arrow depicts the orientation of the transition dipole for the lowest energy electronic transition. The transition dipole deviates from the long molecular axis (black line) by only $\sim 7^\circ$. The molecular axis was identified by fitting the atomic positions using orthogonal regression methods. Copyright © 2016, American Chemical Society ¹⁴⁶	51
Figure 5.2 (a) Optimized geometry of the Nile Red molecule. (b) HOMO representation for Nile Red. (c) LUMO and LUMO+1 representations. The lowest energy electronic transition in Nile Red is characterized primarily as a HOMO to LUMO and LUMO+1 transition. Copyright © 2016, American Chemical Society ¹⁴⁶	53
Figure 5.3 Nile Red emission ratio $(I_{625} - I_{580})/(I_{625} + I_{580})$ as a function of the CM factor for a series of ethanol/hexane mixtures. These data were acquired on the same microscope and	

employed the same filter sets as the single molecule data. The data points show average values and standard deviations obtained from five replicate measurements performed on three separate days. From the left, the solution compositions are 0%, 2%, 3%, 5%, 10%, 15%, 20%, 40%, 60%, 80%, and 100% ethanol (by volume), with the remainder being hexane. The NR concentration in each case was 2 μ M. **Copyright © 2016, American Chemical Society** ¹⁴⁶58

Figure 5.4 (a,b) Z-projection images showing Nile Red motions in a surfactant-templated mesoporous silica film for the 625 and 580 nm detection channels. The video data are provided as Supporting Information. A prevalence of 1D single molecule motions is observed. (c) Single molecule trajectories obtained by tracking the molecules in the same videos. The trajectories are color coded to reflect the emission ratio $(I_{625} - I_{580}) / (I_{625} + I_{580})$ and CM factor along each trajectory. **Copyright © 2016, American Chemical Society** ¹⁴⁶59

Figure 5.5 (a,b) Emission ratios and CM factors as a function of position for each of two representative 1D trajectories. (c,d) The same values plotted as a function of time for an immobile molecule (0D) and a 2D diffusing molecule, respectively. The insets in each panel show the trajectories. The scale bars in each inset are 125 nm in length. The 1D trajectories were rotated to appear horizontal for ease of plotting. All data were taken from Figure 5.3. **Copyright © 2016, American Chemical Society** ¹⁴⁶60

Figure 5.6 (a–c) Single frame emission ratios and CM factors for immobile (0D), 1D, and 2D diffusing molecules, respectively. The solid black lines show fits of the main populations to Gaussian functions. **Copyright © 2016, American Chemical Society** ¹⁴⁶62

Figure 5.7 Plots of mean square displacement data (symbols) for the four single molecule trajectories shown in Figure 5.5 and their fits (straight lines). The filled circles and squares show data from Figure 5.5a,b while the open circles and squares show data from Figure

5.5c,d. Each data set is plotted out to a 20 frame (~ 1.9 s) delay. **Copyright © 2016, American Chemical Society** ¹⁴⁶64

Figure 5.8. (a,b) Z-projection images depicting Nile Red motions in a surfactant-templated mesoporous silica film. The original video data were acquired for the orthogonal emission polarizations designated by the white double-ended arrows. The video is provided as Supporting Information. (c) Single molecule trajectories obtained by tracking the molecules in the same video. The trajectory colors designate immobile (blue), 1D diffusing (red), and 2D diffusing (green) molecules. These data demonstrate that a large fraction of the NR molecules diffuse in 1D, and that these molecules are confined to diffuse with their long molecular axes oriented approximately parallel to the long axis of each pore. **Copyright © 2016, American Chemical Society** ¹⁴⁶67

Figure 5.9 (a,b) Histograms showing the distribution of mean wobbling angles and the same data replotted as the orientational order parameter $\langle P2 \rangle$, respectively, for NR, as derived from Figure 5.8. **Copyright © 2016, American Chemical Society** ¹⁴⁶69

Figure 5.10 (a) Model ~3.5 nm diameter silica pore employed in Monte Carlo simulations of NR orientation. A representative NR molecule is shown within the otherwise empty pore. Silicon atoms are shown in orange, oxygen in red, hydrogen in white, carbon in gray, and nitrogen in blue. (b) Results of the Monte Carlo simulations for NR (data points) in the pore shown in (a). The results are displayed as the orientational order parameter (eq 5.4), as a function of radial position from the pore center. Molecules near the center of the pore are almost randomly oriented, while those near the pore wall are preferentially aligned parallel to the pore axis. The error bars depict the 95% confidence intervals about the mean value at each point. These were obtained by splitting the full population of accepted configurations into 10 subgroups to estimate the standard deviation of replicate simulations. **Copyright © 2016, American Chemical Society** ¹⁴⁶70

Figure 6.1. Z-projections of Widefield fluorescence images acquired simultaneously in two orthogonal polarizations for (A) (B) C₄OPDI (D)(E) TAPDI²⁺ (C)(G) PDISO₃²⁻. These images show the predominance of 1D diffusive motion observed for all Dye molecules, and the strong polarization of their emission parallel to the direction of motion. Double-ended arrows designate the detected polarizations. (C) (F)(I) Images are the trajectory plots for each C₄OPDI, TAPDI²⁺, PDISO₃²⁻ video images.79

Figure 6.2. Representative single molecule trajectories and MSD plots for (a) 2D molecule in blue circle (b) 1D molecule in red circles (c) Immobile molecule in triangles.81

Figure 6.3 (A) Representative Trajectory plot showing immobile, 1D diffusion, 2D diffusion molecules (B) Representative single molecule trajectories showing one molecule moving along the $\phi \sim 30^\circ$ 82

Figure 6.4 Mean relative population of immobile (Red), 1D diffusing (Green) and 2D diffusing (Blue) molecules. The error bars depict the 95% confidence intervals for each value.83

Figure 6.5. Histograms showing the distribution of measured D values for 1D diffusing molecules. The solid lines depict the Gaussian fits to each histogram used to determine the peak of the distribution.86

Figure 6.6. Distribution of wobbling angles for C₄OPDI, C₁₁OPDI, TAPDI²⁺, and PDISO₃²⁻ dyes exhibiting 1D motion. The solid lines depict Gaussian fits to the distributions.88

Figure 6.7. Representative single-molecule trajectories (A) and (B) and stepsize distributions obtained from these trajectories (C) and (D) respectively. Blue lines depict fits to Eq 6.6, and black line depicts to Eq. 6.7. Results are attributed to Fickian diffusion in (C) and anomalous diffusion in (D).91

Figure 7.1 Calibration of the NR spectroscopic response to environments having different dielectric constants. The plot shows the NR emission ratio E in bulk solution for a series of hexane-ethanol mixtures. The polarity of each solution is defined by its Clausius-

Mossotti (CM) factor $(\epsilon-1)/(2\epsilon+1)$. From the left, the solution compositions are 0, 2, 3, 5, 10, 15, 20, 40, 60, 80 and 100% ethanol. The NR concentration was 2 μM in each case. The solid line shows a linear fit to the data; the slope and intercept were used to interpret the imaging results obtained from NR doped single plasmid DNA molecules. **Copyright American Chemical Society**.....100

Figure 7.2 A) Sessile drop water contact angle along the amine gradient surface. No contact angle data could be obtained from the steepest region because the water droplets spontaneously moved towards the low amine end of the gradient. B) Spectroscopic ellipsometry data showing the thickness of the TMOS-derived base layer (blue symbols) and the aminosilane gradient (red symbols). Gradient thickness was obtained by subtracting the base layer thickness from the full film thickness. The positions along the X-axis in the two panels are not identical but indicate similar positions to $\sim \pm 1$ mm. The solid lines are fits to sigmoidal functions and have been added only to better show the trends in the data. **Copyright American Chemical Society**.....101

Figure 7.3 AFM images of A) supercoiled and B) relaxed plasmid DNA on APTMOS-coated mica. Plasmid DNA was deposited from 1 mM Tris-HCl solutions also containing 1 mM MgCl_2 . **Copyright American Chemical Society**.....103

Figure 7.4 Solution phase E values (right axis) and CM factors (left axis) obtained from Nile Red in supercoiled (red symbols) and relaxed (blue symbols) plasmid DNA. The error bars depict the 95% confidence intervals for each value. **Copyright American Chemical Society**.....105

Figure 7.5 Two-color fluorescence images of NR-doped A) supercoiled and B) relaxed plasmid DNA adsorbed at the high amine end (6 mm position) of an APTMOS-derived gradient. These images were acquired under 2.5 mM pH ~ 7.2 PBS buffer. The color scale for both

images is the same and depicts photon counts up to 1000 counts/pixel. **Copyright American Chemical Society**.....108

Figure 7.6 A) CM factor and B) dielectric constant for Nile Red doped supercoiled (red points) and relaxed (blue triangles) plasmid DNA as a function of position along APTMOS-derived gradients, and as a function of buffer concentration. All DNA molecules analyzed were adsorbed on the gradient surface. The 6 mm position represents the high amine end, with decreasing amine coverage towards the 12 mm position. The error bars show the 95% confidence intervals for each value. **Copyright American Chemical Society**.....109

List of Tables

Table 5.1 Electronic transitions of Nile Red obtained from GAMESS modeling using the 6-31G basis set. ^a Energy is given in eV, ^b wavelength is in nm and ^c transition dipoles in Debye. ^d The first transition represents the transition probed in the spectroscopic and single-molecule experiments.....	52
Table 5.2 Lennard-Jones parameters for all pore atoms. ²⁶	54
Table 5.3 Lennard-Jones parameters for all NR atoms. ²⁶	54
Table 6.1 Calculated 1D and 2D diffusion coefficients for all four dyes.....	86

Acronyms and Definitions

1D/2D/3D	One/Two/Three dimensional
CTAB	Cetyltrimethylammonium bromine
EM	Electron microscopy
EM CCD	Electron multiplying charge-coupled device
APD	Avalanche photo diode
FCS	Fluorescence correlation spectroscopy
LCT	Liquid crystal templating
MSD	Mean square displacement
NA	Numerical aperture
NMR	Nuclear magnetic resonance
PDI	Perylene diimide
NR	Nile red
PDMS	Poly(dimethylsiloxane)
DNA	Deoxyribonucleic acid
dsDNA	Double-stranded deoxyribonucleic acid
PBS	Phosphate-buffered saline
APTMS	3-aminopropyltrimethoxysilane
VPD	Vapor phase deposition
WCA	Water contact angle
FTIR	Fourier transform infrared
SAXS	Small angle X-ray scattering
SMT	Single-molecule tracking
SMEP	Single molecule emission polarization

sSMT	Spectroscopic single molecule tracking
FRAP	Fluorescence-recovery after photobleaching
S/N	Signal-to-noise
CM	Clausius-Mossotti
TEM	Transmission electron microscopy
TIRF	Total internal reflection fluorescence
TMOS	Tetramethoxysilicate
XRD	X-ray diffraction
AFM	Atomic force microscopy
STMS	Surfactant-templated mesoporous silica

Variables and Descriptions

β	Angle of the trajectory segment with respect to the horizontal direction
$\bar{\beta}$	Mean trajectory orientation in a given sample region
$\Delta\beta$	Angular deviation in the direction of the individual trajectories, β from $\bar{\beta}$
δi	Error in measuring the position of the molecule
σ	(Chapter 4) Gaussian functions and their widths of SAXS anisotropy data
σ	(Chapter 5.3.2) Localization precision
σ	(Chapter 5.3.4) Lateral detection volume dimensions of the FCS measurement
σ_{δ}^2	Variance in the position measurement for each molecule along each trajectory
σ_R^2	Motional variance in the molecular position
θ	Angle of the trajectory segment with respect to the horizontal direction
θ	(Chapter 4) X-ray scattering angle
$\bar{\theta}$	Mean trajectory orientation in a given sample region
$\Delta\theta$	Angular deviation in the direction of the individual trajectories, θ from $\bar{\theta}$
χ	Azimuthal angle
a	Pixel size
A	The spot amplitude
b^2	Background noise obtained from the rolling-ball background subtraction step
N	Total number of photon counts in the spot area
S	Gaussian width of the detected spot
S_{yy}	Arithmetic mean of squared y_i
S_{xx}	Arithmetic mean of squared x_i
S_{xy}	Arithmetic mean of the product of y_i
x_i	Measured x position of a single molecule spot in the video frames
X_i	The best estimate of the actual x position of the molecule
y_i	Measured y position of a single molecule spot in the video frames

Acknowledgements

First of all, I would like to express my sincere gratitude and appreciation to my major advisor Dr. Daniel Higgins. He helps me complete the Ph.D. degree with constant guidance and endless encouragements during the last six years as a graduate student in the Department of Chemistry at Kansas State University. I highly appreciate the constant academic guidance, valuable advice in my research work, endless hours spent on the revision of my paper drafts, seminar abstracts, written proposals, and final thesis. Dr.Higgins is an excellent professor with a wide range of knowledge and tireless dedication to scientific research. I feel fortunate to have had the opportunity to work and learn under such an excellent advisor and patience mentor.

I am also greatly thankful for my co-advisor Dr. Takasi Ito for providing critical analysis and valuable suggestions on my works. Because of his great advice, I was able to achieve gradual progress in my research. I am thankful for Dr. Ito for being a member of my committee at the preliminary examinations and Ph.D. defense.

I am also very blessed to have such a wonderful Ph.D. committee consisting of Dr. Christopher Culbertson, Dr. Kristan Corwin, and Dr. Keith Hohn. Thank you all for being a member of my committee at the preliminary examinations and Ph.D. defense.

I am very thankful to have my previous and current students and friends of the Higgins group. Dr. Rajib Pramanik and Dr. Khanh-Hoa Tran-Ba are especially acknowledged for the time on showing me all the tricks to use the wide-field microscope. Also, Dr. Seok Chan Park, Dr. Dipak Giri, Dr. Hao Xu and Zi Li for their valuable contribution and their good influences on my Ph.D. studies. I also thank Judith Bautista for interesting discussions on research and daily topics. I am very grateful for the friendship and support from all the past and current members of the Ito group.

I also express my deepest gratitude at the faculty and staff of the Department of Chemistry at Kansas State University. I would like to acknowledge Ron Jackson, Tobe Eggers and Jim Hodgson for their help in the instrumental troubleshooting and in designing experimental

necessities for my research. I also acknowledge U.S. Department of Energy the funding support for our research projects.

Finally, my sincere gratitude to my family and friends. I am grateful for my parents and my sister for their constant support and unconditional love. Most importantly the patience, understanding, encouragement, and support of my loving husband Javed Miandad during the entire Ph.D. program. I am also thankful for all my friends in the U.S. especially Pabodha Galgamuwa, Pavithra Sajeewani, Kushan Weerasinghe and Dimuthu Weerawardene. The experience as a graduate student would not have been that exciting and productive without all of the love, care and support of all my family and friends.

Dedication

To my loving husband Javed Miandad, my caring sister Erandi Nisansala and especially
my proud parents Julius Kumarasinghe & Rani Swarnalatha.

Chapter 1 - General Introduction

1.1 Mesoporous Silica Materials

Mesoporous materials are distinctive nanostructured materials containing nanostructured pores with a characteristic dimension of 2-50 nm.^{3,106} They have attracted great attention especially because of their unique properties such as ordered pore structures, very high specific surface areas and their possible synthesis in a wide range of morphologies (spheres, rods, discs, powders, etc.). The compound producing mesoporous silica was produced in around 1970. (R1) In the 1990s, researchers in Japan first reported surfactant-templating methods.^{1,64} Mesoporous silica materials were later produced at Mobil Corporation laboratories, and named Mobil Crystalline Materials (MCM).^{1,64} The surfactant-templating method employs the well-established sol-gel-process, in which the hydrolysis and condensation of inorganic oxide precursors (e.g., alkoxysilanes) in the presence of structure-directing agents such as surfactant micelles lead to the formation of porous surfactant-templated mesoporous materials.

Most importantly, the use of different synthesis conditions allows for various morphologies (e.g., nanoparticles, monoliths, and films) and porosities of mesoporous silica to be obtained. The morphology and porosity of mesoporous silica materials are determined by the mesophase of the structure-directing agent (i.e., the structure and organization of the surfactant micelles). By changing parameters such as the silica-surfactant-water ratio, nature, and concentration of catalyst and any subsequent processing conditions, different mesophases can be formed. These include 2D hexagonal ($p6m$ space group), 3D cubic ($Ia3d$), and lamellar($p2$) mesoporous materials that are also known as MCM-41, MCM-48, and MCM-50 materials, respectively.

These materials were invented mainly for use as molecular sieves due to their porous structure. Over the years, researchers were able to discover many unique properties of these materials such as high surface area, tunable pore volume, controlled morphology, surface functionalization, and biocompatibility. In the past few decades, due to such unique properties,

these materials have influenced many fields of research and industrial groups in areas such as catalysis, chemical separations, ion exchange, molecular sieving, optical materials, and low dielectric materials.⁹⁻¹⁴ Mesoporous silica containing unidirectional pore arrays throughout the material have been successfully exploited as templates for semiconductor materials formed from the gas phase.⁶⁵⁻⁶⁹ Recently, a novel supercritical fluid solution-phase based approach to producing silicon nanowires within the pores of mesoporous silica has also been reported.⁷⁰ Hexagonally organized cylindrical mesoporous silica materials with open pores lead to the development of potential applications in the fields of catalysis, chemical separations, and drug carriers for selective drug delivery systems. Mesoporous silicas have been used as catalytic nanoreactors for the synthesis of conductive polymers,⁶⁵⁻⁶⁹ and as templates for the growth of certain carbon nanostructures such as nanotubes, nanowires, and mesoporous carbon materials.⁷⁰ Silica membranes have been proposed as potential candidates for separation applications. They are advantageous for rapid diffusion of molecules, can be modified in a variety of ways, and have high chemical and thermal stability, thus allowing for specific separation applications over a range of molecular sizes (e.g., from small gas molecules to larger pharmaceutical or biological molecules).⁶

Applications of mesoporous silica are centered around their morphology and porosity. Producing well-ordered mesoporous silica materials incorporating aligned nanochannels is essential to assist the progress of such applications. In such applications, having nanostructures such as pores, domains or molecular assemblies are a crucial factor in allowing these structures to act as pathways that support or limit the mass transport of analytes.⁹ Also, among many nanostructured materials, surfactant templated mesoporous silica materials have drawn significant attention due to their frequent incorporation of cylindrical one-dimensional nanopores.^{8,105,147} Importantly, mass transport within nanostructured materials is one of the vital processes required for the use of these materials in the applications mentioned above. The incorporation of pores and

small porous domains provide mass transport pathways for incorporated solvent or analyte molecules in such applications. The chemical and physical characteristics of these pathways can further determine the mass transport process by assisting or limiting molecular dynamics.⁹

The structural and morphology characteristics of mesoporous materials are usually assessed by electron microscopy (EM),^{1,73-79} small-angle X-ray scattering (SAXS),^{1, 74-76, 80} and nuclear magnetic resonance (NMR) spectroscopy.⁸⁰ These techniques often provide complementary information on the material characteristics from a nanometer-to-micrometer length scale and a nano-to-macroscale structural basis. EM can deliver nm-scale spatial resolution images of the nanostructure properties, while also allowing for visualization of the local structures. SAXS provides average information about the orientation and spacing of ordered nanostructures within a macroscopic (< 1 mm) sample region. By combining two or more of these techniques the complete structural analysis of mesoporous silica can be achieved.

The local attributes of mesoporous silica such as the pore diameter and orientation can be directly revealed from high-resolution microscopic views (e.g., TEM and SEM) of the mesostructure. These techniques provide visual evidence of the local structure of the material through direct observation of the mesopores with nanometer-scale spatial resolution.^{71, 72} Unfortunately, it is quite challenging to discuss the longer-range (>10 μm) orientation and organization of the nanostructures from such measurements. These techniques can only be used to image microscopic regions of a given sample, making it time-consuming to study larger areas (> 10 μm) of the sample. SAXS probes the material characteristics across the sample thickness by detecting X-ray scattering at very low angles (< 5°). SAXS provides average orientation and spacing information about the organized pores (2-30 nm in size) in mesoporous silicas. However, the materials properties obtained by SAXS measurements are effectively averaged over macroscopic (< 1 mm) sample regions.^{71,72} The characterization of materials' structural properties is necessary to establish the formation of well-ordered mesoporous silica solids incorporating

aligned nanochannels. This knowledge further facilitates the optimization of synthesis conditions and the development of well-defined procedures for synthesis of mesoporous silica materials.

As described in this dissertation, it is often more important to characterize and understand the mass transport properties of mesoporous materials in order to achieve optimal performance in their intended applications. Unfortunately, none of the structural characterization methods discussed above provide direct dynamical information related to their mass-transport characteristics such as the rate and anisotropy of diffusion for incorporated reagents and analytes. NMR can detect the dynamics of molecules within the nanomaterials and also provide evidence on the long-range structure orientation.⁸¹ However, it can only provide spatially-averaged information over a relatively large sample region.⁸¹ Flux measurements have been used to observe the overall continuity and accessibility of nanoporous materials for small molecules and relatively large proteins.¹⁰⁵ Further, overall transport rates and selectivities for these molecules within nanopore materials have been measured.¹⁰⁵ Unfortunately, none of the aforementioned methods provides enough information to fully characterize the spatial and temporal heterogeneities of these materials and their mass-transport properties within local, μm -scale sample regions.

1.2 Single Molecule Tracking Methods Applied to Mesoporous Silica

In recent years, single molecule tracking (SMT) has been employed as a unique method to overcome the above limitations of conventional methods and has also been used as a means to directly probe mass transport.^{9,53} As a result, SMT methods are now being widely employed in investigations of mesoporous systems.^{27-30,53,82-87} SMT is an effective method of understanding the dynamic behaviors and material characteristics in 1D cylindrical nanostructures.⁴⁵ SMT is most useful for exploring the relatively slow diffusion dynamics of molecules confined within such nanostructures.

In the SMT method, the diffusion dynamics of individual fluorescent probe molecules are monitored under wide-field illumination in an optical microscope having high nm-scale spatial precision and millisecond temporal resolution. The wide-field microscope allows the recording of fluorescence videos that reveal the presence of confined molecular pathways in the materials.^{9,53} Furthermore, the SMT method provides the ability to visualize open mesopore structures and characterize their orientation and organization. Also, it provides visual evidence of nanostructure accessibility for probe molecules as well as the direct determination of the dimensionality and mobility of the probe's diffusive motions. This information provides a unique means to assess the qualitative picture of the local mass-transport and structural properties of nanostructured materials. The comprehensive quantitative assessment of single molecule data from probe molecules affords quantitative measures of materials order, nanostructure sizes, and continuity. Most importantly, the trajectory data reveals the local mass transport and material properties of the 1D nanostructures.⁴⁵

The most significant advantage of SMT over conventional methods is the capability to monitor molecular dynamics such as interfacial adsorption and partitioning of permeants between the different phases at the single-molecule level. Single-molecule-level detection facilitates in-depth exploration and investigation of the materials spatial and temporal heterogeneities. For example, surface defects, the presence of solvent (e.g., water) islands, or the irregularity in the formed micellar structures can be detected. A comprehensive study of the single molecule trajectories generated from molecular diffusion at the single molecule level can yield significant fundamental insights on the nanostructure of mesoporous silica materials and the host-guest interactions between nanopore structure and probe molecules. In addition, the frame-to-frame mean square displacement (MSD) for each molecule in the SMT videos allows for estimation of the rate of mass transport (given by, e.g., the diffusion coefficient) of incorporated probe molecules. This information further leads to a qualitative and quantitative evaluation of the level

of confinement and the mechanisms of diffusion for probe molecules inside the silica-surfactant nanochannels. An in-depth study of the single molecule trajectories generated from the SMT method for a specific probe molecule can deliver valuable information on the location of individual molecules and the heterogeneity of their surrounding environment. The method can be further extended for use with biological systems such as DNA, to explore their microscopic chemical properties (i.e., dielectric constant).

1.3 Objective and Motivation of the Present Research

In the present dissertation, the SMT method was used to probe and quantitatively analyze the heterogeneity of the nanoscale morphology and mass-transport dynamics of surfactant templated mesoporous silica nanochannels. The primary objective of the studies performed in this dissertation is to explore the molecule dynamics, and mass transport in solvent filled surfactant templated mesoporous silica materials. SMT facilitated the characterization of the 1D nanostructured materials by detecting and quantitatively assessing the diffusion dynamics of single molecules within the cylindrical nanopores with high spatial resolution. SMT offered evidence of properties of confined nanoscale morphologies and structures. Importantly, the single molecule diffusion trajectories obtained afforded a wealth of information from the quantitative assessment of the molecular transport. A better understanding and quantitative evidence of the above stated facts play a profound role in governing ultimate application performance.

In all solution-phase applications of mesoporous silica materials, the nanopores contained within the silica gel are necessarily filled with liquids, such as compressed water or organic liquids condensed from the atmosphere, or the surfactants and solvents remaining from materials synthesis. The efficiency and selectivity of catalytic reactions and chemical separations occurring in liquid-filled mesoporous materials are governed by the translational and orientational mobilities, and surface interactions of the incorporated solvents, reagents, and analytes.¹⁴⁶ The properties of

solvents in nanoconfined pores have been reported to differ from those of bulk liquids, due to molecular cooperativity.¹⁻¹⁴ The properties of the pore-filling solvent plays a crucial role in determining mass transport and molecule dynamics within the nanochannels. Interactions of incorporated reagents and analytes with the pore-filling medium and pore surfaces govern the molecular level mechanisms of mass transport within such materials.¹⁴⁶ The location of the reagent and analytes, as well as the volume they explore inside the pore structure, constitute important information required to fully understand their behavior in nanoconfined spaces. For example, the reagent's and the analyte's ability to explore the full pore diameter or capability to move between central or near-surface pore regions facilitate the partitioning of the permeants between the different phases within the cavities or nanoscale domains or adsorption onto their surfaces. These same factors play an integral role in defining the selectivity of chemical separations in mesoporous silica.¹⁴⁶ Therefore, it is important to explore and understand the nanoscale morphology and molecule dynamics in a surfactant-silica mesoporous nanochannel, which provides essential aid to optimize and develop the performance of such applications.

Mesoporous silica systems have been studied previously by many methods including NMR^{15,16} and ensemble spectroscopic methods.¹⁶⁻¹⁸ Unfortunately, the exact location of the probe molecules within the pores has been difficult to ascertain. To date, the most detailed molecular level information on solute confinement within silica mesopores has been obtained by computer modeling.^{25,26} In the present dissertation, the SMT method was applied to investigate the exact location of the probe molecules inside solvent- and surfactant-filled mesoporous silica nanopores. Surfactant-silica mesopores incorporating the cationic surfactant cetyltrimethylammonium bromide (CTAB) were investigated by employing suitable probe dye molecules (i.e., Nile Red and PDI dyes). This dissertation demonstrates the applicability of modified SMEP and sSMT methods to explore mesoporous silica materials, to quantify their properties such as nanoscale heterogeneity, and to assess their mass transport characteristics. The rate of diffusion of probe

molecules and their confinement were investigated to understand the mass transport within solvent- and surfactant-filled mesoporous silica materials. The dependence of molecular confinement on dye charge and structure was also explored in this dissertation. More evidence of their location, confinement, and the nanoscale heterogeneities within pore structure (e.g., surface defects, the presence of solvent (e.g., water) islands, or irregularity in the formed micellar structures) were further investigated by incorporating probe molecules of different charges and sizes. The capability of the sSMT method to explore biological environments were demonstrated by determining the dielectric constant, ϵ , of nonpolar microenvironments in double-stranded DNA (ds-DNA) single molecules both in aqueous buffer solution and when adsorbed on amine-modified chemical gradient surfaces.

1.4 Overview of Thesis

The present dissertation consists of eight chapters. It begins with a general introduction of the research performed, along with the research objectives and motivations of the dissertation (Chapter 1). Chapter 2 discusses the applications and properties of surfactant-templated mesoporous silica materials. This chapter explains the synthesis of surfactant templated mesoporous silica materials by the evaporation induced self-assembly method and further discusses mass transport in these nanostructured materials. Chapter 3 focuses on the methods used in investigating mass transport in nanostructured materials. Both ensemble and conventional methods for investigation of mass transport are briefly discussed. This chapter mainly explores the applicability and advantages of single molecule tracking methods in the investigation of nanostructured materials and their mass transport characteristics. Chapter 3 further introduces two modified methods of single molecule tracking (SMEP and sSMT methods) that have been applied in this research. These methods were employed to observe and assess specific morphological and molecular dynamics characteristics of the materials being investigated. Chapter 4 covers

experimental details such as the preparation of surfactant-templated mesoporous silica materials and details of the fluorescent probe dyes employed in single-molecule imaging. Also, in this chapter, the instrumentation employed in wide-field fluorescence microscopy and imaging are discussed in detail. The last section of Chapter 4 describes the orthogonal regression analysis method and trajectory angle order parameter analysis, which represents the quantitative assessment of all 1D SMT data in the present work.³⁸

The confined translational and orientational motions of the solvatochromic dye Nile Red and a series of four different PDI dyes diffusing along one dimension (1D) within individual cylindrical silica mesopores were investigated in this dissertation. Both Chapters 5 and 6 investigate the nanoscale structural properties and mass transport characteristics of mesoporous silica materials synthesized by incorporating cationic surfactant, cetyltrimethylammonium bromide (CTAB) as the structural directing agent. In Chapter 5 spectroscopic single molecule tracking (sSMT) studies were used to determine the location of the Nile Red dye within solvent and surfactant filled mesoporous silica materials. Single molecule emission polarization (SMEP) methods were used to explore the confinement and alignment of the probe dye molecules inside the silica nanochannels. These studies have afforded an enhanced understanding of how nanostructuring of the pore-filling medium in solvent and surfactant filled mesoporous materials governs the mass transport and surface interactions of incorporated reagents and analytes. In Chapter 6, the dependence of molecular confinement on dye charge and structure was explored. The SMEP method and four different PDI dyes were employed to compare the dynamics of charged and uncharged perylene diimide dyes in surfactant-silica nanochannels. The results provide evidence on the degree of confinement and the diffusion mechanism for each molecule. Chapter 6 offers more evidence of probe molecule location and nanoscale heterogeneity (e.g., surface defects, solvent islands (e.g., water) or irregularity in the formed micellar structures) within solvent and surfactant filled mesoporous silica materials. Chapter 7 demonstrates the applicability

of sSMT methods in the study of nanostructured biomolecules by determining the dielectric constant, ϵ , of nonpolar microenvironments in double-stranded DNA (ds-DNA) single molecules both in aqueous buffer solution and when adsorbed on amine-modified chemical gradient surfaces. In Chapter 7, quantitative information on the local dielectric properties of plasmid DNA is obtained in buffer solutions of different ionic strengths and on the aminosilane gradients, again using the solvatochromic dye Nile Red.

Chapter 2 - Mass Transport and Nano-Structure of Surfactant-Templated Mesoporous Silica Materials

Surfactant-templated mesoporous silica materials play an important role in both research and industrial fields due to their chemical and thermal stability as well as well-defined and controllable structure. Among many nanostructured materials, solvent and surfactant-filled mesoporous silica materials¹ find a wealth of potential applications as models for self-assembly in confined geometries,² and as porous media for solution-phase catalysis³⁻⁵ and chemical separations.⁶ In these applications, the transport rate and selectivity are governed by the partitioning of permeants between the different phases and by mass transport within the cavities or nanoscale domains.⁹ Also, interfacial adsorption is another important factor in determining materials properties for the above applications.⁹ The characterization of the nanoscale structures and a comprehensive study of mass-transport characteristics within such systems is important to understand and improve materials properties and performance for the applications mentioned above.

Self-organized nanostructured materials such as surfactant-filled mesoporous silica containing pores, domains, or molecular assemblies provide pathways that may facilitate or limit the mass transport of incorporated reagents and analytes. Interactions of incorporated reagents and analytes with the pore-filling medium and pore surfaces govern the molecular level mechanisms of mass transport within such materials.⁹ The present dissertation primarily focuses on such cylindrical one-dimensional (1D) pathways in surfactant filled mesoporous silica material and to understand mass transport within them. When considering application-specific performance, host-guest interactions within nanomaterials play a significant role in defining mass transport and selective transport of specific reagents/analyte. Mesoporous silica systems for condensed-phase applications incorporate surfactant templates and solvents within their pores. The pore-filling

medium can create nanoscale heterogeneity that leads to a complex host-guest model with many possible selective mass transport paths.

2.1 Surfactant-Templated Mesoporous Silica

Surfactant-templated mesoporous silica materials gained popularity in industrial and research fields due to their relatively simple, time-efficient, and low-cost synthesis process.⁹⁵ Most importantly, their tunable pore size and well-organized, narrow pore distribution caught the attention of many researchers in research fields such as catalysis, chemical separation, molecular sieving, and optical materials, due to their unique properties, including high surface area, large pore volume, controlled morphology, facile functionalization, and good biocompatibility.⁴ Before the discovery of micellar and lyotropic liquid-crystal phases as templates for organized mesoscale porous structures, it was challenging to synthesize and design well organized structured nanomaterials.^{64,88,89}

Mesostructured and mesoporous materials have been developed in various shapes and morphologies such as fibers, powders, and thin films. Synthesis of these materials commonly employs a well-established sol-gel process. In this process, alkoxy silane (e.g., tetramethoxysilane, TEOS) precursors are hydrolyzed and condensed in the presence of amphiphilic surfactant molecules (e.g., cetyltrimethylammonium bromide, CTAB) that act as structure directing agents.¹⁰⁷ Spin-coating¹⁰⁸ or dip-coating¹⁰⁷ procedures are the simplest procedures by which to obtain thin films of mesoporous silica materials.

In this process, several synthesis parameters such as the concentration of reagents (e.g., surfactants and silica precursor), concentration and nature of the catalyst, and any subsequent processing conditions such as drying and calcination all play crucial roles in controlling the properties of the final product.⁹² Importantly, these synthesis parameters determine the properties of silica materials, including their final structure, morphology, and porosity. The controlled and

optimized synthesis parameters can offer more productive and applicable mesoporous silica products.

2.1.1 Properties and Application of Mesoporous Silica

Surfactant-templated mesoporous silica materials became a significant class of nanostructured materials due to their unique properties and broad applicability in a number of disciplines. Because of their inorganic framework, they have been introduced as chemically and thermally stable nanomaterials with well-defined and controllable structures.

Importantly, by simply changing synthesis parameters a diverse group of porous materials can be obtained. For example, synthesis conditions such as the acid catalyzed sol-gel-process commonly produce silica networks with relatively low porosity, while the base-catalyzed reaction, in general, leads to xerogels with intrinsic higher porosity.⁹² The narrow and tunable pore size distribution that can often be obtained allows surfactant templated mesoporous silica to stand out amongst other porous materials.⁹² The uniform and well-defined porous structures of surfactant templated mesoporous silica materials affords routes to a wealth of applications in chemical separations¹¹⁰, sensing,¹¹¹ catalytic substrates,¹¹⁰ nonlinear optical materials¹¹² and solid-state electrochemical devices.¹⁰⁴ Uniform and well-defined mesoporous structures are important in defining the selectivity and efficiency of their applications.¹⁰³ For example, the separation applications exhibit a link between the morphological characteristic of the incorporated nanomaterials and separation performance. It has been observed chromatographic band broadening in the presence of strong adsorption sites on the nanostructure surfaces as well as the presence of defects often exhibit adsorption and desorption events of molecules at the surface in a statistically random process.^{159,167}

Surfactant-templated mesoporous silica materials are popular in medicine and environmental applications because of their biocompatibility and low toxicity. They are often applied in drug delivery systems due to their capability in enhancing bioavailability of poorly water-soluble drug

molecules.¹⁷⁸ Also, the porous structure facilitates mass transport, which allows them to be used in applications that require the associated species to enter and interact with the materials. Such materials might be used to remove toxic organics and heavy metals from wastewater in water purification systems, for example.¹⁷⁸

Furthermore, mesoporous silica materials can also be easily modified with well-established chemistries, thus offering valuable means for their optimization for use in potential applications.⁹² Importantly, as synthesis of silica materials by the sol-gel process is frequently performed at room temperature, these mild reaction conditions allow for incorporation of many reagents (enzymes, catalysts, or receptors) without degradation of their activity and reactivity.

In the applications mentioned above, analytes or small molecules of interest are incorporated within or move along the nanopores of surfactant templated mesoporous silica materials. Obtaining well-ordered mesoporous silica materials with aligned nanochannels by well-defined procedures are advantageous to develop and optimize their performance for these applications. Mainly, it is essential to understand the interaction between the analyte/guest molecule and nanoscale structure to acquire a better understanding of mass transport properties in surfactant templated mesoporous silica nanochannels.

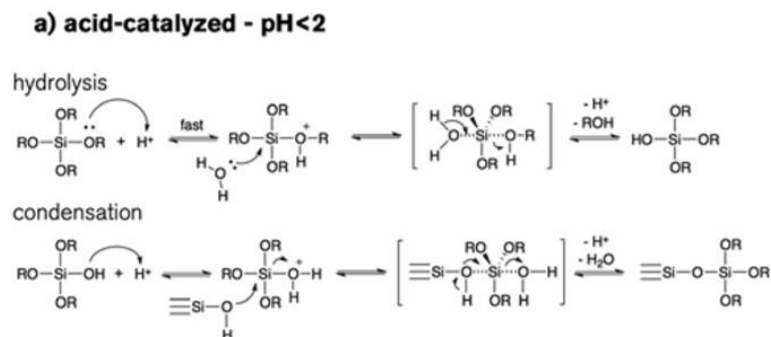
2.1.2 Silica Sol-gel Process

The sol-gel process is the most popular and promising technique available for synthesis of mesoporous silica nanomaterials. The sol-gel process was first introduced by Graham in 1864 during his work on silica sols.¹⁷⁹ This technique has become more popular than other synthesis techniques due to its ability to control size, distribution, and morphology of the particles by controlling reaction parameters.¹⁷⁹ The sol-gel process is a low-temperature route that produces homogeneous solid materials such as mesoporous silica from small molecules. First, in the sol-gel process, silicon alkoxide monomers transform into a colloidal solution (or sol), and then this sol becomes the precursor for the formation of an integrated network (or gel) of discrete particles or

network polymers. This technique helps to produce materials of different morphology and compositions and offers diverse materials such as powders, fibers, films, and bulk monoliths.

In the sol-gel process, a colloidal suspension (or sol) is generally obtained by the acid or base catalyzed hydrolysis and condensation of alkoxy silane precursors. The acid catalyzed process produces highly crosslinked networks (e.g., a continuous gel) with relatively low porosity, while base-catalyzed process offers higher porosity due to the formation of xerogels (dried gel) by subsequent aggregation of the colloidal particles.⁹⁵ Control over the reaction conditions is very important since the final structure, morphology, and porosity of the gel depend on the reaction conditions. Moreover, reaction conditions such as the ratio of precursor silane to water, the pH and concentration of the catalyst, and aging and drying conditions have a critical effect on the product.^{91,92,94,95}

The sol-gel process offers a simple and effective method to obtain ordered mesoporous silica materials with different structural and functional properties.⁹⁰ Figure 2.1. shows the chemical processes involved in a sol-gel reaction. As the first step, the figure shows⁹³ that the silanol groups, Si-OH, form by hydrolysis of silicon alkoxides. In the next step, the silanol groups further react to form siloxane linkages. That is Si-O-Si groups.



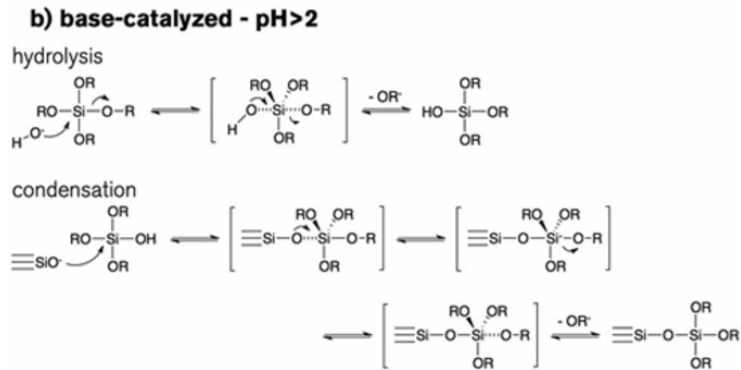


Figure 2.1 General mechanisms for hydrolysis and condensation of alkoxy silane precursors to form silica under (a) acid catalyzed conditions and (b) base catalyzed conditions Reprinted with permission from Ref (92) Copyright © 2013, Royal Society of Chemistry.

2.1.3 Evaporation Induced Self Assembly (EISA)

Evaporation-induced self-assembly process (EISA) is an efficient approach to obtain mesoporous transition metal oxides. Synthesis of surfactant templated mesoporous silica materials by EISA combines both sol-gel and self-assembly processes. Hydrolysis and condensation of alkoxy silane precursors in the presence of a rapidly evaporating solvent and a structure directing surfactant produce porous or nanocomposite materials.

The formation of surfactant micelles is the key factor in the EISA process in determining the structure of the synthesized mesoporous silica materials. In a homogeneous surfactant solution, rapid solvent evaporation causes the concentration of the solution to increase to the point at which the critical micelle concentration is exceeded, and this increase of concentration drives self-assembly of micelles.⁹¹⁻⁹³ As shown in figure 2.2.,⁴ different solvent compositions form different types of micelles such as bilayers, spherical micelles, or cylindrical micelles. Consequently, micellar structures transform into lamellar, three-dimensional (3D) cubic or 2D hexagonal mesostructures and become the templating nanostructures (i.e., forming the pores) in the fabricated silica materials.

Many researchers have attempted to explore and explain the chemistry behind the EISA process. As explained in Grosso et al., the EISA method consists of four important steps.⁹¹⁻⁹³ These steps include rapid solvent evaporation, after which the water content of the film reaches equilibrium with the atmosphere, formation, and stabilization of the hybrid mesophase, and further condensation to form the rigid network. According to Grosso et al., these steps can take place at any point of the reaction process in no specific order.⁹¹⁻⁹³

The EISA process involves the formation of liquid crystalline mesophases that template pores in the silica matrix by combining self-assembled micelles with the silica precursor.^{1,4} Figure 2.3 shows two possible formation mechanisms included with the liquid crystal templating process. The most prominent synthesis process is defined by the route labeled a) in the figure. Here, in the initial step, rapid solvent evaporation leads to the formation of lamellar, three-dimensional (3D) cubic, or 2D hexagonal mesostructures. By changing the reaction conditions such as starting solvent composition, temperature, and pH, the desired micellar mesostructure can be obtained.

In the EISA process, the formation of appropriate micellar structures such as the hexagonal mesophase comprised of cylindrical micelles is critical to obtain the desired porous mesostructures. Proper choice of reaction conditions and processing parameters as stated in the above discussion, will lead to desired mesostructure and specific material form.

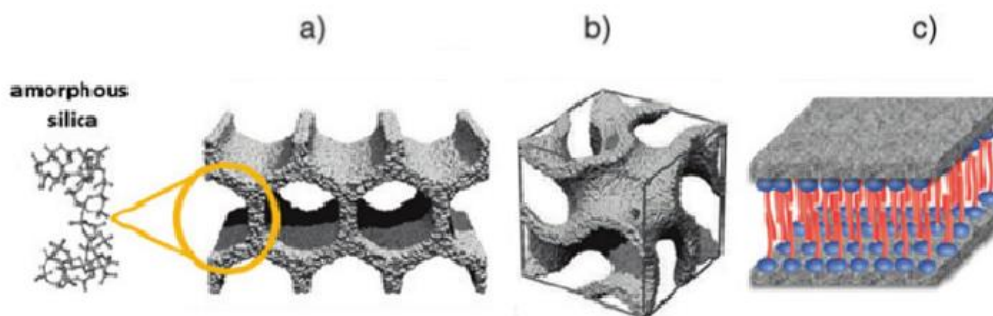


Figure 2.2 Structures of mesoporous M41S materials: a) MCM-41 (2D hexagonal, space group $p6mm$), b) MCM-48 (cubic, space group $Ia\bar{3}d$), and c) MCM-50 (lamellar, space

group **p2**). Reprinted with permission from Ref (95) Copyright © 2006 WILEY-VCH Verlag GmbH & Co. KGaA, Weinheim.

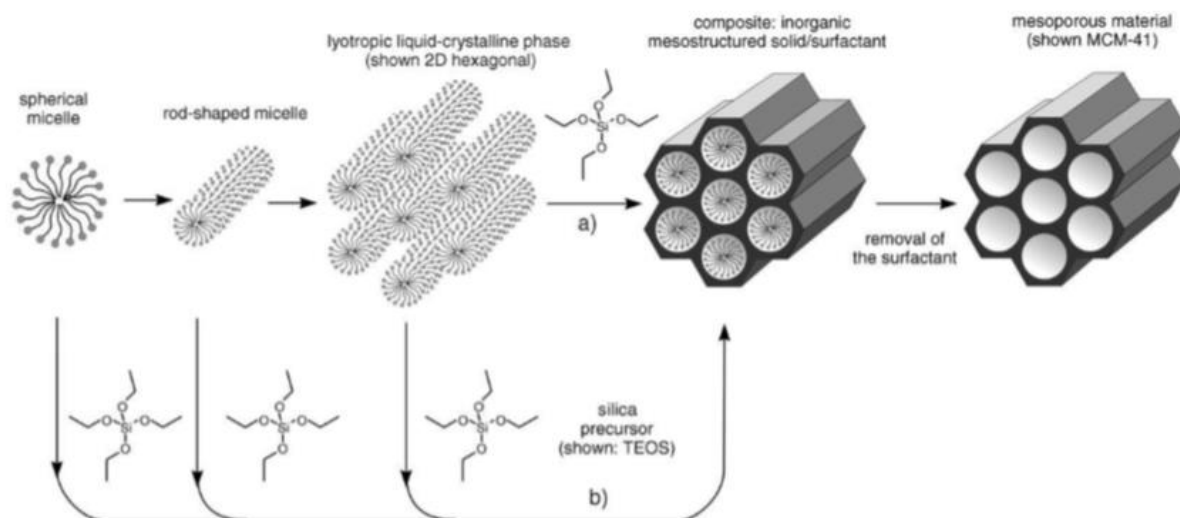


Figure 2.3 Formation of mesoporous materials by structure-directing agents: a) true liquid crystal template mechanism, b) cooperative liquid crystal template mechanism. Reprinted with permission from Ref (95) Copyright © 2006 WILEY-VCH Verlag GmbH & Co. KGaA, Weinheim.

2.2 Properties of Nano-confined Solvents

Many applications of mesoporous silica such as solution-phase catalysis³⁻⁵ and chemical separations⁶⁻⁸ require the nanometer-sized pores to be filled with solvents. In such applications, molecular level interactions between analytes and the pore surfaces define the mass transport processes occurring within the porous structure.⁹ These molecular level interactions are governed in part by the properties of incorporated solvent(s).⁹ However, nanoconfinement of the solvent can lead to solvent properties that differ dramatically from those of bulk solutions.¹¹

Importantly, among other properties, the translational and orientation motions of nanoconfined solvents often differ from what is observed in bulk solvents. Likewise, the dynamics of probe/analyte molecules within the nanopores depend upon the nature of the nanoconfined solute, solvent, and pore surfaces. Many simulations¹⁴², fluorescence studies¹⁹ and vibrational spectroscopy experiments¹⁴¹ offer evidence of nanoconfinement effects on solvent and dynamic properties of analytes such as their translational and orientation properties. For example, nuclear magnetic resonance^{15,16} and electron spin resonance¹⁶⁻¹⁸ experiments demonstrate the slowing of probe motions with decreasing pore size in solvent-filled pores in mesoporous materials. The results of fluorescence studies have come to similar conclusions by revealing evidence of decreased solute motions as a result of increased levels of confinement.^{9,19-21} The fluorescence studies¹⁹ provide valuable evidence on nanoconfined analyte molecules. In earlier studies of mesoporous silica materials by single-molecule emission polarization (SMEP) methods, perylene diimide (PDI) dyes were shown to exhibit unexpectedly strong confinement as they diffused within the one-dimensional (1D) pores of surfactant-templated mesoporous silica films.¹⁴⁶ Also, SMEP measurements demonstrate that the PDI molecules diffuse with their long axes aligned parallel to the long axis of the pores.¹⁹ Further, spectroscopic single molecule tracking (sSMT) studies using the polarity sensitive dye Nile Red (NR) employed to determine the location of the molecules, and these results demonstrate that the NR dyes are confined to the hydrophobic cores of the micelles.¹⁴⁶

Importantly, a variation of properties of nanoconfined solvents and analytes can result in interactions of the liquids with the pore walls.¹¹ Surfactant and solvent filled mesoporous silica structures form a heterogeneous environment due to the presence of organized surfactant structures within the pores, as well as those of incorporated solvent/analyte mixtures. The pore structures are expected to be relatively polar and hydrophilic micelle/pore interface, while taking on the non-polar and hydrophobic character at the center of each pore.¹ The resulting heterogeneous environment inside the surfactant-silica pore system could limit the solvent and analyte/probe

molecular motion to specific nanoscale subregions within even the smallest pores. Furthermore, an understanding of the properties of nanoconfined solvents/analytes can also be made more complicated due to the spontaneous demixing (i.e., phase separation) of solvent mixtures in such nanoscale environments.¹⁰

2.3 Mass Transport in Nanostructured Materials

Most nanostructured materials, including surfactant templated mesoporous silica, have found a wealth of applications in the field of solution-phase catalysis,³⁻⁵ chemical separations⁶⁻⁸ and as energy storage. In such applications, having nanostructures such as pores, domains or molecular assemblies are a crucial factor in allowing these structures to act as pathways that support or limit the mass transport of analytes.⁹ Also, among many nanostructured materials, surfactant templated mesoporous silica have drawn significant attention due to their cylindrical one-dimensional pathways.^{8,30,147} Importantly, mass transport within nanostructured materials is one of the vital processes required for the use of these materials in the applications mentioned above. The structural characteristics such as pores and domains provide pathways to incorporated solvent or analyte molecules in such applications. The chemical and physical characteristics of the pathways can further determine the mass transport process by assisting and limiting molecular dynamics.⁹

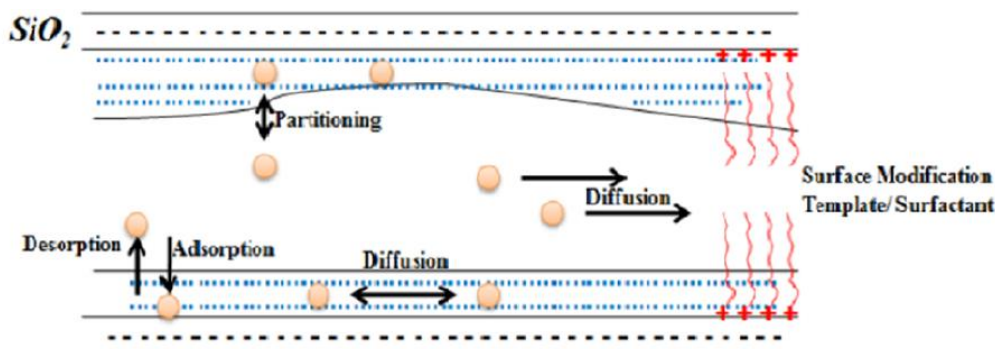


Figure 2.4 Model for partitioning and mass transport (e.g., diffusion) in solvent-filled 1D nanoporous media such as solvent and surfactant filled mesoporous silica.

Several different dynamic phenomena participate in mass transport processes occurring within solvent filled surfactant templated mesoporous silica nanochannels. The analyte molecules exhibit various molecular dynamics such as adsorption/desorption, partitioning and diffusion within and between phases. The partitioning of analytes between different layers/phases as well as the diffusion of analyte molecules within layers/phases determines the selectivity and transport rate of analyte molecules. The presence of solvent layers or phases¹⁴ and the diffuse electrical double layer^{105,147,148} affects the mass transport by spatial permeant distributions within these nanostructures.⁹ The presence of nanoscale structures such as layers/phases can act as impermeable or semipermeable barriers to confine molecular motions in one or more dimensions.⁹ The physical and chemical properties of nanostructured materials are highly affected by nanoscale molecular dynamics occurring in their cavities or nanoscale domains. Moreover, a clear understanding of mass transport and molecular dynamics within nanostructured materials plays an important role in understanding their properties and optimizing their applications.

Chapter 3 - Optical, Microscopic, and Single Molecule Methods for Investigating Mass Transport in Nanostructured Materials

The mass transport is a key factor in application-specific performance characteristics of nanostructured materials. The knowledge gained from the investigation of mass transport in nanostructured materials helps to improve and optimize their applications. Many simulation studies¹⁴², fluorescence methods¹⁹ and vibrational spectroscopy experiments¹⁴¹ offer some evidence of properties of solvents/analytes in nanostructured materials. But such experiments do not provide sufficient information to fully understand the mass transport since this is a molecular level process taking place in nanoscale structures. Unfortunately, the exact location of the probe molecules within the pores has been difficult to ascertain. The impacts of probe location have been explored in liquid crystal mesophases²² and in surfactant-templated silica^{23,24} by employing two or more fluorescent probes that partition differently between polar and nonpolar regions. Unfortunately, such methods do not allow for the location of individual probe molecules to be explicitly identified.¹⁴⁶

3.1 Ensemble Methods for Mass Transport Nanostructured Materials

Throughout the years, many approaches have been taken to investigate the mass transport in nanostructured materials but most of these approaches are known as ensemble methods. In an ensemble method, information can be obtained as an “average result” of a large number of molecules in many different local environments. For example, methods such as quasielastic neutron scattering (QENS) and Fourier transform infrared spectroscopy (FTIR) studies were used to monitor the effects of pore structure on methanol molecules adsorbed in HMCM-41 and HZSM-5 molecular sieves.¹⁴⁰ These studies have shown that the motions of capillary-condensed alcohols become slower as the pore size decreases in mesoporous silica, due to interactions of the alcohols

with the pore walls.¹⁴⁰ Furthermore, these methods do not offer necessary insight into nanoconfined solvent systems and effectively “average out” important molecular level aspects. Therefore it is important to consider other methods to investigate nanoconfined solvent systems. Also, fluorescence recovery after photobleaching (FRAP) experiments are commonly used the optical technique to investigate solvent and analyte molecules behavior in nanostructured systems.^{149,150} But, similar to other ensemble methods, FRAP experiments involves extensive signal averaging which will limit detecting valuable molecular level information.

The flux method can be introduced as another important example of an ensemble method. Briefly, in the flux method, the concentration of permeants will be observed and recorded while they pass from the source reservoir through the material.^{147,148}

$$J = -DP \frac{\varepsilon}{\tau} \frac{dC}{dx} \quad (\text{eq 3.1})$$

The equation 3.1 defines the diffusion-controlled flux, J , of permeants through a nanoporous monolith.⁹ Where, D is the diffusion coefficient of the permeant within the pores; P is its partition coefficient, defined between the external solution and the pore-filling medium; ε is the fraction of the material cross-section comprising open pores, τ is the pore tortuosity; and dC/dx is the concentration gradient.⁹ The eq. 3.1 exhibits that flux is associated with both mass transport parameters (D and P) and the structural properties (ε and τ) of the material.⁹ These details will provide average information on the mass transport process but limit acquiring details of molecular-level processes such as molecule-matrix interaction and limit the ability to observe molecular motions. These methods will not provide necessary insight into nanostructured systems and effectively “average out” important molecular level aspects. Therefore it is important to consider other methods to investigate mass transport in nanostructured materials.

3.2 Single-Molecule Methods for Mass Transport Studies

The single molecule methods provide an important to explore chemical, steric and electrostatic interactions between the solvent/analyte molecules and nanoscale structures to fully understand molecular dynamics in nanostructured materials. The information gained by ensemble techniques does not provide great details. Therefore, techniques capable of observing properties and behaviors of each solvent/analyte molecule incorporated in nanostructured materials needed to be introduced. The optical single-molecule methods¹⁵¹⁻¹⁵⁶ have been able to address the challenges and limitations of previous ensemble measurements successfully. Also, optical single-molecule methods facilitate the detection of nanoscale domains and their morphologies under the high spatial resolution,^{9,53} which makes this method popular and more useful than x-ray scattering methods and electron microscopy methods.¹¹⁴⁻¹²² The optical single-molecule method expected to offer the capability to detect individual molecular level mechanism and to observe and track the motions of individual fluorescent molecules in many transparent media. Therefore, this method provides a better means for studies of mass transport within transparent nanostructured materials.^{53,95,157,158} In single molecule techniques, fluorescent molecules are used to detect molecular dynamics in nanoscale structures, and these probe molecules are capable of partitioning into specific nanoscale domains of interest. Furthermore, trajectory data collected from these probe molecules will offer information such as rate and directional motion of the analyte molecules in nanostructured materials. Also, this technique provides the details of nanoscale structural properties and their effect on limiting and facilitating molecular dynamics which will provide more evidence to understand mass transport characteristics within nanostructured materials.

3.3 Single-Molecule Fluorescence Methods

In 1996, Schmidt and coworker performed the first single-molecule tracking experiment to obtain diffusion coefficients of rhodamine dye-labeled phospholipids in a phospholipid membrane under ambient conditions.⁴⁵ Over the years, many single-molecule fluorescence methods have

been developed such as confocal microscopy, wide-field single-molecule tracking (SMT) and fluorescence correlation spectroscopy (FCS).

The confocal microscopy method is capable of observing individual diffusive transits and adsorption events and quantify collected data.⁹ The confocal method records single-point time transients of a passage of probe molecules at an isolated detection volume.^{153,164} The confocal microscopy imaging technique increases the optical resolution and contrast of an image by using a spatial pinhole to block out-of-focus light in image formation.⁹ Capturing multiple two-dimensional images at different depths in a sample enables the reconstruction of three-dimensional structures within an object. Briefly, the confocal imaging employs a laser light to excite fluorescence probe molecules. The excitation light is pass through any required optics such as a polarizers and filters. Then the light is directed into a high numerical aperture objective by a dichroic mirror and focuses into the sample. The beam scanning or sample scanning methods can be employ to obtain the sample position relative to the laser spot. Using the same objective, the fluorescence from the sample is frequently acquired in reflection. The collected light is passed back through the dichroic mirror and focused through an appropriately sized pinhole placed in an image plane of the microscope. Then the light is directed through any additional filters and/or polarizers and subsequently imaged onto a detector, such as a single-photon-counting avalanche photodiode.⁹ For sufficiently dilute solutions (e.g., <1 molecule in the detection volume), passage of molecules through the microscope focus produces bursts of signal above the background.⁹

On the other hand, the fluorescence correlation spectroscopy (FCS) method will be used to generate a correlation function for the purpose of analyzing fluctuations of the fluorescence intensities coming from probe molecules.^{165,166} Simply, FCS is a correlation analysis of the fluctuation of the fluorescence intensity. The fluorescence intensity fluctuations can be due to diffusion, physical/ chemical reactions or aggregation taking place in a nanoscale environment. Briefly, the fluorescence emitted from a very tiny space in solution containing a

small number of fluorescent particles is observed. The fluorescence intensity fluctuation due to particles passing through the space is observed and analyzed to obtain the average number of fluorescent particles and average diffusion time of the particles.

When considering the wide-field single-molecule tracking (SMT), it provides the ability to track probe molecule with millisecond time resolution as well as nanometer-scale spatial precision.^{45,61,161-163} Further, SMT methods capability to detect single molecule at single event levels provide evidence of temporal and nanoscale spatial heterogeneity of nanostructures in different environments.¹²³

3.3.1 Wide-Field Fluorescence Video Microscopy and Single Molecule Tracking (SMT)

Wide-field single-molecule tracking (SMT) method is one of the successful technique to overcome limitations and challenges in many of the discussed ensemble and conventional methods. It is known from the theory and experiments that SMT method offers quantitative measurements of local concentrations, molecular diffusion coefficients, diffusion anisotropies, adsorption and reaction times, the order and orientation of nanostructures, and the confinement of molecular motions.⁹ Using SMT methods, trajectories of fluorescent probe molecules are recorded, and, when properly analyzed, these trajectories provide information on the rate and direction of probe molecule motions. While other optical methods as FRAP experiments only measure the diffusion of many probe molecules in μm -scale regions, SMT is capable of detecting the diffusion of each molecule over nm-scale regions.¹²⁴ Therefore, it has been applied to detect diffusion in near-surface regions.^{45,167} Also, diffusion dimensions of molecules in different nanostructured materials such as polymer films,¹²⁶ lipid bilayers,^{44,128} Langmuir films,^{44,129,130} in gels^{127,131} and cell membranes^{132,133} have been studied. Furthermore, SMT studies are applied in observing molecular level processes such as molecular adsorption at interfaces and partition coefficient in nanoscale environments.^{159, 167, 170, 171} Recent studies exhibit that SMT method provides qualitative evidence

of sizes, orientation, and order of the organized domains within mesoporous silica materials and diblock polymers.^{39,84,113} Also SMT has been successfully employed in detecting mass transport within nanostructured materials as well as to observe defects and material heterogeneities.^{39,134,147}

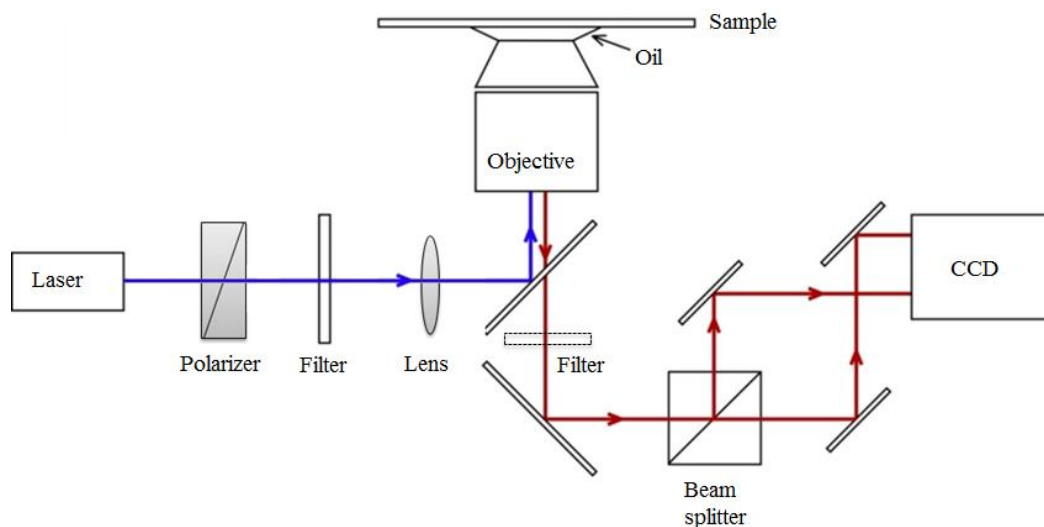


Figure 3.1 Common components often found in wide-field microscopes. Some optics have been omitted for simplicity. Abbreviations: CCD, charge-coupled device.

Figure 3.1 shows the components of a wide-field microscope that are commonly employed in the SMT method.^{9,53} In the first step, fluorescence probe molecules in the transparent sample will be illuminated by focusing a laser beam through the back aperture of the microscope objective, but in some approaches, probe molecules are illuminated externally to the objective.¹²³ Depending on the probe specificity, expected information and simple experiment condition there can be a variety of optics inserted in the optical path. For example in each specific experiment different filter cubes, bandpass filters, dichroic mirrors, and polarizing beam splitters can be employed. The imaging detectors such as Charge-Coupled Device (CCD) camera, or Complementary Metal Oxide Semiconductor (CMOS) camera, or an Electron multiplying CCD (EMCCD) camera are

commonly employ as the detectors.¹⁸⁰ But in CCD/CMOS detector, readout noise can severely weaken the quality of the acquired data, especially at low signal level measurements.¹⁸⁰ Among other detectors, the EMCCD camera successfully resolves this issue by minimizing readout noise on the measured signal by amplifying the signal before the readout process.¹⁸⁰ After collection of video data with the CCD camera, the videos must be processed and analyzed. This is commonly accomplished using either commercial or custom-written image analysis software. These computer programs can be employed to locate the individual fluorescent spots in each frame.¹⁶⁰ These spots are commonly approximated by Gaussian intensity profiles.^{47,48} Fitting of the spots to two dimensional (2D) Gaussians allows their locations to be determined with subdiffraction and subpixel precision.⁶¹ These fluorescent molecules can be located to within ± 20 – 50 nm and the precision may approach ± 1 nm in some situations.^{168,169} Located fluorescence spots can be further connected in each frame by a linking program to obtain probe trajectories. These trajectory data represent the time-dependent translational motions of the molecules due to molecular level processes such as adsorption and partitioning of molecules inside the nanostructured materials.

Moreover, the SMT method can be employed in observing the molecular level process in a variety of nanostructured materials such as mesoporous materials, polymer films,¹²⁶ lipid bilayers,^{29,45,128} langmuir films,^{45,129,140} in gels^{92,157} and cell membranes.^{132,133} Considering material characteristics and expected information, each experiment requires specific experimental conditions and experimental setups. The SMT method can be modified and developed according to experiment specificity by introducing a variety of optics in the optical path. Single molecule emission polarization (SMEP) mode and spectroscopic single molecule tracking (sSMT) method are two such SMT approaches that aid in the study of nanostructured materials.

3.3.1.1 Single Molecule Emission Polarization (SMEP)

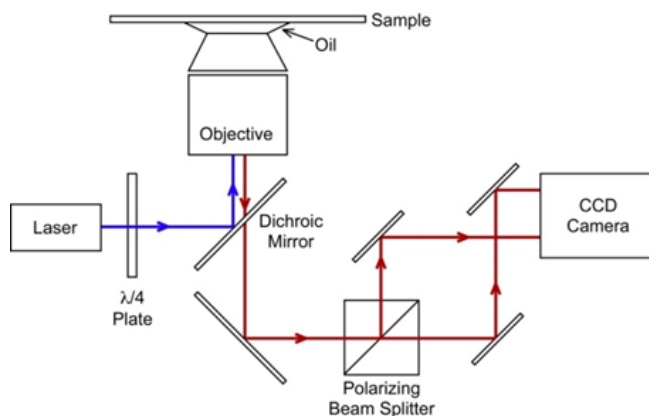


Figure 3.2 Common components often found in SMEP wide-field microscopes setup.

The SMEP is one of the SMT methods that can be used to determine the orientations of molecules, which illustrate in figure 3.2. While the SMEP method offers evidence time-dependent translational and orientational motions of the molecules, it specifically provides insight into confined molecular motions. In the SMEP method, fluorescence emission light will be split into orthogonal polarizations. Figure 3.3 provides a representative example of the data obtained. These data obtained from SMT/SMEP studies of mesoporous silica incorporating 1D nanopores in which the Nile Red molecules used as probes molecules.¹⁴⁶ The two polarization waves are collected and detected as two channels in the video image as shown in figure 3.3. The double-ended arrows designate the detected polarizations. The separate pairs of images (left and right) are displayed on identical intensity scales. In this case, the results show that the emission is strongly polarized in the direction of molecular motion, indicating the orientation of the molecules is parallel to the pore axis, and any orientational motions are tightly confined.¹⁴⁶

Briefly, in order to acquire orthogonal polarization emission from probe molecules, they must be excited by circularly polarized light. Therefore, in the optical path a quarter wave plate is involved as shown in figure 3.2, to create circularly polarized incident laser light. Then depending

on the excitation and emission wavelengths of probe molecules, emitted light will pass through an appropriate bandpass filter. The bandpass filter will block the excitation light, and pass the emission light from probe molecules. After filtering, the fluorescence will be routed into an image splitter which is fitted with a polarizing beam splitter. This splitter will divide the collected fluorescence into two image channels having orthogonal polarizations. Finally, the data can be analyzed by image analysis software.

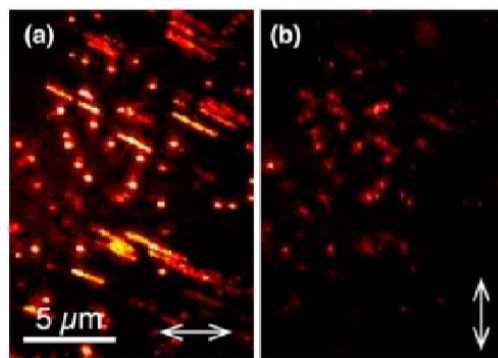


Figure 3.3 (a, b) SMEP images acquired simultaneously in two orthogonal polarizations for Nile Red-doped CTAB-templated mesoporous silica films. The orthogonal emission polarizations designated by the white double-ended arrows. The images depict the maximum signal level observed at each pixel across the 200 frame long videos. Reprinted with permission from Ref (146) Copyright © 2016, American Chemical Society.

3.3.1.2 Spectroscopic Single Molecule Tracking (sSMT)

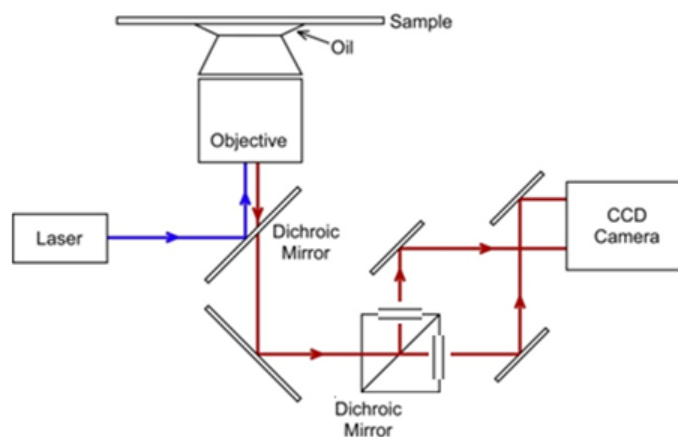


Figure 3.4 Common components often found in sSMT wide-field microscope setup.

Spectroscopic single molecule tracking (sSMT) is one of the modified SMT technique which offers characteristic specific information of nanodomains. As an example, sSMT method can be employed to determine the presence of distinct polarity environments in nanostructured materials. Some probe molecules such as Nile red (NR) exhibit specific polarity sensitive characteristics. The NR is known as a solvatochromic dye. The excitation and emission spectra of solvatochromic dyes strongly dependent on the dielectric constant of their local nano-environment. For example, when NR is in a nonpolar environment such as toluene, it emits fluorescence in the orange wavelength region. But when NR is in a polar environment such as ethanol solution it emits in the red wavelength region. Therefore, probe molecules like NR can be used to assess the polarity of nanoenvironments in spectroscopic single molecule tracking experiments. In sSMT experiment, NR emit distinct wavelength lights(625nm at polar environment and 580 nm at non-polar environments) depending on their polarity environment.

In sSMT experiments, the fluorescence collected from the sample will subsequently be directed through an appropriate filter (Schott Glass) in order to distinct excitation and emission beams. The emitted fluorescence will then be routed into a beam splitter cube incorporating a second dichroic mirror and two bandpass filters. This will divide the fluorescence into two image channels centered at two distinct wavelengths. Finally, the fluorescence in these image channels will be simultaneously detected using an electron-multiplying CCD as shown in figure 3.5. Figure 3.5 provides a representative example of the data obtained. These data obtained from SMT/sSMT studies of mesoporous silica incorporating 1D nanopores in which the Nile Red molecules used as probe molecules.¹⁴⁶ The two emission lights are collected and detected as two channels in the video image as shown in figure 3.3 In this case, the results show that the emission is strongly intense in the 580nm channel compared to 625nm channel. The sSMT data of this study reveal that the majority of NR molecules are found in nonpolar environments having polarities similar to that of n-hexane.¹⁴⁶

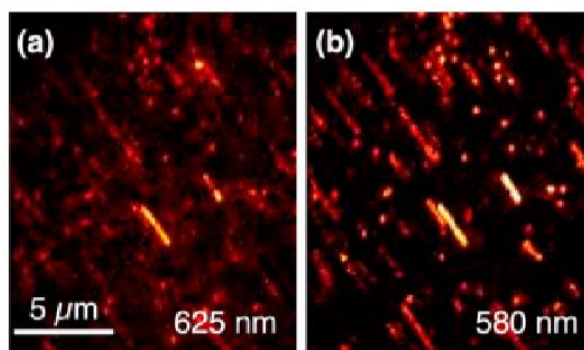


Figure 3.5 sSMT images acquired simultaneously in (a) 625nm and (b) 580 nm wavelength detection channels for Nile Red-doped CTAB-templated mesoporous silica films. The images depict the maximum signal level observed at each pixel across the 200 frame long videos. Reprinted with permission from Ref (146) Copyright © 2016, American Chemical Society.

Chapter 4 - Experimental Considerations

This chapter reports the preparation of surfactant-templated mesoporous silica films, which will be studied and discussed in Chapters 5 and 6 of this dissertation. It will also discuss the experimental techniques and data analysis procedures involved in the characterization of the samples. Each chapter will further discuss the experimental methods and sample preparation conditions for each study in detail.

4.1 Preparation of Surfactant-Templated Mesoporous Silica: Formation of the Hexagonal Mesophase

The following Chapters 5 and 6 of this dissertation discuss the surfactant templated mesoporous silica nanostructures which were employed as the confining porous system. These materials were selected due to the relative simplicity of their preparation and modification as well as wide range of their applicability in methods such as solution-phase catalysis³⁻⁵ and chemical separations.⁶⁻⁸ In this dissertation, hexagonal mesoporous silica nanostructures were synthesized by the acid catalyzed sol-gel process, while employing a surfactant as the structure-directing agent. Evaporation-induced self-assembly (EISA), as discussed in chapter 2, was also employed in the fabrication of mesoporous silica materials. EISA, in this case, involved the rapid evaporation of solvent during spin coating of the silica sols on to glass coverslips. Micelle formation and silica hydrolysis and condensation occur during the EISA process, forming surfactant-templated mesoporous silica materials.

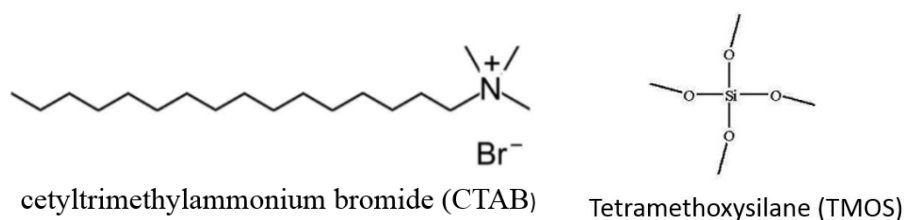


Figure 4.1 Chemical structures of (left) CTAB and (right) TMOS.

The following reagents and procedures were employed in the synthesis of the surfactant-containing mesoporous silica materials employed in Chapters 5 and 6. Briefly, silica sols were prepared by dissolving tetramethoxysilane (TMOS, Figure 4.1) in ethanol. Deionized water (18 M Ω cm) and HCl (0.1 M) in deionized water were subsequently added to initiate the hydrolysis and condensation process that leads to gel formation. This sol mixture was stirred for 1 hour and aged for another 24 hours in a desiccator. Cetyltrimethylammonium bromide (CTAB, Figure 4.1) was added to the aged sol. The sols were next stirred for an additional 1 h and then spincast onto plasma-cleaned glass coverslips at 3000 rpm for 30 s. The thin films obtained were aged for 24 h to a few days in a desiccator prior to characterization. All samples were imaged on a wide-field epifluorescence microscope. The samples were mounted on the microscope and then immediately covered with a Plexiglas chamber. The chamber was purged with a mixture of water and ethanol (8:3) vapor in N₂ gas. The gas flow rates were set to maintain an ambient relative humidity of 70% at ~22 °C. All samples were exposed to this vapor mixture for ~30 min prior to imaging and were maintained under the same atmosphere during imaging.

Importantly, proper concentrations of the surfactant, silica precursor, and water, and proper experimental conditions such as the reaction temperature need to be employed to obtain hexagonal mesoporous structures. Figure 4.2 shows the ternary phase diagram for ethanol, water (and TMOS) and surfactant. It shows the mesophases expected for sols of different compositions for each component. In this dissertation, the composition was selected to reach the hexagonal region upon evaporation of the solvent during spin coating.

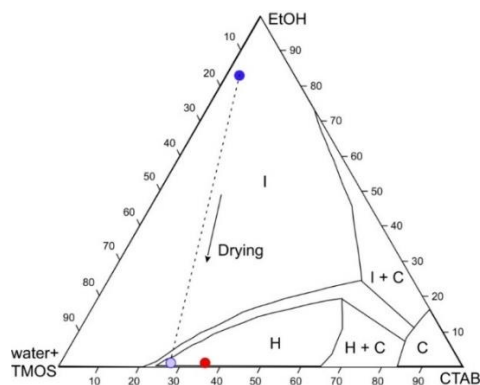


Figure 4.2 The ternary CTAB/water/ethanol phase diagram. Reprinted with permission from Ref (101). The sol composition was adjusted to form the hexagonal mesophase in spin-coated films. (I = Isotropic, C = Cubic, H = Hexagonal).

4.2 Perylene Diimide (PDI) Dyes

In chapters 5 and 6 of this dissertation, fluorescent dyes were employed as probes of the silica mesostructure (i.e., cylindrical nanopores). Tracking of mobile dye molecules revealed the presence of the nanopores and their orientations in the plane of the spin-coated films and were also used to determine their polarity properties and the accessible pore diameters quantitatively. Neutral, positively charged, and negatively charged perylene diimide (PDI) dyes synthesized in our labs were employed in initial SMT experiments.¹⁰¹ Figure 4.3 depicts the chemical structures of the PDI dyes. The specific PDIs employed included uncharged N,N'-bis(methoxypropyl)perylene-3,4,9,10-tetracarboxylic diimide (C₄OPDI), and two doubly charged PDIs, N,N'-bis(3-sulfonatopropyl)perylene-3,4,9,10-tetracarboxylic diimide and N,N'-bis(2-(trimethylammonio)ethyl)-perylene-3,4,9,10-tetracarboxylic diimide. These dyes were used to explore charge dependent mass transport dynamics in the films. Another uncharged PDI of greater length, N,N'- bis(octyloxypropyl)perylene-3,4,9,10-tetracarboxylic diimide (C₁₁OPDI), was also employed to investigate the role of steric and confinement effects on mass transport.

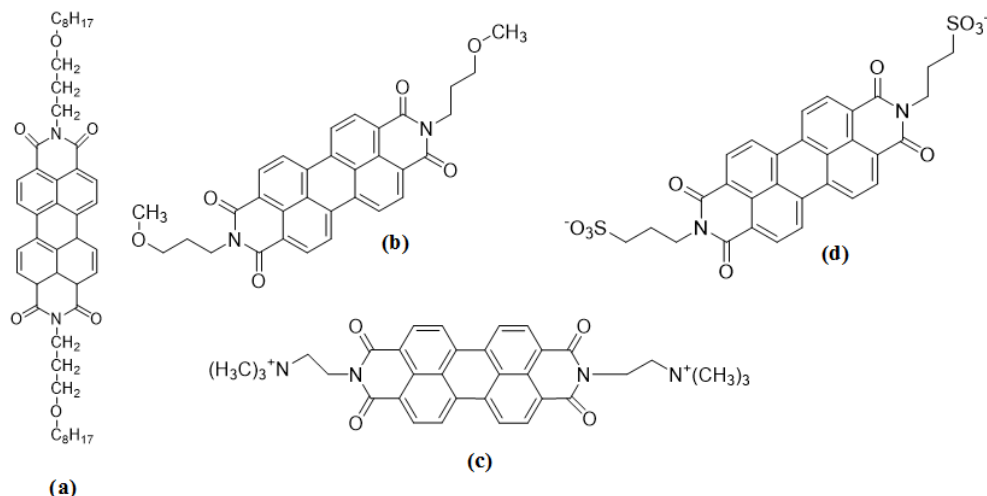


Figure 4.3 Molecular structures ;

(a) N,N'- bis(octyloxypropyl)perylen-3,4,9,10-tetracarboxylic diimide.

(b) N,N'-bis(methoxypropyl)perylen-3,4,9,10-tetracarboxylic diimide.

(c) N,N'-bis(3-sulfonatopropyl)perylen-3,4,9,10-tetracarboxylic diimide.

(d) N,N'-bis(2-(trimethylammonio)ethyl)-perylen-3,4,9,10-tetracarboxylic diimide.

4.3 Nile Red (NR) Dye and its Solvatochromic Properties

Chapter 5 of this dissertation specifically focuses on developing an understanding of the polarity properties of microenvironments within solvent and surfactant filled mesoporous silica materials.

A highly solvatochromic dye was employed for this purpose. The specific dye selected for these studies was Nile Red (NR, Figure 4.4.a). This molecule is highly fluorescent and can readily be detected at the single molecule level. Most importantly, as shown in Figure 4.4.b, this dye exhibits a strong sensitivity to the polarity of its local environment. The emission from NR exhibits

a $\sim 100\text{nm}$ bathochromic shift with a change in ϵ from ~ 2 to ~ 32 . The dramatic wavelength change in its peak emission with respect to environmental polarity is explained by its large change in dipole moment between the ground and excited states, which arises from the transfer of charge between its diethylamino and quinoidal moieties. The charge transfer state is stabilized in more polar media than non-polar media, lowering the energy of the excited state and shifting its emission to longer wavelengths with increasing solvent polarity.

Like many other dyes, such as the PDIs discussed above, NR also produces well-polarized emission. Its transition dipole is oriented slightly off its long axis direction (figure 5.1). As with the PDIs, it can also be used to study wobbling motions within the silica mesopores. SMEP methods obtain such data (see below).

Nile red has previously been used to measure the evolution of the dielectric constant for poly(vinylidene fluoride) (PVDF) films accompanying the transition from the disordered α phase to the ferroelectric β phase upon mechanical stretching.¹⁴⁵ Nile red has also been used in single-molecule (SM) studies of dielectric heterogeneity in poly(methyl methacrylate) (PMMA) and poly(vinyl alcohol) films.³⁴ Most recently, the surface characteristics of polarity gradients prepared from phenyltrimethoxysilane (PTMOS) and tetramethoxysilane have been studied by single molecule spectroscopic measurements using the Nile red molecule.⁴¹

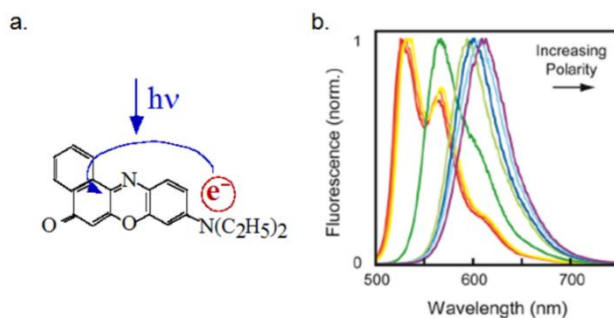


Figure 4.4 a) Nile Red molecular structure and intramolecular charge transfer process.
b) Fluorescence spectra of NR in hexane (red), heptanes (orange), cyclohexane (yellow), toluene (dark green), chloroform(light green),

dichloromethane (dark blue), acetone (light blue), and acetonitrile (dark purple) obtained with 488-nm excitation. Reprinted with permission from Ref (42). Copyright © 2013, American Chemical Society.

4.4 Instrumentation

4.4.1 Wide-Field Fluorescence Microscopy

The SMT experiments carried out in this dissertation were performed on a wide-field fluorescence microscope. A typical setup is shown in Figure 3.1.^{9,53} In our set-up, laser light of different wavelengths (e.g., 488 nm, 514nm, 532nm) was employed to excite fluorescence from the different dyes used to probe our samples. Appropriate optics such as polarizers, optical filters, dichroic mirrors, and image splitters were incorporated as required by each experiment. Most importantly, our set-up employed a high magnification and high numerical aperture (NA) objective lens (100X magnification, 1.49 NA). The use of a high magnification and high NA objective allowed for detection of single molecules as fluorescent spots of diffraction-limited size. Also, the use of a high NA objective was required for the efficient collection of the fluorescence emission from individual fluorescent probe molecules.

Furthermore, broad illumination over a relatively wide area could be achieved when the laser light was focused at the back focal plane of this objective. Broad, or wide-field, illumination allowed for the dynamics of a number of single molecules within nanoscale structures to be simultaneously recorded for μm -scale sample areas (eg. $15 \times 15 \mu\text{m}^2$ in the present work). A highly sensitive, back-illuminated electron multiplying (EM) CCD camera was employed to detect the single-molecule fluorescence. This detector provided for high-speed data collection with a signal-to-noise (S/N) ratio that was sufficient for detecting and tracking fast moving probe molecules.

In this thesis, SMT experiments were conducted by both SMEP and sSMT methods. Figures 3.2 and 3.4 depict typical set-ups and components incorporated in the microscope for SMEP and sSMT measurements, respectively. In the case of sSMT, the emission spectrum of the fluorescence

probe molecules was used to select the optics (i.e., dichroic mirror and optical filters) involved in each set-up. SMEP measurements employed a polarizing beam splitter in all cases.

4.5 Single Molecule Trajectory Analysis

4.5.1 Orthogonal Regression

Single molecule tracking experiments provide data on the locations and motions of fluorescent probe molecules. In this dissertation, SMT was used to track probe molecules in nanostructured materials, such as surfactant-templated mesoporous silica. The fluorescent spots produced by the probe molecules dispersed within these samples were recorded in the form of fluorescence videos, using the aforementioned EM-CCD camera. The spots were subsequently located in each video frame and linked into trajectories across the videos. These trajectories showed the motions of each molecule. Spot location and linking into trajectories was accomplished using software written in-house in the LabView environment. Once the trajectories were obtained, they were analyzed to distinguish mobile and immobile molecules, and those moving in 1D and 2D in the sample film plane. A comprehensive analysis of the fluorescence trajectories in this regard was carried out by employing an orthogonal linear regression analysis.³⁸ In orthogonal regression, trajectories produced by the probe molecules were fitted to a linear function, affording important quantitative parameters such as the best fit (x,y) positions of each single molecule trajectory, the in-plane orientation of the 1D trajectory segment, and estimates of positional errors for each spot and angular errors for the local trajectory orientation. Furthermore, the orthogonal regression analysis provided quantitative evaluations of the mobility (i.e., the diffusion coefficient) for each single molecule.

The orthogonal regression method assumes that all the trajectories are absolutely one dimensional. It assumes each molecule takes a random walk in 1D about its mean position ($x=0$,

y=0). It also assumes that the x and y positions of each molecule are measured to similar levels of precision.^{60,135}

The measured position (x_i, y_i) for a single molecule in one video frame can be written as:

$$x_i = R_i \cos \theta + \delta_i \quad (\text{Eq.4.1})$$

$$y_i = R_i \sin \theta + \delta_i \quad (\text{Eq. 4.2})$$

Where R_i is the actual position along the 1D trajectory (i.e., error free), θ corresponds to the angle (-90° to 90°) of the trajectory segment with respect to the x axis (horizontal direction) in the video frames and thus represents the in-plane orientation of the diffusive motion, δ_i is the localization error in the position of the molecule. The mean position of each molecule is defined as $\langle R \rangle = 0$.

By considering equation 4.1 and equation 4.2, the measured (x_i, y_i) positions of the molecule can be rewritten as:

$$x_i = X_i + \delta_i \quad (\text{Eq. 4.3})$$

$$y_i = X_i \tan \theta + \delta_i \quad (\text{Eq. 4.3})$$

Where X_i is the best estimate of the actual x position of the molecule. The orthogonal regression analysis produces the best-fit line ($Y_i = X_i \tan \theta$) giving the minimum sum of the squared residuals (SSR) between x_i and X_i , and y_i and Y_i . The error is estimated by drawing a normal to the fitted line from each point. The error is measured across the entire length of the trajectory.^{60,135}

Accordingly, actual positions of the molecules can be defined by:^{60,135}

$$X_i = \frac{x_i + y_i \tan \theta}{1 + \tan^2 \theta} \quad (\text{Eq. 4.4})$$

$$Y_i = \frac{x_i + y_i \tan \theta}{1 + \tan^2 \theta} \tan \theta \quad (\text{Eq. 4.5})$$

The best-fit line ($Y_i = X_i \tan \theta$) produces the minimum SSR represented by: ^{60,135}

$$\text{SSR} = \frac{1}{n} \sum_{i=1}^n [(x_i - X_i)^2 + (y_i - Y_i)^2] = \frac{1}{n(1 + \tan^2 \theta)} \sum_{i=1}^n (y_i - x_i \tan \theta)^2 \quad (\text{Eq. 4.6})$$

The fitted $\tan \theta$ is found by setting the derivative of SSR with respect to $\tan \theta$ equal to zero: ^{60,135}

$$\tan \theta = \frac{(S_{yy} - S_{xx}) + \sqrt{(S_{yy} - S_{xx})^2 + 4S_{xy}^2}}{2S_{xy}} \quad (\text{Eq. 4.7})$$

In equation 4.7, S_{yy} , S_{xx} and S_{xy} are defined as,

$$S_{yy} = \frac{1}{n} \sum_{i=1}^n y_i^2$$

$$S_{xx} = \frac{1}{n} \sum_{i=1}^n x_i^2$$

$$S_{xy} = \frac{1}{n} \sum_{i=1}^n x_i y_i$$

The finite noise level of the fluorescence profile (i.e., the spot) produced by each molecule leads to a finite localization error for each molecule. However, this is not the only source of error in the measurement. The additional error can arise from the deviation of molecule position from a true 1D trajectory path. This type of error can result from irregularity in the nanochannels, reflecting bends or kinks in these channels. Furthermore, it is well known that probe molecules can cross between neighboring channels in mesoporous silica materials, apparently by passing through defects in the pore walls. ^{24,125}

The following equation offers the positional variance (i.e., the errors in determining x_i and y_i) for each trajectory due to the deviations above from a 1D trajectory^{60,135}

$$\sigma_{\delta}^2 = \frac{S_{yy} - 2S_{xy} \tan \theta + S_{xx} \tan^2 \theta}{1 + \tan^2 \theta} \quad (\text{Eq. 4.8})$$

Furthermore, the variance in the tangent of the estimated trajectory angle can be determined from equation 4.6, and the trajectory angle error can be obtained from equation 4.7.^{60,135} These parameters provide the means to assign trajectories produced by moving molecules to 1D and 2D populations.

$$\sigma_{\tan \theta}^2 = \frac{\sigma_{\delta}^4 \tan^2 \theta + S_{xy} \sigma_{\delta}^2 \tan \theta (1 + \tan^2 \theta)}{n S_{xy}^2} \quad (\text{Eq. 4.9})$$

$$\sigma_{\theta} = \sigma_{\tan \theta} \cos^2 \theta \quad (\text{Eq. 4.10})$$

In equation 4.9, n is the number of data points in each trajectory, while σ_{θ} is the error in the trajectory angle, in equation 4.10.

4.5.2 Trajectory Angle Order Parameter

Valuable information on nanopore order can be obtained by observing the orientations of the nanopores in nanostructured materials. This information is frequently accomplished using static imaging data obtained from electron microscopy images or X-ray scattering data. (cite our JPCLett review). Unfortunately, such data provide little information on the ability of these materials to support mass transport in 1D along any particular direction. A primary objective of the work reported in this dissertation was to use SMT methods to observe and characterize 1D mass transport in nanostructured materials, based on the motions exhibited by single probe molecules.

As discussed above, single molecule motions are ultimately obtained as trajectories showing the rate and direction of these motions.

Importantly, the trajectories obtained in the analysis of single molecule motions can be further analyzed and used to calculate an order parameter for local regions of a particular sample. The order parameters obtained afford a quantitative measurement of the complete distribution of open channel alignments in the region being characterized. Specifically, the order parameter provides a measure of the width of the trajectory angle distribution for the region of interest. In a selected sample region, the orientation of the individual pores or nanochannels are directly identified by the orientations of the individual trajectories. By determining the deviations of the individual trajectories from their mean orientation in the region of interest, the order parameter describing the degree of trajectory alignment is obtained. The second Legendre polynomial (i.e., Eq. 4.11) provides the universal ensemble order parameter for systems of spherical symmetry.

$$S = \frac{1}{2}(3\langle \cos^2(\Delta\theta) \rangle - 1) \quad (\text{Eq. 4.11})$$

Where $\Delta\theta$ is the angular deviation of individual cylindrical pores in a given sample region, and $\langle \rangle$ represents the average over the selected population, region, or sample domain. S can fall anywhere in the range of $-1/2 - 1$. Isotropically ordered pore structures exhibit $S = 0$. $\Delta\theta = \bar{\theta} - \theta$ where $\bar{\theta}$ represents the mean trajectory orientation.¹⁴³

For systems of cylindrical symmetry (i.e., mesopores oriented in a planar sample),¹⁴³ the 2D order parameter is more appropriate for defining materials order. In this case, the order parameter is defined by equation 4.12.

$$\langle P \rangle = 2\langle \cos^2(\Delta\theta) \rangle - 1 \quad (\text{Eq. 4.12})$$

Here, $\langle P \rangle = 1$ indicates perfectly ordered populations are present, while $\langle P \rangle = 0$ for totally disordered populations.¹⁴³

4.5.3 Emission Polarization Measurements

As the name implies, single molecule tracking (SMT) is used to follow and observe the translational motions of individual fluorescent molecules. As discussed above, these measurements allow for 1D trajectories to be assigned and order parameters for organized nanopore domains to be quantified. However, single molecule data can also be used to access additional quantitative parameters describing the nanoscale properties of porous materials. For example, the dye molecules used to probe the 1D orientations of the nanochannels can also be used to obtain information on the accessible pore diameter. A number of different methods can obtain this information. One such method involves characterizing the wobbling motions of the individual molecules tightly confined to the nanopores.

The wobbling motions of individual molecules are readily detected and quantified by characterizing the polarization of the fluorescence emitted by the probe molecules. This polarization imaging was done in this dissertation by employing single molecule emission polarization (SMEP) methods. SMEP methods work for one-dimensionally (1D) moving molecules for which both the trajectory orientation and the degree of emission polarization can be simultaneously measured.¹⁴⁶ Note that most of the molecules tracked in this dissertation emit strongly polarized light as they diffuse within 1D nanochannels. However, a subtle depolarization of the fluorescence from the probe dye molecules was readily detected. It is this subtle depolarization that reflects their wobbling motions.

There are a few possible mechanisms that can result in emission depolarization for single molecules. In this dissertation, “wobbling” of confined dye molecules inside the nanochannels was identified as the main element causing the depolarization of fluorescence emission. However, the microscope itself can also cause depolarization of the collected emission via optical effects in the high NA objective, and due to the polarization characteristics of the dichroic mirrors.¹⁴³ The effects from these components need to be considered and incorporated into the models employed to understand the emission depolarization in detail.

A simple model and analysis method were developed earlier by our group to determine the wobbling-induced depolarization quantitatively, and the associated wobbling angle exhibited by probe dye molecules diffusing through surfactant-templated mesoporous silica.²⁷ The expected wobbling motion is shown in Figure 4.5, where the maximum wobbling angle is defined by θ_{\max} .

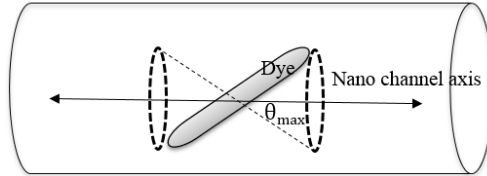


Figure 4.5 Wobbling motion of dye molecule inside a nanochannel.

The process of determining the wobbling angle for each molecule first involves a careful analysis of the emission intensity of each molecule in the pairs of orthogonally polarized images obtained by SMEP. The following equations provide the expected signal levels in each of the two channels for a given wobbling angle.²⁷

$$\bar{I}_V \propto \cos^2 \phi (1 - \cos^3 \theta_{\max}) + \frac{1}{2} (a^2 + \sin^2 \phi) \times (2 - 2 \cos \theta_{\max} - \cos \theta_{\max} \sin^2 \theta_{\max}) \quad (\text{Eq. 4.13})$$

$$\bar{I}_H \propto \sin^2 \phi (1 - \cos^3 \theta_{\max}) + \frac{1}{2} (a^2 + \cos^2 \phi) \times (2 - 2 \cos \theta_{\max} - \cos \theta_{\max} \sin^2 \theta_{\max}) \quad (\text{Eq. 4.14})$$

Where θ_{\max} is the maximum wobbling angle and ϕ is the average orientation of each molecule. The I_V and I_H parameters represent the measured emission intensities of each molecule in the vertical and horizontal polarization channels, respectively. The parameter a^2 represents the depolarization produced by the high NA objective. For this dissertation, a^2 was estimated to be ~ 0.44 for a 1.49 NA objective by applying a model published earlier.¹⁸ The effect of the dichroic mirrors causes only slight variations in the detected intensity with average orientation.²⁷

Furthermore, the effect of the dichroic mirrors is greatest for 45° oriented trajectories, for which there is no sensitivity to the wobbling motions, and it gives the smallest errors for 0° and 90° oriented trajectories, where the measurement is most sensitive to wobbling.

It is known that when dye molecules emit fluorescence light into an anisotropic medium, their emission also depends on their orientation relative to the optical axis.^{27,39} This effect was neglected in the experiments conducted for this dissertation. The effect was believed to be small for surfactant filled mesoporous silica materials because the refractive index associated with the surfactant filled mesoporous silica was close to that of the silica itself, giving a sample that closely resembles an optically isotropic system.^{27,144}

The fluorescence polarization, given as the frame averaged linear emission dichroism (LD) in equation 4.15 is the parameter ultimately used to determine the wobbling angle.²⁷

$$LD = \frac{\bar{I}_V - \bar{I}_H}{\bar{I}_V + \bar{I}_H} \quad (\text{Eq. 4.15})$$

The degree of molecular wobbling can be calculated by using the LD values, and the average orientation of each molecule as follows by equation 4.16:²⁷

$$\langle \cos^2 \theta \rangle = \frac{\cos(2\phi) + LD(2a^2 + 1)}{3\cos(2\phi) + LD(2a^2 - 1)} \quad (\text{Eq. 4.16})$$

The $\langle \cos^2 \theta \rangle$ represent the orientational motions of the molecule that take place on time scales much shorter (i.e., <microseconds) than the video frame time (~0.3 s). The maximum wobbling angle, θ_{\max} , is related to $\langle \cos^2 \theta \rangle$ by the following expression:²⁷

$$\langle \cos^2 \theta \rangle = \frac{1}{3} \left(\frac{1 - \cos^3 \theta_{\max}}{1 - \cos \theta_{\max}} \right) \quad (\text{Eq. 4.17})$$

Chapter 5 - Spectroscopic and Polarization-Dependent Single-Molecule Tracking Reveal the One-Dimensional Diffusion Pathways in Surfactant-Templated Mesoporous Silica

Reproduced with permission from American Chemical Society.

Published as: Ruwandi Kumarasinghe, Eric D. Higgins, Takashi Ito and Daniel A. Higgins

J. Phys. Chem. C, 2016, 120, 715–723.

Contributions of Authors

I was responsible for the preparation of surfactant templated mesoporous silica samples. I carried out the calibration of the Nile red response. Also, I was responsible of carrying out single molecule imaging, data analysis and summarization. Eric D. Higgins performed the Monte Carlo simulations of the dye molecules in model pores. Prof. Daniel Higgins and Prof. Takashi Ito guided the research. They provided indispensable help for the publication of this work.

5. 1 Introduction

Solvent- and surfactant-filled mesoporous silica materials¹ find a wealth of potential applications as models for self-assembly in confined geometries,² and as porous media for solution-phase catalysis³⁻⁵ and chemical separations.⁶⁻⁸ Interactions of incorporated reagents and analytes with the pore-filling medium and pore surfaces govern the molecular level mechanisms of mass transport within such materials.⁹ The transport of reagents and analytes is most efficient when they can explore the full pore diameter, readily moving between central and near-surface pore regions. Likewise, these same factors play an integral role in defining the selectivity of chemical separations in mesoporous silica. However, confinement of liquids within nanometer-size pores often leads to changes in their properties.¹⁰⁻¹⁴ Among other factors, these properties variations may arise from interactions of the liquids with the pore walls.¹¹ In the case of solvent mixtures, spontaneous demixing of the different components on nanometer length scales also

contributes to this complexity.¹⁰ Because of their inherent nanostructure, surfactant micelles exhibit significant variations in properties along their radial dimensions. In surfactant-filled silica mesopores, the micelle/ pore interface is expected to be relatively hydrophilic, while micelle core regions at the center of each pore should be nonpolar and hydrophobic.¹ Such nano-structuring of the pore filling medium is expected to play a profound role in limiting the motions of reagents, analytes, or probe molecules (i.e., solutes) dissolved within the pores, confining their motions to specific nanoscale sub regions within even the smallest pores. The confinement of solute molecules within individual mesopores is inherently difficult to investigate because of the nanometer (and smaller) length scales over which confinement occurs. The effects of solute confinement in mesoporous materials have been explored previously by nuclear magnetic resonance^{15,16} and electron spin resonance methods.¹⁶⁻¹⁸ These studies revealed a slowing of probe motions in solvent filled pores. Fluorescence methods have also revealed a slowing of solute motions as a result of confinement.^{9,19-21} Unfortunately, the exact location of the probe molecules within the pores has been difficult to ascertain. The impacts of probe location have been explored in liquid crystal mesophases²² and in surfactant-templated silica^{23,24} by employing two or more fluorescent probes that partition differently between polar and nonpolar regions. Unfortunately, such methods do not allow for the location of individual probe molecules to be explicitly identified. To date, the most detailed molecular level information on solute confinement within silica mesopores has been obtained by computer modeling.^{25,26} We have recently employed single molecule emission polarization (SMEP) methods to explore the diffusive translational and orientational motions of perylene diimide (PDI) dyes within the cylindrical, solvent-, and surfactant-filled pores of spin-coated mesoporous silica films.^{27,28} In these studies, the diffusion coefficients for translational probe motions within the one-dimensional (1D) pores were found to be $\sim 10^3$ -fold smaller than those in bulk solution, consistent with strong confinement of the dye.^{8,29} However, the most interesting results were obtained from the polarization dependence of dye

fluorescence. These data revealed that the orientational motions of the dye were also tightly confined. Specifically, the dye molecules were found to diffuse along the cylindrical pores with their long axes aligned parallel (on average) to the long axis of each pore. While Brauchle and co-workers had reported similar results for terrylene diimide dyes,³⁰ strong orientational confinement of the smaller PDI dyes was not originally expected. The physical diameter of the pores was estimated to be ~ 3.7 nm, while the longest PDI molecules employed were only ~ 2.8 nm in length.²⁸ In fact, the original measurements showed that the longest PDI molecules were confined to “wobble” within a cone of $\sim 20^\circ$ maximum half angle.²⁸ This wobbling angle was consistent with confinement of the dye to

Only ~ 1 nm diameter pathways within the pores. While the experimental evidence for molecular confinement was clear in these previous studies, the exact origins of confinement were not. It was concluded that the 1D diffusing molecules were restricted to the hydrophobic cores of the surfactant micelles filling the pores.^{27,28} However, the PDI dyes could instead have been confined near the surfactant–silica interface, where steric effects alone would restrict their orientational motions. In fact, previous ensemble studies of dye wobbling within spherical surfactant micelles have attributed orientational confinement of the dye to its incorporation in restricted environments near the micelle surface.³¹ In reality, no direct evidence for the location of the PDI molecules was obtained in our earlier studies. In this Article, we explore the origins of probe molecule confinement within the solvent- and surfactant-filled pores of mesoporous silica films in greater depth by employing the dye Nile Red (NR) as a probe molecule. NR was selected because of its sensitivity to the polarity of its local environment.³² Indeed, NR is one of the most polarity-sensitive probes known that is also sufficiently fluorescent to detect at the single molecule level.^{33,34} NR has been employed previously to determine the local polarity in surfactant assemblies by ensemble methods.^{31,35–37} In the present study, the location of the individual NR molecules was determined by spectroscopic single molecule tracking (sSMT). Fluorescence

videos depicting the diffusive motions of NR within the silica mesopores were simultaneously recorded in two spectral bands ($\sim 580 \pm 40$ and $\sim 625 \pm 40$ nm). Comparisons of the results obtained from the single molecules to those in bulk solution were then used to quantitatively determine the polarity, and hence the identity of the environments through which each molecule diffused. Fluorescence videos depicting NR motions in the same samples were also acquired for two orthogonal emission polarizations. These data were used to determine the orientation of the NR molecules within the pores and to quantitatively assess their level of orientational confinement. By comparison of the NR results with those obtained in previous studies of PDI dyes,^{27,28} additional evidence on the diffusion pathways of the latter molecules within the solvent- and surfactant-filled silica mesopores was obtained.

5. 2 Experimental Section

5. 2. 1 Sample Preparation

Surfactant-filled mesoporous silica films incorporating hexagonally ordered cylindrical pores were prepared by spin coating surfactant-templated silica sols onto glass coverslips. The silica sols were prepared by first dissolving tetramethoxysilane (TMOS, 99% Sigma-Aldrich) in ethanol. Deionized water (18 M Ω cm, Barnstead B-pure) and HCl (0.1 M) in deionized water were subsequently added to initiate hydrolysis and condensation of the alkoxy silane. After addition of water and HCl, the sols were stirred for 1 h and then aged for 24 h in a desiccator. At this point, cetyltrimethylammonium bromide (CTAB, $\geq 99\%$ Sigma-Aldrich) was added to the sol. The NR dye used for single molecule tracking was also added at this point. The final molar ratio of TMOS:ethanol:water:HCl:CTAB in each sol was 1.00:48.2:17.6:0.0091:0.204. The sols were next stirred for an additional 1 h and then spincoated onto plasma-cleaned glass coverslips at 3000 rpm for 30 s. The thin films obtained were aged for 24 h to a few days in a desiccator prior to characterization. The solvatochromic dye Nile Red (NR) was employed as a spectroscopic probe

of the microenvironments inside the surfactant-filled silica pores. NR was obtained from SigmaAldrich and was used as received. Its structure is shown in Figure 5.1. Each sol was doped to a concentration of ~ 2.9 nM by adding 150 μL of an ~ 200 nM ethanolic solution of NR to the sol.

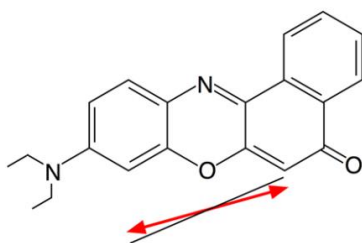


Figure 5.1 Nile Red structure. The red arrow depicts the orientation of the transition dipole for the lowest energy electronic transition. The transition dipole deviates from the long molecular axis (black line) by only $\sim 7^\circ$. The molecular axis was identified by fitting the positions of the atoms comprising the molecule, using orthogonal regression methods. Reprinted with permission from Ref (146) Copyright © 2016, American Chemical Society.

5.2.2 Quantum Mechanical Calculations

Electronic structure calculations were performed on Nile Red (NR) to determine the orientation of the transition dipole moment for its lowest energy electronic transition. The GAMESS software package was employed for optimizing the structure and modeling the electronic properties of NR.⁵⁵ NR was first constructed and its structure initially optimized using the Avogadro software package.⁵⁶ Its structure was then fully optimized in GAMESS at the Hartree-Fock level, using the 6-31G basis set. The electronic orbitals were also obtained at the same level of theory. The electronic transitions were obtained from a full configuration interaction using the graphical unitary group approach at the single excitation level. Table 5.1 gives the parameters obtained for first four electronic transitions. Figure 5.2 displays the optimized NR

structure and the HOMO, LUMO and LUMO+1 orbitals. The lowest energy electronic transition involves promotion of an electron from the HOMO to a combination of orbitals dominated by the LUMO and LUMO+1.

The ground and excited state dipole moments for NR were found to be 7.5 Debye and 12.5 Debye, respectively, values that compare favorably with previously-reported experimental and theoretical results.^{57,48,49} The ~ 5 Debye increase in the dipole moment upon excitation of NR explains its strong sensitivity to solvent polarity.³² The transition dipole associated with the lowest energy electronic transition was determined to deviate from the long axis of the molecule by ~ 7°. The long axis of NR was assigned by fitting the positions of all atoms to a line using orthogonal regression methods.^{58, 59, 60}

<u>Transition</u>	<u>Energy^a</u>	<u>Wavelength^b</u>	<u>Trans. Dipole^c</u>	<u>Osc. Strength</u>
1 ^d	3.41	364	8.03	0.834
2	4.30	289	0.53	0.005
3	4.57	271	0.12	0.000
4	4.69	264	1.47	0.039

Table 5.1. Electronic transitions of Nile Red obtained from GAMESS modeling using the 6-31G basis set. ^a Energy is given in eV, ^b wavelength is in nm and ^c transition dipoles in Debye. ^d The first transition represents the transition probed in the spectroscopic and single-molecule experiments.

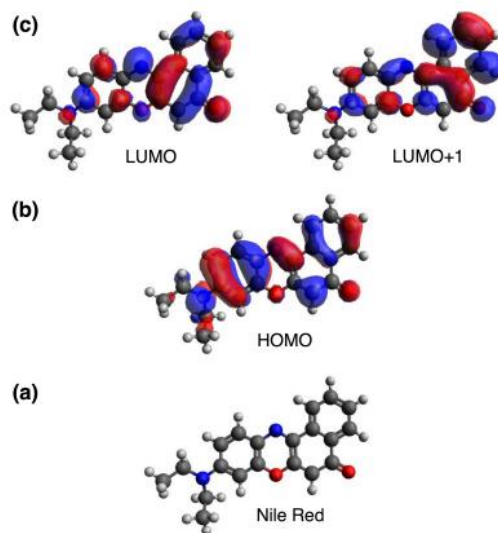


Figure 5.2 (a) Optimized geometry of the Nile Red molecule. (b) HOMO representation for Nile Red. (c) LUMO and LUMO+1 representations. The lowest energy electronic transition in Nile Red is characterized primarily as a HOMO to LUMO and LUMO+1 transition. Reprinted with permission from Ref (146). Copyright © 2016, American Chemical Society.

5.2.3 Partition Coefficient Measurements

The octanol-water partition coefficient for NR was determined by filling a 125 mL separatory funnel with a 25 mL aliquot of 2.5 μ M NR solution in n-octanol and 25 mL of deionized water. The solution was then vigorously shaken for ~ 5 min, after which the solutions were allowed to separate for a period of 1.5 h. The water was then drained, a second aliquot of water added and the extraction repeated. A total of 5 extractions were performed with fresh volumes of water. After the final extraction, the octanol was drained from the separatory funnel and the absorbance of NR was measured in a 1 cm pathlength cuvette at 535 nm. All procedures were performed at ~ 23 °C.

5.2.4 Monte Carlo Simulations

Simulations of the orientation distribution expected for NR within an empty 3.5 nm diameter model silica pore were performed using software written in house.⁵⁴ In these simulations, random central positions and orientations were generated for each molecule within the pore. The pairwise interaction energies between the NR atoms and those of the pore were then determined using a Lennard-Jones potential. The σ and ϵ values employed to define the interaction distances and energies are given in Tables 5.2, 5.3. The Lennard-Jones parameters used for interactions between pairs of different atoms were obtained using the Lorentz-Berthelot combining rules.¹³ The Metropolis Algorithm⁵⁴ was employed to accept or reject each molecular configuration within the pore, using a temperature of 298K. Convergence of the results was verified by repeating the simulations multiple times for varying numbers of attempts up to 3×10^5 .

<u>Atom</u>	<u>σ (Angs)</u>	<u>ϵ (kcal/mol)</u>
Si	2.500	0.0001
O	2.700	0.4569
H(OH)	1.295	0.0004
O(OH)	3.070	0.1700

Table 5.2. Lennard-Jones parameters for all pore atoms.⁶⁸

<u>Atom</u>	<u>σ (Angs)</u>	<u>ϵ (kcal/mol)</u>
C	3.400	0.086
H	2.650	0.015
N	3.250	0.170
O	2.960	0.210

Table 5.3. Lennard-Jones parameters for all NR atoms.⁶⁸

5. 2. 5 Single Molecule Tracking

All samples were imaged on a wide-field epifluorescence microscope that has been described previously.³⁸ In each case, the sample was mounted on the microscope and then immediately covered with a Plexiglas chamber. The chamber was purged with a mixture of water and ethanol

(8:3) vapor in N₂ gas. The gas flow rates were set to maintain an ambient relative humidity of 70% at ~22 °C. All samples were exposed to this vapor mixture for ~30 min prior to imaging and were maintained under the same atmosphere during imaging. These conditions facilitated formation of organized mesopore domains³⁹ and also mobilized the dye molecules within the pores.²¹ The NR dye was excited by 514 nm laser light. Prior to directing it into the microscope, ~2 mW of the excitation light was first passed through a spinning optical diffuser. It was subsequently reflected from a dichroic beam splitter (Chroma 555 DCLP) and then focused into the back aperture of an oil immersion objective (1.49 numerical aperture, Nikon APO TIRF, 100×). The objective produced a broad illumination pattern in the sample, allowing for ~15 × 15 μm² regions to be imaged. The fluorescence emitted by the dye molecules was collected in reflection by the same objective and directed back through the dichroic beam splitter. In SMEP experiments, the fluorescence was subsequently directed through a 580 nm (Chroma HQ 580/40) bandpass filter, while in the case of sSMT studies, a 570 nm colored glass long-pass filter (Schott Glass) was employed. The fluorescence was then directed into an image splitter (Cairn Research OptoSplit II). In SMEP studies, the incident laser light was circularly polarized, and the image splitter was fitted with a polarizing beam splitter. The latter divided the collected fluorescence into two image channels having orthogonal polarizations. Fluorescence in these image channels was simultaneously detected using an electron-multiplying CCD camera (Andor iXon DU-897). In sSMT studies, a beamsplitter cube incorporating a second dichroic mirror (Chroma 605 DCLP) and two bandpass filters was employed. The latter divided the fluorescence into two image channels centered at ~580 and ~625 nm, respectively, each having a ~40 nm passband. Fluorescence in these image channels was simultaneously detected using an electron-multiplying CCD camera (Andor iXon DU-897). Fluorescence videos depicting the single molecule motions were acquired as movies 200–500 frames in length at frame rates of ~10 frames/s, using an electron multiplying gain of 30.

5. 2. 6 Trajectory Analysis

Single molecule trajectories were obtained from the videos by locating, fitting, and tracking the fluorescent spots produced by each molecule using LabView-based software written inhouse. Briefly, fitting the pair of fluorescent spots produced by each molecule (i.e., in the vertical and horizontal polarization images or in the 580 and 625 nm images) to Gaussian functions provided the location of each molecule in the sample plane and the amplitude of its emission profile in each image. The spot locations obtained across a series of video frames were subsequently linked into trajectories depicting the pathways followed by each molecule. A variant of well-known cost functional linking methods⁴⁰ was employed to obtain the trajectories.

5.2.7 Assessing Molecular Mobility and Dimensionality of Motion

Separation of the trajectories into mobile and immobile populations and the former into 1D and 2D diffusing populations was accomplished by first estimating the localization precision for each molecule, using the method reported by Thompson, et al.⁶¹ The amplitudes of the fitted spots were used to determine the total number of photons detected from each spot. The standard deviation of the background counts, determined from regions where no molecules were found, was used to estimate the effective background count level. The calibrated pixel size in the videos was 125 nm, as determined from images of hexagonal arrays of 1 μm diameter fluorescent polystyrene beads. These parameters yielded common localization precisions, σ , of ~ 20 nm. Further analysis of the trajectory data was accomplished by previously-reported orthogonal regression methods.³⁸ Among other useful parameters, this analysis provides measures of the localization variance, σ_s^2 averaged across each trajectory, and the motional variance, σ_R^2 due to molecular diffusion along a 1D pathway. Molecules having $\sigma_s^2 \leq 4.6 \sigma^2$ were assigned to the immobile population, while all others were classified as mobile. Of the mobile molecules, those having $\sigma_R^2 \geq 4.6 \sigma_s^2$ were classified as diffusing in 1D, while all others were classified as 2D diffusing molecules.

5. 3 Results and Discussion

5.3.1 Spectroscopic Single Molecule Tracking (sSMT)

The polarity of the microenvironments probed by the individual NR molecules was determined by analysis of the two-color sSMT data, as originally reported by Giri et al.,⁴¹ based on prior work by Hess et al.⁴² Related methods have also been employed in ensemble studies of local polarity in surfactant and micellar solutions.³⁷ As a first step in this analysis, the spectral response of NR to environments of different polarity was explored using a series of bulk ethanol/hexane mixtures. The solution-phase NR response was recorded on the same microscope used in the sSMT experiments. In these experiments, NR solutions were used to fill a specially designed liquid cell that was mounted over the microscope objective. Fluorescence videos were then acquired from each solution. The background-subtracted average signals in the 580 and 625 nm image channels were determined from these data for each solution in the series. The emission ratio, E , for each solution was then calculated, as defined in eq 5.1

$$E = \frac{I_{625} - I_{580}}{I_{625} + I_{580}} \quad (\text{Eq 5.1})$$

Figure 5.3 plots the average E values obtained from five replicate experiments performed on three different days. As is apparent from these data, NR yields E values that are linearly dependent on the Clausius–Mossotti factor, $(\epsilon - 1)/(2\epsilon + 1)$ (CM factor), of the solvent mixture.^{41,42} While a second term based on the optical frequency dielectric constant is usually included in such relationships,³⁷ the refractive index of hexane (1.38) is similar to that of ethanol (1.36), allowing this term to be included as a constant. The relationship between E and the CM factor was obtained by fitting these data to eq 5.2.

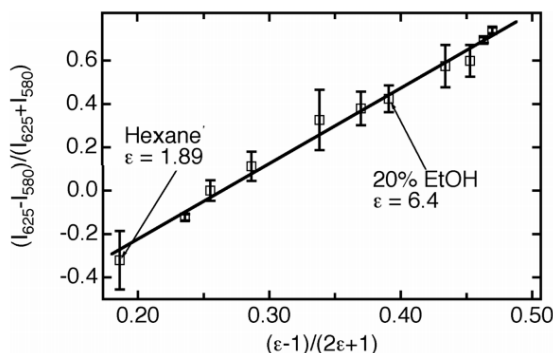


Figure 5.3 Nile Red emission ratio $(I_{625} - I_{580})/(I_{625} + I_{580})$ as a function of the CM factor for a series of ethanol/hexane mixtures. These data were acquired on the same microscope and employed the same filter sets as the single molecule data. The data points show average values and standard deviations obtained from five replicate measurements performed on three separate days. From the left, the solution compositions are 0%, 2%, 3%, 5%, 10%, 15%, 20%, 40%, 60%, 80%, and 100% ethanol (by volume), with the remainder being hexane. The NR concentration in each case was 2 μ M. Reprinted with permission from Ref (146). Copyright © 2016, American Chemical Society.

$$E = K \left(\frac{\epsilon - 1}{2\epsilon + 1} \right) + C \quad (\text{Eq 5.2})$$

The fitted data yielded $K = 3.48 \pm 0.13$ and $C = -0.92 \pm 0.05$. These parameters were subsequently applied in the analysis of the sSMT data (see below) to determine the apparent CM factor for the microenvironment surrounding each molecule. The CM factor is used here as a representation of the effective local polarity. Its value ranges from ~ 0.5 in very polar environments to ~ 0.19 in nonpolar environments as in n-hexane.

Figure 5.4 shows representative two-color wide-field fluorescence video data obtained from NR-doped mesoporous silica films. These videos are displayed as Z-projection images produced by plotting the maximum signal detected at each pixel across the length of the video. The prevalence of 1D “streaks” in the Z-projection images reveals a significant level of 1D diffusion by the NR molecules. This observation confirms that the molecules are largely confined within the

surfactant-filled 1D silica pores, as was also the case for the PDI dyes investigated previously.^{27,28} A significant number of apparently immobile molecules also appear in the images, in this case, as bright round “spots”. These molecules may be entrapped in the silica matrix, in spherical micelles included in the silica matrix, or adsorbed at the film/air or film/substrate interfaces. Most of the spots and 1D streaks found in these images are brightest in the 580 nm image channel, indicating that $E \leq 0$ and the CM factor is less than 0.26 in many cases. Hence, the majority of mobile and immobile molecules is apparently found in nonpolar microenvironments. Similar images obtained from sample “blanks” in the absence of NR yielded ~ 5 -fold fewer fluorescent spots that also produced ~ 2 -fold weaker fluorescence, on average, than the NR-doped samples. Furthermore, very few of the fluorescent spots in the blanks exhibited clear 1D diffusion.

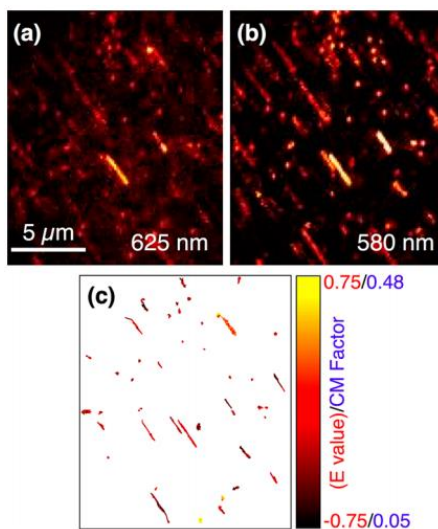


Figure 5.4 (a,b) Z-projection images showing Nile Red motions in a surfactant-templated mesoporous silica film for the 625 and 580 nm detection channels. The video data are provided as Supporting Information. A prevalence of 1D single molecule motions is observed. (c) Single molecule trajectories obtained by tracking the molecules in the same videos. The trajectories are color coded to reflect the emission ratio $(I_{625} - I_{580})/(I_{625} + I_{580})$

and CM factor along each trajectory. Reprinted with permission from Ref (146). Copyright © 2016, American Chemical Society.

A much more quantitative assessment of local polarity, based on eq 5.2, was obtained by tracking the fluorescent spots produced by each molecule across multiple video frames. The total fluorescence counts detected from a given molecule in the 580 and 625 nm image channels were determined by fitting the fluorescent spots to 2D Gaussian functions. The signal levels were obtained as the amplitudes of the fitted spots and were used to calculate E values for each molecule as a function of time and position along its trajectory. This procedure also allowed for precise determination of the location of each molecule in each video frame. These spot locations were subsequently linked into trajectories. As has been reported in previous publications,^{24,38} the trajectories were used to quantitatively assign each molecule to either immobile or mobile populations and to determine the dimensionality of motion for the mobile molecules.

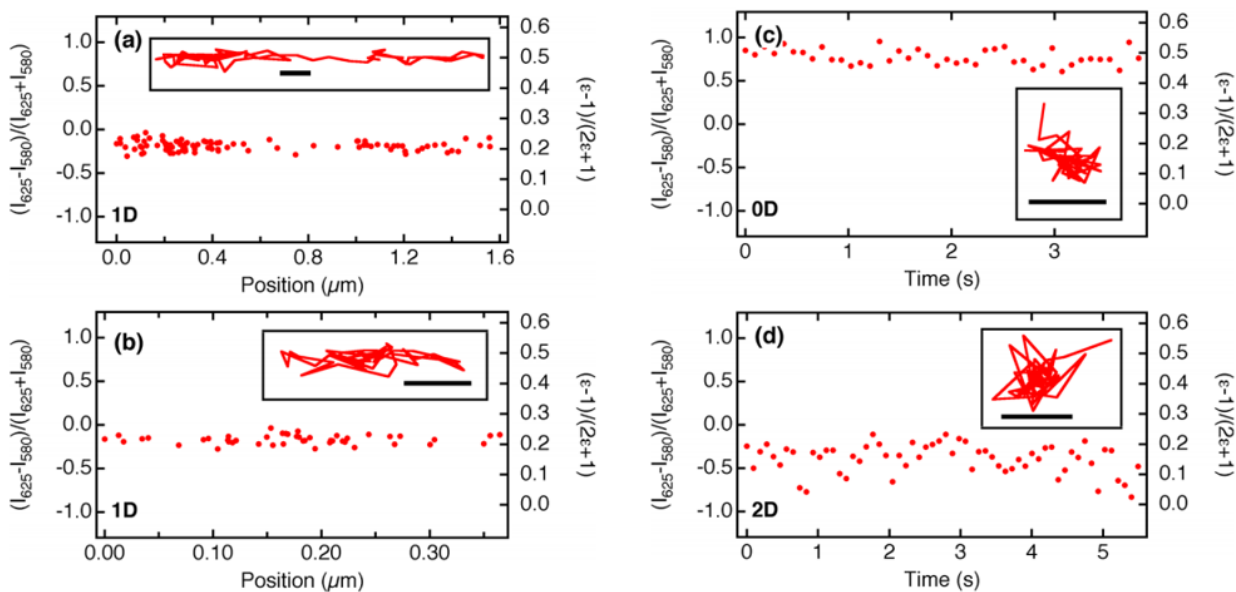


Figure 5.5 (a,b) Emission ratios and CM factors as a function of position for each of two representative 1D trajectories. (c,d) The same values plotted as a function of time for an immobile molecule (0D) and a 2D diffusing molecule, respectively. The insets in each panel

show the trajectories. The scale bars in each inset are 125 nm in length. The 1D trajectories were rotated to appear horizontal for ease of plotting. All data were taken from Figure 5.3. Reprinted with permission from Ref (146). Copyright © 2016, American Chemical Society.

Figure 5.4c plots the trajectories obtained from the video data in Figure 5.4a,b. Only those trajectories ≥ 10 frames in length are shown, and only these were used in subsequent analyses. The individual trajectories again depict the presence of 1D diffusing (streaks) and immobile molecules (spots). The trajectories shown are color coded to depict the E values observed in each video frame, and their associated CM factors. While these data reveal some variability across the region imaged, they also demonstrate that most molecules are found in very nonpolar environments. Representative trajectories extracted from the data in Figure 5.4 are plotted in Figure 5.5, along with their E values and CM factors. Shown are two examples of 1D diffusing molecules, and one each of 2D diffusing and immobile (0D) molecules. The 1D moving molecules both yield $E < 0$ on average, as does the 2D diffusing molecule. The immobile molecule yields $E > 0$, indicating it is entrapped in a more polar environment. None of these plots show any clear time- or position-dependent variations in their E values. The same observation was made for the vast majority of trajectories acquired, suggesting that the individual molecules locate within microenvironments of a certain polarity and remain there on the measurement time scale (~ 100 ms to ~ 10 s). While the lack of variation in environmental polarity might suggest a loss of NR sensitivity, previous results probing the properties of organically modified silica polarity gradients demonstrate that NR remains sensitive to local polarity in/on solid materials.⁴¹

Histograms showing the distributions of E values and CM factors obtained from the sSMT data are provided in Figure 5.6. Shown in panels a, b, and c are results from immobile, 1D diffusing, and 2D diffusing molecules, respectively. These data were compiled from single-frame measurements of the fluorescence from a large number of single molecules. They reveal some

important differences in the environments experienced by the immobile, 1D, and 2D diffusing molecules. The main components of the distributions shown in Figure 5.6 have been fit to Gaussian functions to facilitate discussion of the properties of these environments.

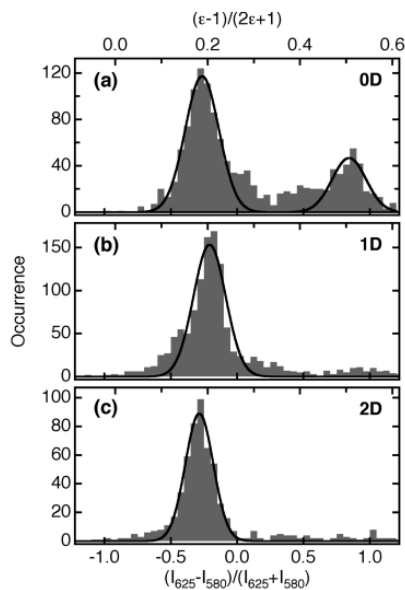


Figure 5.6 (a–c) Single frame emission ratios and CM factors for immobile (0D), 1D, and 2D diffusing molecules, respectively. The solid black lines show fits of the main populations to Gaussian functions. Reprinted with permission from Ref (146). Copyright © 2016, American Chemical Society.

First, a significant population of immobile molecules (0D) is found in highly polar microenvironments having CM factors peaked near ~ 0.5 . In contrast, the mobile populations (1D, 2D) incorporate far fewer molecules in such environments. The greater fraction of immobile molecules found in polar environments is readily attributable to molecules entrapped in or adsorbed on the silica matrix, or at the film/air or film/ substrate interfaces. Careful inspection of the trajectories from the mobile molecules associated with these high polarity environments reveals that most are very short in spatial extent and number of video frames, suggesting they may actually represent immobile molecules that are erroneously assigned to the mobile populations. Those that do reflect a real increase in the local polarity may arise from molecules diffusing along

the silica/surfactant interface. No clear evidence of molecules transiting between polar and nonpolar environments could be found in the data. The most significant populations of the immobile, 1D, and 2D diffusing molecules exhibit CM factors consistent with nonpolar microenvironments. Specifically, the immobile population is peaked at a CM factor of 0.188 ± 0.001 , while the 2D diffusing population is peaked at 0.182 ± 0.001 . The 1D diffusing population is peaked at 0.204 ± 0.003 . Taken together, these data reveal that the vast majority of molecules are found in microenvironments with polarities similar to that of n-hexane, which has a CM factor of 0.186.

Interestingly, the population of 1D diffusing molecules in nonpolar microenvironments produces a distribution that is shifted to slightly higher polarity than either of the immobile or 2D diffusing populations. The shift to more polar environments for the 1D diffusing molecules may reflect an increase in the solvent content of the local environment. In particular, the results suggest that more ethanol and/or water may be incorporated in regions that yield 1D diffusion. Indeed, addition of solvents from the vapor phase is required to induce molecular motion in these samples.^{21,30} Hydrogen bonding to solvent molecules has also been shown to produce an ~ 25 nm red-shift in the NR emission spectrum.^{43,44} Thus, the shift in the 1D population may also reflect enhanced hydrogen bonding of NR to the solvent. Unfortunately, distinction between an increase in the local dielectric constant and hydrogen-bonding mechanisms cannot be made using the current data.

Measurements of the diffusion coefficients, D , for the molecules tracked in Figure 5.4 provide supporting evidence that the dye molecules diffuse within highly confined environments. In these measurements, the mean square displacement (MSD) exhibited by each molecule was calculated and plotted as a function of time.⁴⁵ These data were fit to a straight line out to a five-frame delay, with the slope of the line giving the MSD value. Figure 5.7 shows representative plots. The diffusion coefficient was then obtained for each molecule from its MSD value, using D

= $MSD/(2nt)$, where n is the dimensionality of diffusion and t is the video frame time (0.093 s). The mean D value obtained by averaging all results from the 1D diffusing population was $0.08 \pm 0.02 \mu\text{m}^2/\text{s}$, where the error bar gives the standard error on the mean for 51 trajectories. This D value is similar to that measured in fluorescence correlation spectroscopy studies of NR diffusion in related films,²¹ and $\sim 10^3$ -fold smaller than its diffusion coefficient in bulk solution.⁴⁶ Similarly, small D values have also been measured for 1D diffusing PDI dyes in related mesoporous silica films.^{27,38} The 2D diffusing molecules gave even smaller mean D values of $0.0013 \pm 0.0007 \mu\text{m}^2/\text{s}$ (from 27 trajectories).

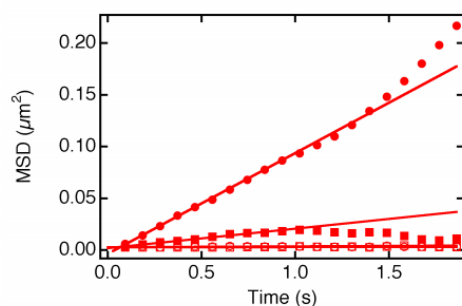


Figure 5.7 Plots of mean square displacement data (symbols) for the four single molecule trajectories shown in Figure 5.5 and their fits (straight lines). The filled circles and squares show data from Figure 5.5a,b while the open circles and squares show data from Figure 5.5c,d. Each data set is plotted out to a 20 frame (~ 1.9 s) delay. Reprinted with permission from Ref (146). Copyright © 2016, American Chemical Society.

From the above observations, it is concluded that the vast majority of NR molecules are confined to the hydrophobic core of the CTAB micelles incorporated within the silica pores. It also appears that their mobility characteristics are determined by the exact morphology of the CTAB assemblies. For example, immobile molecules found in nonpolar environments are likely entrapped within spherical or very short cylindrical micelles. The 2D diffusing molecules may be incorporated in defected film regions that permit passage of molecules through the silica pore

walls,²⁴ or they may be entrapped in film voids or at grain boundaries, all of which likely incorporate CTAB micelles or less well-organized surfactant assemblies. In fact, the diffusion coefficients of this population are only slightly larger than those obtained from the immobile molecules, the latter as a result of the finite localization precision. Therefore, it is likely that many of the 2D diffusing molecules are actually immobile. Finally, the 1D diffusing population exhibits clear evidence for anisotropic motion that is characteristic of their entrapment in cylindrical pores/micelles. The large population of NR molecules found in nonpolar, hexane-like microenvironments in the surfactant-templated silica films is consistent with its solution-phase partitioning behavior.⁴⁷ Here, the NR octanol–water partition coefficient (K_{ow}) was determined by extracting a 25 mL volume of 2.5 μ M NR in n-octanol with five 25 mL volumes of deionized water. The NR absorbance at 535 nm was used to determine K_{ow} after the final extraction. From these studies, K_{ow} was determined to be ~ 40 . This value is consistent with values reported in the literature for other organic solvents.⁴⁷ These results indicate that NR molecules should preferentially locate in nonpolar regions.

The observation that many NR molecules are found in hexane-like microenvironments stands in contrast to the results of previous ensemble studies of its location in micellar solutions.^{31,35–37} In these previous publications, NR was concluded to locate in somewhat more polar environments, often at the micelle–solution interface. This discrepancy may reflect real differences in the materials or it may be due to the significant spatial and temporal averaging of data that occurs in ensemble measurements, relative to single molecule methods. A large number of molecules distributed across a range of different environments are probed by ensemble methods. The spectral data obtained reflect the integrated contributions of all such molecules. In single molecule studies, the microenvironment in which each molecule resides is independently probed, and detailed information on the populations of molecules in microenvironments of different polarity is obtained. Indeed, averaging of all of the polarity data shown in Figure 5.6 to produce an ensemble-

like result reveals that the average molecule is found in a microenvironment that is significantly more polar (CM factor = 0.250) than the most common environment exhibited by the 1D diffusing molecules (CM factor = 0.204).

As a caveat to the above discussion, it should be noted that NR becomes less fluorescent in polar and hydrogen-bonding liquids, as demonstrated by published quantum yield data.^{44,48,49} It also may form non fluorescent dimers at $\sim 10^3$ - fold higher concentrations.³⁷ Therefore, it is possible that the population of single molecules in the most polar environments is under-detected in the present studies. However, the data presented in Figure 5.4 show that the NR signal levels in polar environments (CM factors of 0.45 ± 0.05) are $\sim 70\%$ as large, on average, as those in less polar environments (CM factors of 0.20 ± 0.05). Therefore, it is concluded that the distributions shown in Figure 5.6 very likely reflect the properties of the most common environments probed by NR and are not significantly biased by the aforementioned phenomena.

5.3.2 Single Molecule Emission Polarization (SMEP) Studies.

The sSMT results described above demonstrate that NR preferentially locates within the hydrophobic core of the cylindrical micelles filling the silica mesopores. However, additional data are required to verify that it is confined to the same degree and within the same environments as the previously reported PDI dyes.^{27,28} To this end, polarization dependent wide-field fluorescence video data were also acquired from NR single molecules doped into the silica films. Figure 5.8 presents representative video data and the trajectories obtained. Again, only those trajectories ≥ 10 video frames in length are included in Figure 5.8c. These trajectories were also separated into immobile, 1D, and 2D diffusing populations, as described above, using the methods defined in the Supporting Information. The trajectories shown are color coded to depict the population to which each molecule was assigned. Only those trajectories determined to depict 1D diffusion were employed in the subsequent data analysis as only these can be used to determine the level of orientational confinement. The data shown in Figure 5.8 reveal that the fluorescence from 1D

diffusing NR molecules is strongly polarized along the diffusion direction, exactly as was previously observed for PDI dyes in the same materials.^{27,28} The strongly polarized emission from the single molecules indicates that their orientational motions are tightly confined within the silica mesopores. Quantitative interpretation of the SMEP results in terms of molecular orientation requires knowledge of the transition dipole orientation in the molecular reference frame. While previous modeling studies have explored the solvent dependence of NR emission,^{50,51} the exact orientation of its transition dipole has not been reported to our knowledge. Electronic structure calculations were undertaken to make this determination and are described in the Supporting Information. From these calculations, the transition dipole orientation in NR was estimated to be tilted by only $\sim 7^\circ$ from the “long axis” of the molecule. The black and red lines appended to the NR structure in Figure 5.1 depict its “long axis” and transition dipole orientations, respectively. From this information, and from the SMEP results shown in Figure 5.8, it is concluded that NR diffuses with its long axis aligned approximately parallel to the pore axis, as was also the case for the PDI dyes studied previously.^{27,28}

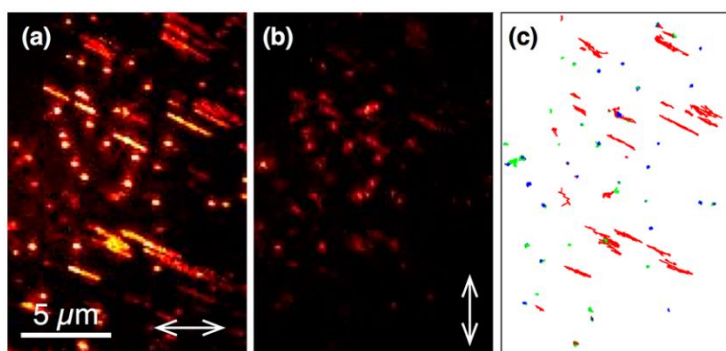


Figure 5.8 (a,b) Z-projection images depicting Nile Red motions in a surfactant-templated mesoporous silica film. The original video data were acquired for the orthogonal emission polarizations designated by the white double-ended arrows. The video is provided as Supporting Information. (c) Single molecule trajectories obtained by tracking the molecules in the same video. The trajectory colors designate immobile (blue), 1D diffusing

(red), and 2D diffusing (green) molecules. These data demonstrate that a large fraction of the NR molecules diffuse in 1D, and that these molecules are confined to diffuse with their long molecular axes oriented approximately parallel to the long axis of each pore. Reprinted with permission from Ref (146). Copyright © 2016, American Chemical Society.

As reported for the PDI dyes,^{27,28} NR also exhibits a subtle depolarization of its fluorescence that may be attributed to a confined “wobbling”^{31,52} of the molecule about its average orientation as it diffuses along the pore. The level of orientational confinement exhibited by NR was quantified by determining the mean “wobbling angle” for each molecule, using methods defined in detail in the original reports describing SMEP measurements.^{27,28} Briefly, this analysis requires fitting each 1D trajectory to a line by orthogonal regression methods,³⁸ to obtain the average in-plane orientation, ϕ , of each pore, and hence the average in-plane orientation of each molecule. The SMEP data also provide quantitative frame-by-frame values for the fluorescence polarization, FP (originally called the emission dichroism^{27,28}). These data are averaged along the trajectory length, and the mean wobbling angle, $\langle\theta\rangle$, is then determined via eq 5.3.⁵³

$$\langle\cos^2\theta\rangle = \frac{\cos(2\phi) + FP(2a^2 + 1)}{3\cos(2\phi) + FP(2a^2 - 1)} \quad (\text{Eq. 5.3})$$

Here, a^2 is a constant (0.44) defined by the numerical aperture of the microscope objective.²⁷ This model assumes the long molecular axis and dipole are parallel to each other, a reasonable approximation for NR given the $\sim 7^\circ$ tilt between the two. Figure 5.9a plots a histogram showing the mean wobbling angles obtained from the 1D trajectories in Figure 5.8, using $\cos^2\langle\theta\rangle \approx \langle\cos^2\theta\rangle$. These data reveal that the wobbling motions exhibited by NR are tightly confined, as they also were for the PDI dyes.^{27,28} The average value for the mean (and maximum, θ_{\max}) wobbling angles in the case of NR was 16° (and 24°), while the shortest PDI dyes exhibited wobbling angles of $\sim 25^\circ$ (and 36°). The maximum wobbling angle is readily related to the accessible pathway

diameter, d , within the pores and the molecular length, L , by $d = L \sin \theta_{\max}$.^{27,28} These parameters yield an apparent pathway diameter of ~ 0.6 nm for NR, which is ~ 1.4 nm in length. This value is very close to the ~ 1 nm value reported for the PDI dyes.²⁸ The slight discrepancy may reflect the precision of the measurements or real differences in the wobbling angles of the dyes.

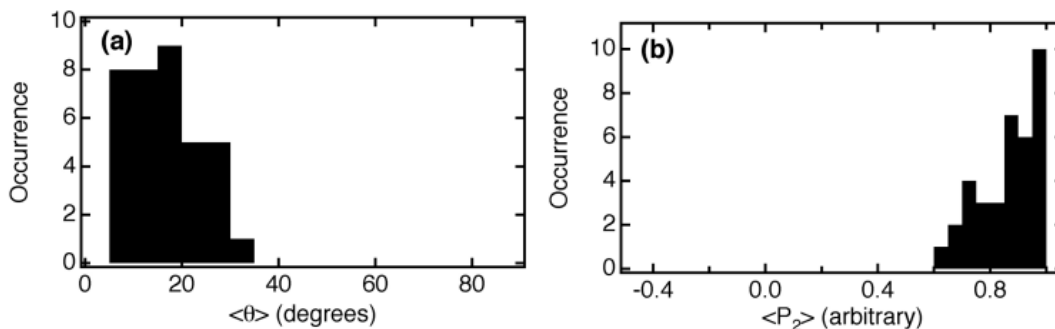


Figure 5.9 (a,b) Histograms showing the distribution of mean wobbling angles and the same data replotted as the orientational order parameter $\langle P_2 \rangle$, respectively, for NR, as derived from Figure 5.8. Reprinted with permission from Ref (146). Copyright © 2016, American Chemical Society.

5.3.3 Monte Carlo Simulations of Nile Red in a Model Silica Pore.

As noted above, strong orientational confinement of the NR and PDI dyes in the CTAB-templated silica pores is somewhat unexpected, because of the small size of these molecules relative to the physical pore size. Again, NR is estimated to be ~ 1.4 nm in length, while the largest of the previously studied PDI dyes was only a factor of two longer.²⁸ The diameter of the silica mesopores is estimated to be ~ 3.7 nm.²⁸ The following figures imply that a broad range of orientations is possible for NR molecules entrapped within the silica pores. The range of orientations expected was obtained through Monte Carlo simulations of NR molecules within a model silica pore. The pore employed is shown in Figure 5.10 a. No solvent or surfactant molecules were included within the pore. Briefly, Monte Carlo methods⁵⁴ were used to generate random NR

positions and orientations within the otherwise empty pore. The interaction energies between the individual NR atoms and those comprising the pore were then determined using a Lennard-Jones potential and summed to determine the total energy of each NR configuration within the pore. NR configurations were accepted or rejected by comparing the total energy to kT , with $T = 298$ K. Figure 5.10a shows one representative example of an accepted NR configuration within the pore. In this case, the long axis of the NR molecule lies approximately perpendicular to the pore axis (perpendicular to the page).

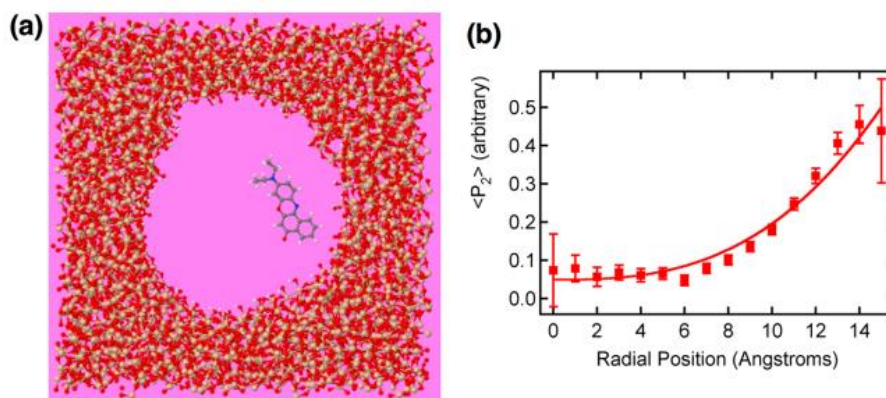


Figure 5.10 (a) Model ~ 3.5 nm diameter silica pore employed in Monte Carlo simulations of NR orientation. A representative NR molecule is shown within the otherwise empty pore. Silicon atoms are shown in orange, oxygen in red, hydrogen in white, carbon in gray, and nitrogen in blue. (b) Results of the Monte Carlo simulations for NR (data points) in the pore shown in (a). The results are displayed as the orientational order parameter (eq 5.4), as a function of radial position from the pore center. Molecules near the center of the pore are almost randomly oriented, while those near the pore wall are preferentially aligned parallel to the pore axis. The error bars depict the 95% confidence intervals about the mean value at each point. These were obtained by splitting the full population of accepted

configurations into 10 subgroups to estimate the standard deviation of replicate simulations.

Reprinted with permission from Ref (146). Copyright © 2016, American Chemical Society.

The results of the simulations show that NR molecules fit within the empty silica pore in a broad range of orientations. The average of the second Legendre polynomial, $\langle P_2 \rangle$, was employed to quantify the level of orientational order:

$$\langle P_2 \rangle = 0.5(3\langle \cos^2(\theta) \rangle - 1) \quad (\text{Eq. 5.4})$$

Here, θ is the tilt angle of the individual NR transition dipoles relative to the pore axis. Note that $\langle P_2 \rangle$ ranges from zero for randomly oriented dipoles to 1.0 for those oriented parallel to the pore axis. By averaging all accepted orientations in the simulations, a value of $\langle P_2 \rangle = 0.13$ was obtained. Figure 5.10b plots the NR orientational order parameter as a function of its radial position within the pore. These data show that NR molecules in the empty pore are only strongly oriented along the pore axis when positioned nearest the pore wall. In this case, $\langle P_2 \rangle \approx 0.5$. It is therefore concluded that steric interactions between the silica pore walls and the NR molecules do not explain the observed level of orientational confinement. Rather, taken together with the polarity measurements reported above, it is most likely that the solvent and surfactant present within the pores play a role in governing NR orientation. This conclusion is supported by previous simulations of a coumarin dye in solvent-filled silica pores reported by Harvey and Thompson.²⁶ Based on these observations, it is concluded that the NR molecules (and the PDI molecules reported previously)^{27,28} must be confined to the central hydrophobic core of the micelles, and that their restriction to this region best explains their orientational confinement.

5. 4 Conclusion

The present studies demonstrate that nanostructuring of the solvent and surfactant medium filling the cylindrical pores of spin-coated mesoporous silica films plays an important role in governing the diffusive translational and orientational motions of incorporated reagents or analytes. The hydrophobic dye NR was used as a model analyte, and through sSMT studies of its mobility and location, it was shown to be tightly confined to regions having polarities similar to that of n-hexane in the CTAB-filled mesopores. It was concluded that the dye molecules were largely restricted to the hydrophobic core regions of the micelles filling the pores, rather than locating near the silica/surfactant interface. The sSMT results suggest that some polar solvent molecules (i.e., ethanol) may have also been incorporated within the micelles. Importantly, the regions to which the molecules were confined were shown to be much smaller than the physical diameter of the pores. The diameter of these pathways was found to be ~ 0.6 nm for the NR dye, a value that is similar to the ~ 1 nm pathway diameter obtained in previous studies of PDI dyes.^{27,28} These results suggest that the micelles filling the pores limit the interactions between the probe molecules and the silica pore walls. Similar phenomena are likely to occur for a broad range of hydrophobic reagents and analytes incorporated within solvent and surfactant-filled porous materials such as those being developed for applications in micelle-mediated catalysis^{4,5} and chemical separations.⁶⁻⁸ Knowledge of such phenomena is of critical importance to understanding the mechanisms governing mass transport and molecule–matrix interactions in solution-phase applications of mesoporous silica and other nanoporous materials.

Chapter 6 - Single-Molecule Tracking Studies of Charged and Neutral Perylene Diimide Probes within Surfactant-Filled Silica Mesopores Reveal Differences in Mass Transport Behavior and Orientational Confinement

6.1 Introduction

Surfactant-templated mesoporous silica has long been investigated as a possible stationary phase for chemical separations and as a useful platform upon which to base studies of the fundamental mechanisms of mass transport within nanoporous media. Mesoporous silica materials incorporating cylindrical pores are best suited for such applications and are typically obtained via the hydrolysis and condensation of alkoxy silane precursors in a liquid sol containing the templating surfactant. The surfactant may be present in sufficient concentration, i.e., above the critical micelle concentration, such that cylindrical micelles are present when the sol is prepared and can directly template cylindrical silica pores. Alternatively, the surfactant molecules may self-assemble into cylindrical micelles as the solvent evaporates from a more dilute sol. In both cases, the cylindrical micelles formed may further assemble into organized mesophases. Polymerization of the silica around the templating micelles leads to the formation of a rigid silica gel incorporating surfactant- and solvent-filled silica pores. These gels can either be obtained as bulk monolithic materials, or they can be spin coated or dip coated onto a substrate to form porous films. The pores within these materials typically range from 2-15 nm in diameter, depending on the surfactant employed, and are at least a few micrometers in length. The surfactant is often removed from the pores to yield the desired mesoporous silica, but it can also be left in place to form silica-encapsulated surfactant micelles that are also of interest for use in chemical separations and surfactant-modified catalysts. They are often oriented in the film plane, which is a distinct advantage for the single molecule tracking experiments described in this dissertation.

In all condensed-phase applications of mesoporous silica materials, the nanopores contained within the gel are necessarily filled with liquids, whether these comprise water or organic liquids condensed from the atmosphere, those remaining from materials preparation, or those purposefully loaded into the materials afterwards. As noted above, the templating surfactants may also remain in place. In all such cases, the materials incorporated within the pores are tightly confined on nanometer length scales. The impact of nanoconfinement on the properties of liquids is an active area of research at present.¹⁴ It is well-known that nanoconfinement of liquids can cause a reduction in their melting points¹³⁶⁻¹³⁸ and can alter the rate of molecular motions.¹³⁹⁻¹⁴² Nanoconfinement of mixtures can also lead to demixing and formation of ordered solvent layers on molecular length scales.¹⁰ The changes imparted on the pore filling medium by nanoconfinement can have a profound effect on the partitioning of solutes to different environments within the pores, the rates and mechanisms of mass transport, and the propensity of the solutes to interact with (i.e., adsorb to) the internal pore surfaces.

Over the last several years, our group and others have employed single molecule tracking methods to explore the mass transport behaviors of fluorescent probe molecules confined within surfactant- and solvent-filled silica mesopores. We have measured the apparent diffusion coefficients of these molecules, and have found them to be orders of magnitude smaller than their diffusion coefficients in bulk liquids. We have shown that the probe molecules frequently exhibit clear 1D motions, consistent with their confinement to the cylindrical silica mesopores. While the pores obtained by templating with cetyltrimethylammonium bromide (CTAB) are expected to be ~ 3.7 nm in diameter, and the probe dyes were much shorter (i.e., < 2.8 nm) in length, we routinely observe that the dye molecules move within the surfactant-filled pores in a highly oriented state, with the long molecular axis aligned parallel to the cylindrical axis of the pore. These observations are made by analyzing the polarization of the fluorescence emitted by each molecule in single molecule emission polarization (SMEP) experiments. However, the SMEP data suggest the

molecular orientation is not perfect, as reflected by a subtle depolarization of the detected emission from the molecules. We have interpreted the observed depolarization to reflect orientational wobbling motions of the dye molecules within the pores. Careful measurements of the fluorescence depolarization have shown that uncharged dye molecules are confined to wobble within a cylinder ~ 1 nm in diameter. Single molecule measurements of the dielectric constant of the medium through which the molecules move have shown the environments to be highly nonpolar, consistent with confinement of molecular motions not by the silica pores themselves, but rather by the surfactant micelles filling the pores.¹⁴⁶ In all cases, the probe dyes employed to date have been uncharged, hydrophobic perylene diimide dyes, or the hydrophobic solvent-sensitive dye Nile Red.¹⁴⁶ It remains to be seen whether more hydrophilic molecules can explore more of the pore volume and are thus less tightly confined.

In the present study, we seek to determine whether charged perylene diimide dyes are less confined within the pores, in comparison to uncharged perylene diimides. To this end, wide-field fluorescence video microscopy is used to follow the motions of both cationic and anionic versions of the perylene diimides loaded into the pores. The results are compared to those obtained from two different uncharged perylene diimide dyes. The fractional populations of molecules found to be immobile, or diffusing in one or two dimensions is compared across the series of four dyes, as are their apparent diffusion coefficients. Single molecule emission polarization (SMEP) measurements are also employed to measure the confined orientational motions of each of the dyes and the results are compared across the series. Taken together, the results obtained reveal that confinement of the dyes does depend on their charge. The mass transport mechanisms for all four dyes are also investigated for the first time in this study. In this case, the distributions of single-frame step sizes are compiled for individual dye molecules and these are used to identify the likely mechanism for diffusion. These results are also used to draw important conclusions about the heterogeneity of the medium found within the silica pores.

6. 2 Experimental Section

6. 2. 1 Sample Preparation

Surfactant-filled mesoporous silica films incorporating hexagonally-ordered cylindrical pores were prepared by spin casting surfactant-templated silica sols onto glass cover slips. The silica sols were prepared by first dissolving tetramethoxysilane (TMOS, 99% Sigma Aldrich) in ethanol. HCl (0.1M) in deionized water (18 M Ω cm, Barnstead B-pure) was subsequently added to initiate hydrolysis and condensation of the TMOS. After addition of water and HCl, the sols were stirred for 1 h and then aged for 24 h in a desiccator. At this point, cetyltrimethylammonium bromide (CTAB, \geq 99% Sigma-Aldrich) was added to the sol. Any one of the dyes used in the single molecule tracking studies (see below) was also added at this point. Sufficient dye was added to yield a concentration of a \sim 2.9 nM by adding 150 μ L of an \sim 200 nM ethanolic solution. The final molar ratio of TMOS:ethanol:water:HCl:CTAB in each sol was 1.00:48.2:17.6:0.0091:0.204. The sols were subsequently stirred for an additional 1 h and then spin coated onto plasma-cleaned glass cover slips at 3000 RPM for 30 s. The thin films thus obtained were aged for more than 24 h in a desiccator prior to characterization.

Four different perylene diimide (PDI) dyes were employed as probes of the silica films. These included symmetrically-substituted uncharged PDI dyes N,N'- bis(octyloxypropyl)-perylene-3,4,9,10-tetracarboxylic diimide (C₁₁OPDI) and N,N'-bis(methoxypropyl)-perylene-3,4,9,10-tetracarboxylic diimide (C₄OPDI), along with a cationic derivative N,N'-bis(2-(trimethylammonio)ethyl)-perylene-3,4,9,10-tetracarboxylic diimide (TAPDI²⁺) and an anionic derivative N,N'-bis(3-sulfonatopropyl)-perylene-3,4,9,10-tetracarboxylic diimide (PDISO₃²⁻). The former was obtained as an iodide salt while the latter was prepared as a sodium salt. All four dyes were synthesized in-house, as described previously.¹⁰² Ethanolic solutions (\sim 200 nM) of each dye were prepared for use in doping of the silica sols (see above).

6. 2. 2 Single Molecule Tracking

All samples were imaged on a wide-field epifluorescence microscope that has been described previously, in detail.³⁸ In each case, the sample was mounted on the microscope and then immediately covered with a Plexiglas chamber. The chamber was purged with a mixture of water and ethanol (8:3) vapor in N₂ gas. The gas flow rates were set to maintain an ambient relative humidity of 70% at ~22 °C. All samples were exposed to this vapor mixture for ~ 30 min prior to imaging and were maintained under the same atmosphere throughout the imaging process. These conditions were employed to facilitate the formation of organized mesopore domains^{21,30,39} and to mobilize the dye molecules within the pores.^{27,28}

The dye molecules were excited by exposure to circularly polarized 488 nm laser light. Just prior to entry into the microscope, the laser light was passed through a spinning optical diffuser. It was then reflected from a dichroic beam splitter (Chroma, 505 DCLP) and subsequently focused into the back aperture of an oil immersion objective (1.49 numerical aperture, Nikon APO TIRF, 100X). The objective produced a broad illumination pattern in the sample, allowing for ~15 × 15 μm² regions to be imaged. The fluorescence emitted by the dye molecules was collected by the same objective and directed through the dichroic beam splitter, and through a bandpass filter (Chroma, HQ535/50m). The fluorescence was then guided into an image splitter (OptoSplit II, Cairn Research) incorporating a polarizing beam splitter that divided the collected fluorescence into two orthogonal polarizations. The two spatially separated images were subsequently directed onto an electron-multiplying CCD camera (Andor iXon Du-897) for detection. An electron-multiplying gain of 30 was employed. Fluorescence videos depicting the single molecule motions were recorded as movies 200 frames in length at a frame rate of ~ 3 frames per second.

6.2.3 Trajectory Analysis

Single molecule trajectories and emission polarization data were obtained from the videos by locating, fitting and tracking the fluorescent spots produced by each molecule using LabView-based software written in-house. Briefly, fitting the pair of fluorescent spots produced by each molecule (i.e., in the vertical and horizontal polarization channels) to a Gaussian function provides the location of each molecule in the sample plane and the amplitude of its emission profile in each image. These spot locations obtained were subsequently linking into trajectories depicting the pathways followed by each molecule using a variant of well-known cost-functional based linking approaches.⁴⁰

6.3 Results and Discussion

In previous studies of spin-coated surfactant-templated mesoporous silica films from our group, fluorescence correlation spectroscopy (FCS) methods were employed to measure diffusion coefficients for a series of uncharged and charged dyes.¹⁷³ The results showed that in CTAB-containing mesoporous silica materials, sulfonated perylene diimide (SPDI) is found to be immobile under all conditions explored, while Nile Red is always mobile and mobility of DiI is dramatically dependent on the level of film hydration.¹⁷³ Unfortunately, these previous studies relied upon dyes having different chromophoric structures, and therefore, the charge character of each dye was not the only factor of importance in governing molecular mobility and dye-surface interactions. For example, hydrophobic effects and hydrogen bonding could have also played a role. In the present studies, uncharged, cationic, and anionic PDI dyes having identical chromophores were employed, largely mitigating the limitations of the earlier work. Furthermore, our previous studies included no conclusive evidence that the dyes were present inside the silica matrix rather than on its surface or at the glass-air interface. Here, direct observation of one-

dimensional (1D) molecular motions by wide-field video microscopy affords the evidence necessary to conclude the dye molecules are in fact confined inside the silica mesopores.

Figure 6.1 shows representative wide-field fluorescence videos obtained from the surfactant-templated mesoporous silica films doped with C₄OPDI, TAPDI²⁺, and PDISO₃²⁻. The pairs of images presented depict the video data obtained for the two orthogonal polarization states. Each image depicts a compilation of the signals obtained across the entire 200 frame length of each video and was obtained by plotting the maximum signal at each pixel in a single image. These videos show extensive evidence of 1D dye motion for all three dyes. The results unequivocally demonstrate that the dye molecules are entrapped within and diffusing along the long axes of the surfactant-filled silica mesopores. Similar results have been reported in a number of recent publications on related materials.^{27,28}

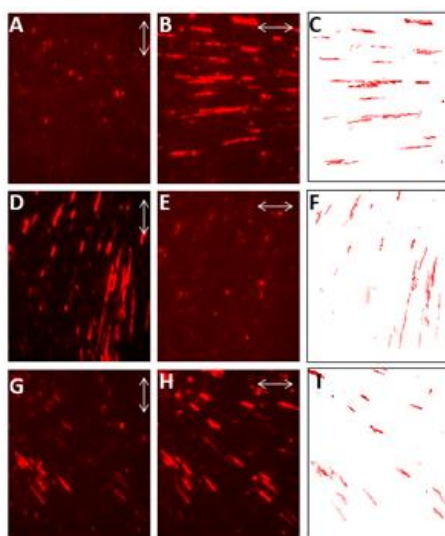


Figure 6.1 Z-projection images of fluorescence acquired simultaneously in two orthogonal polarizations for (A, B) C₄OPDI (D, E) TAPDI²⁺ (G, H) PDISO₃²⁻. These images show the predominance of 1D diffusive motion observed for all Dye molecules and the strong polarization of their emission parallel to the direction of motion. Double-ended arrows designate the detected polarizations. (C, F, I) Plot the trajectories obtained from each video.

The results in Figure 6.1 demonstrate that some dye molecules remain at fixed locations throughout each video while others appear to move in two dimensions (2D). More quantitative assessment of molecular motion was accomplished by tracking the fluorescent spots associated with the single molecules across multiple video frames. Tracking software written in-house was used for this purpose. This software was designed to locate the individual fluorescent spots in individual frames and to fit each a two-dimensional Gaussian function. The individual spot locations were then linked into trajectories spanning multiple video frames.⁴⁰ These trajectories depict the translational motions (or lack thereof) for each molecule. Trajectories obtained from the video data shown in Figure 6.1 are also plotted in the figure (panels C, F, and I).

These trajectory data were subsequently used to assess molecular mobility and the dimensionality of molecular motion. At the most fundamental level, molecules were first assigned to immobile or mobile populations. Assignment of molecular mobility was accomplished by comparing the average localization variance data, σ^2 , (i.e. the error in locating each spot in each video frame)^{60,135} determined as described below, to the mean square displacement (MSD) for each molecule. Trajectories yielding MSD values equal to or smaller than their average localization precision were assigned to the immobile population while the rest were classified as mobile molecules,^{60,135} as illustrated by Eqs. 6.1 and 6.2:

$$\mathbf{Immobile} \quad \text{MSD} \leq 4.6\sigma^2 \quad (\text{Eq. 6.1})$$

$$\mathbf{Mobile} \quad \text{MSD} > 4.6\sigma^2 \quad (\text{Eq. 6.2})$$

Here, the factor of 4.6 ensures that the MSD value is greater than 99% of the squared deviations from the mean position. The localization variance was obtained from the fluorescence signal levels and detector background, as defined by Eq. 6.3.⁶¹

$$\langle(\Delta x)^2\rangle = \frac{s^2 + a^2/12}{N} + \frac{8\pi s^4 b^2}{a^2 N^2} \quad (\text{Eq.6.3})$$

Where, s , a , and N represent the standard deviation of the point-spread function (i.e., the Gaussian width of each fluorescent spot), the pixel size, and the total photon counts under the Gaussian spot. The term b^2 represents the background counts. The latter was estimated from the square of the signal standard deviation in image regions free of fluorescent spots.⁶¹

The single-frame mean square displacement values for each trajectory were obtained by fitting the first four points in each MSD plot to a straight line. The slope of this line yields the single-frame MSD directly. It is this MSD value that was compared to the localization variance determined as described above. In these measurements, the mean MSD exhibited by each molecule was calculated and plotted as a function of time.⁴⁵ These data were fit to a straight line out to a five-frame delay, with the slope of the line giving the MSD value. Figure 6.2 shows representative plots. The diffusion coefficient was then obtained for each molecule from its MSD value.

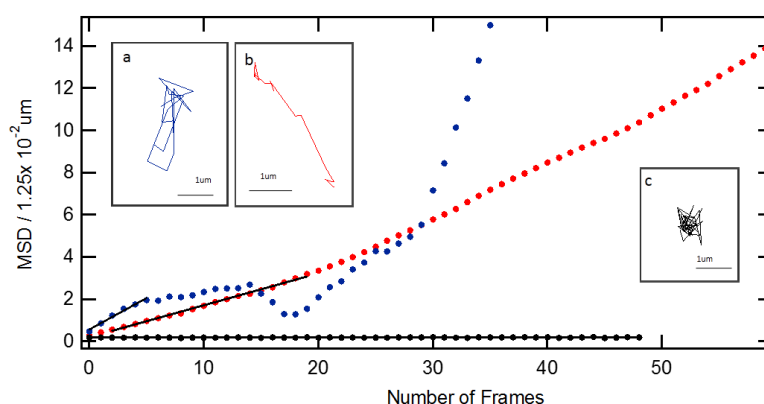


Figure 6.2 Representative single-molecule trajectories and MSD plots for (a) 2D molecule in blue circle (b) 1D molecule in red circles (c) Immobile molecule in triangles.

Once the mobile population was determined, the trajectories were further analyzed to assign the dimensionality of their motions. Specifically, the trajectories were separated into populations exhibiting 1D and 2D motions. Classification of the individual trajectories in this regard was

accomplished by first analyzing the trajectory data by orthogonal regression methods. Orthogonal regression provides the “best fit” (x,y) positions of the fluorescence spots in each trajectory, the orientation of the 1D trajectory segments in the film plane, and estimates of the errors in these parameters.³⁸ Figure 6.3B depicts a representative 1D trajectory and its best-fitted line, showing the in-plane orientation of the trajectory. Also shown are designations for additional parameters obtained, including the motional variance, σ_R^2 (related to the mean-square displacement along the trajectory) and the positional variations, and σ_s^2 (the error in measured the position of the molecule).³⁸ The positional variance, σ_s^2 was then compared to the motional variance, σ_R^2 . Trajectories having a motional variance significantly larger than their positional variance were assigned as 1D, while the remainder were assigned to the 2D population, as defined by Eqs. 6. 4 and 6.5.

$$1D \quad \sigma_R^2 > 4.6\sigma_s^2 \quad (\text{Eq. 6.4})$$

$$2D \quad \sigma_R^2 < 4.6\sigma_s^2 \quad (\text{Eq. 6.5})$$

This analysis was applied to all trajectories longer than 7 frames in each video. The trajectories were then color-coded for easy visualization of their dimensionality assignment. Figure 6.3(A) provides a representative color-coded trajectory plot.

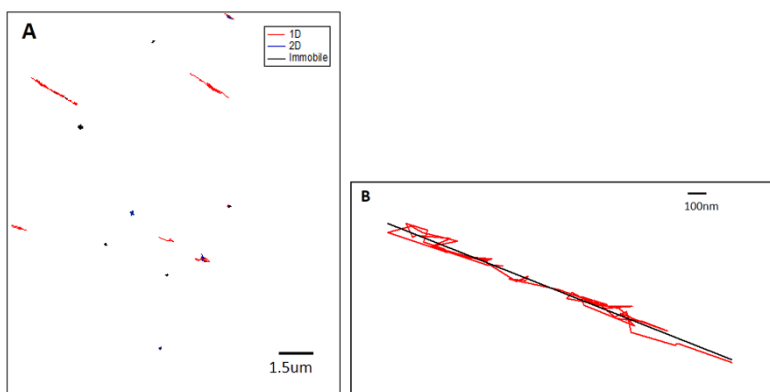


Figure 6.3 (A) Representative Trajectory plot showing immobile, 1D diffusion, 2D diffusion molecules (Immobile-Black,1D-Red,2D-Blue) (B) Representative single-molecule trajectory showing one molecule moving at $\phi \sim 30^\circ$.

6.3.1 Populations of Mobile and Immobile Molecules

The mobility and dimensionality analysis were carried out for ~ 9-10 videos for each of the four dyes. Once the dimensionality of each trajectory had been determined, the results were compiled to obtain mean relative populations of immobile, 1D diffusing, and 2D diffusing molecules.

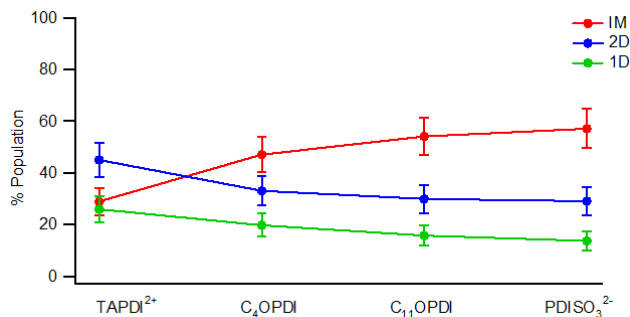


Figure 6.4 Mean relative population of immobile (Red), 1D diffusing (Green) and 2D diffusing (Blue) molecules. The error bars depict the 95% confidence intervals for each value.

The mean relative populations are represented in Figure 6.4. According to these data, anionic PDISO₃²⁻ has the largest immobile fraction (57%) and the smallest mobile fraction (2D: 29%, 1D:14%). In contrast, cationic TAPDI²⁺ produced the smallest immobile population (29%) and the largest mobile population (2D: 45 %, 1D: 26%). The structures of these two molecules are shown in Figure 4.4. Their different behaviors are consistent with differences in their electrostatic interactions with the nanostructured pore-filling medium. According to the studies reported in chapter 5, PDI molecules may be expected to locate near the center of the surfactant-silica nanochannels. Assuming the molecules employed in this chapter also locate near the center of the nanochannel, we can obtain more details about the surface charge of the nanochannels. The present results imply that the relevant electrostatic interactions favor attraction between the negatively charged molecules and the cationic surfactant headgroups near the pore surface, causing a larger

population of these molecules to be immobile. In contrast, the cations are likely repelled from the positively charged micellar surface, causing them to move towards the center of each pore, making them more mobile. These interpretations also suggest that the positive charges of the surfactant headgroups are more important than the anionic sites on the silica pore walls in governing translational diffusion of the dyes. The molecule diffusion data indicate that molecules are much closer to the surfactant micellar surface than to the silica surface. Therefore, probe molecules dynamic mechanisms are strongly affected by the surfactant micelles surface than the silica surface.

The data in Figure 6.4 also shows that the behavior of the uncharged dyes fall between that of the cation and anion. The population data indicate that the C₄OPDI molecules are commonly more mobile than C₁₁OPDI. Likewise, more 1D diffusion is also observed for C₄OPDI than for C₁₁OPDI. Much shorter C₄OPDI molecules (~ 2.2 nm in length) can yield greater mobility (2D: 33%, 1D: 20%) compared to the longer C₁₁OPDI molecules (~ 2.8 nm in length), which yield lower mobility (2D: 30 %, 1D:16%). The early studies show that the molecules are confined into the hydrophobic micellar core region in the pore.¹⁴⁶ Having a long hydrocarbon chain in the C₁₁OPDI molecule favors the longer molecules to move to the hydrophobic micellar region than it is for the shorter C₄OPDI molecule. But longer C₁₁OPDI molecules exhibit a higher immobile population. This restricted mobility of molecules can cause by the presence of small hydrophilic environments within the micellar core region such as solvent islands (e.g., Water) or spherical micelles. Since a higher amount of C₁₁OPDI molecules are expected to be in the micelle core region than C₄OPDI molecules, C₁₁OPDI molecules can be more affected by such small hydrophilic environments than C₄OPDI molecules. Therefore, C₁₁OPDI molecules may exhibit higher immobile population than C₄OPDI molecules.

Looking into the detailed population data, the 1D population is higher for positively charged molecules compared to the other molecules. This may be the result of restricted mobility due to

electrostatic repulsion caused by the cylindrical surface formed by the charged surfactant headgroups surrounding the micelles. In previous studies of PDISO_3^{2-} dye diffusion in the CTAB-silica system, performed using fluorescence correlation spectroscopy (FCS), the PDISO_3^{2-} molecules were found to be immobile under all conditions explored.¹⁷³ The immobility of PDISO_3^{2-} in the CTAB-containing materials was concluded to arise from strong ionic interactions with the surfactant. Here, we have obtained more detailed single molecule level information indicating that while many (57%) of the PDISO_3^{2-} molecules were immobile, some of the molecules still diffused in 1D and 2D.

6.3.2 Rate of Molecular Motion

The diffusion coefficients were obtained for each molecule from its MSD value, using $D = \text{MSD}/(2nt)$, where n is the dimensionality of diffusion and t is the video frame time (0.093 s). Figure 6.5 depicts histograms of the D values obtained from 1D trajectories of all four PDI molecules. The most common values, reflected by the peak of each in homogeneous distribution, were measured to be $0.042 \text{ um}^2\text{s}^{-1}$, $0.020 \text{ um}^2\text{s}^{-1}$, $0.006 \text{ um}^2\text{s}^{-1}$, and $0.038 \text{ um}^2\text{s}^{-1}$ for C_4OPDI , C_{11}OPDI , TAPDI^{2+} and PDISO_3^{2-} respectively. The mean D value obtained by averaging all results from the 1D and 2D diffusing populations are shown in Table 6.1 with errors at 95% confidence level.

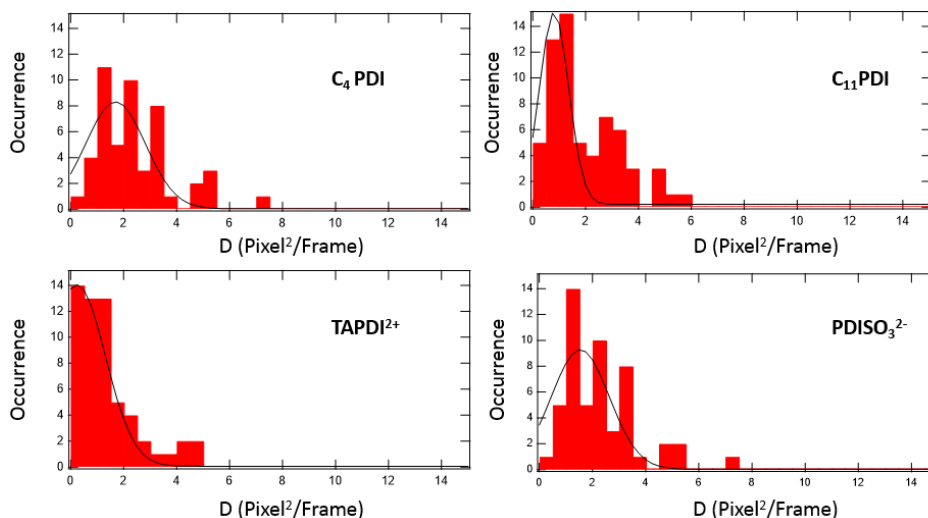


Figure 6.5 Histograms showing the distribution of measured D values for 1D diffusing molecules. The solid lines depict the Gaussian fits to each histogram used to determine the peak of the distribution.

AVRG Diffusion Coefficient	TAPDI ²⁺ molecules $\mu\text{m}^2\text{s}^{-1}$	C ₄ PDI molecules $\mu\text{m}^2\text{s}^{-1}$	C ₁₁ PDI molecules $\mu\text{m}^2\text{s}^{-1}$	PDISO ₃ ²⁻ molecules $\mu\text{m}^2\text{s}^{-1}$
1D Trajectories	0.034± 0.029	0.060± 0.035	0.049± 0.033	0.056± 0.050
2D Trajectories	0.010± 0.009	0.008± 0.005	0.006± 0.005	0.010± 0.010

Table 6.1. Calculated mean 1D and 2D diffusion coefficients for all four dyes.

The calculated mean D values for 1D trajectories to be $0.060 \mu\text{m}^2\text{s}^{-1}$, $0.049 \mu\text{m}^2\text{s}^{-1}$, $0.034 \mu\text{m}^2\text{s}^{-1}$, and $0.056 \mu\text{m}^2\text{s}^{-1}$ for C₄OPDI, C₁₁OPDI, TAPDI²⁺, and PDISO₃²⁻ respectively. Similarly, small D values have also been measured for 1D diffusing neutral PDI dyes in related mesoporous silica films in early studies.^{27,38} The differences between the average and most common D values reported above result from “tailing” of the distributions to higher D values (see Figure 6.5), which biases the average results. The observation of these higher D values reflects nanoscale heterogeneity. The variations in pore filling medium which is CTAB surfactant micelles can be

one of the main reasons creating the heterogeneity within the nanopores, such as the presence of spherical micelles. Also, the different compositions of the solvent system (Water: EtOH ratio) can create possible heterogeneity along the pore structure. Water “pockets” can be generated between micelle structures causing nanoscale heterogeneity and different diffusion rates. Higher diffusion coefficient could also result from molecules “jumping” from one open pore to another. The molecules “jumping” may occur due to the presence of defects (i.e., openings) in the pore walls and molecules capability to readily access and pass through them.

The mean D values for 2D trajectories were found to be $0.008 \text{ um}^2\text{s}^{-1}$, $0.006 \text{ um}^2\text{s}^{-1}$, $0.010 \text{ um}^2\text{s}^{-1}$ and $0.010 \text{ um}^2\text{s}^{-1}$ for C₄OPDI, C₁₁OPDI, TAPDI²⁺, and PDISO₃²⁻ respectively. In all four dye molecules, 2D diffusing molecules gave significantly smaller mean D values than their 1D trajectories. Moreover, the observed D values for 2D trajectories are similar to the D values obtained for the immobile population. Indeed, it is likely that some immobile molecules are also included in the 2D mobile population. This could arise from situations in which the localization precision is degraded by low signal or excess noise, making the molecules appear as though they are moving in 2D. The similarity in D values also suggests that adsorption and desorption may be taking place throughout the trajectories. As discussed earlier, negatively charged molecules can adsorb to the positively charge micellar surface as well as the presence of spherical micelles or solution islands can result in possible molecules adsorptions. The studies of Fangmao Ye¹⁷³ discuss the possibility of heterogeneity and surface absorption of dye molecules employing neutral and negatively charges dyes in similar surfactant-silica systems.

6.3.3 Molecule Confinment

As reported in earlier studies of PDI dyes,^{27,28} all four PDI dyes in the present work also exhibit subtle fluorescence depolarization that may be attributed to a confined “wobbling”^{31,52} of the molecule about its average orientation as it diffuses along the pore. The level of orientational confinement exhibited by PDI dyes was quantified by determining the mean “wobbling angle” for

each molecule, using methods defined in detail in the original reports describing SMEP measurements,^{27,28} and as discussed in Chapter 5. Briefly, this analysis requires fitting each 1D trajectory to a line by orthogonal regression methods,³⁸ to obtain the average in-plane orientation, ϕ , of each pore, and hence the average in-plane orientation of each molecule. The SMEP data also provide quantitative frame-by-frame values for the fluorescence polarization, FP. These data are averaged along the trajectory length, and the mean wobbling angle, $\langle\theta\rangle$, is then determined via Eq 6.6.⁵³

$$\langle\cos^2\theta\rangle = \frac{\cos(2\phi) + FP(2a^2 + 1)}{3\cos(2\phi) + FP(2a^2 - 1)} \quad (\text{Eq. 6.6})$$

Here, a^2 is a constant (0.44) defined by the numerical aperture of the microscope objective.²⁷ Figure 6.6 plots a histogram showing the mean wobbling angles obtained from the 1D trajectories produced by the four dye molecules, using $\cos^2\langle\theta\rangle \approx \langle\cos^2\theta\rangle$.

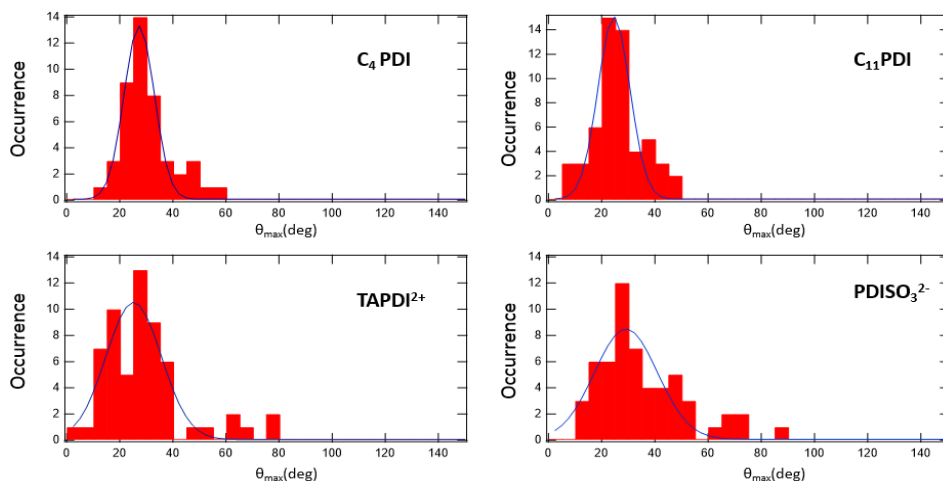


Figure 6.6 Distribution of wobbling angles for C₄OPDI , C₁₁OPDI, TAPDI²⁺ , and PDISO₃²⁻ dyes exhibiting 1D motion. The solid lines depict Gaussian fits to the distributions.

These data reveal that the wobbling motions exhibited by all PDI molecules are tightly confined. The average value for the mean (and maximum, θ_{\max}) wobbling angles in the case of TAPDI²⁺ cation was $\sim 24^\circ$ (and 29°), while the PDISO₃²⁻ anion exhibited wobbling angles of 27° (and 34°). The smaller wobbling angle observed for the cation can be explained by electrostatic repulsion from the positively charged micellar surface, which may confine its orientational motions. In contrast, the electrostatic attraction that occurs between the anionic PDI molecules and the cationic headgroups of the surfactant micelles may cause the higher wobbling angle observed in that case. The wobbling angles and confinement of neutral PDI molecules are defined by steric interactions that scale with their molecule sizes. The shorter C₄OPDI molecule, therefore, exhibited a larger wobbling angle of $\sim 27^\circ$ (and 30°) while the longer C₁₁OPDI molecule exhibit a smaller wobbling angle of $\sim 25^\circ$ (and 26°) due to its greater level of confinement. It is concluded that the SMT and SMEP data provide quantitative measurements of the confined PDI wobbling motions within the surfactant filled silica mesopores. The charge dependent wobbling observed here provides further evidence for the claim that the molecules located inside the nanochannels, and for the hypothesis that the positive charges on the outer micelle surfaces play an important role in governing molecular confinement and motions within the surfactant-filled pores.

6.3.4 Mechanistic Insights into Single-Molecule Diffusion

The SMT data from the 1D molecular population was further analyzed to better understand the mechanisms of diffusion in the silica nanopores. For example, the molecules could move by a Fickian-like mechanism, which is most often used to describe diffusion in bulk solution. However, with the tight confinement of the molecules to nanometer-sized pores, it is likely that interactions with the pore surfaces also plays an important role. For example, diffusion along the surface may be interrupted by adsorption events in which the molecules are briefly immobilized on the surface

but are later released and begin to move again. Such a process is inherently non-Fickian and is known in the literature as desorption-mediated diffusion.¹⁷⁴

Indeed, in most SMT studies of molecule diffusion in surfactant filled mesoporous silica, it has been tacitly assumed that diffusion occurs by a Fickian mechanism, with the MSD increasing linearly in time.⁴¹ Evidence for the involvement of both Fickian and non-Fickian (i.e., anomalous diffusion) mechanisms was obtained in the present studies by further analysis of the SMT data. Specifically, the mechanism of diffusion was further explored by calculating and plotting the single-frame step-size distribution for each single molecule trajectory as shown in Figure 6.7. Fickian diffusion is expected to produce a step size distribution of Rayleigh-like character.¹⁵⁷ Eq. 6.7 shows the population distribution expected for Fickian diffusion.

$$P(r, t) = A \left(\frac{r}{2Dt} \right) \exp \left(-\frac{1}{2} \left(\frac{r^2}{2Dt} \right) \right) \quad \text{Eq. 6.7}$$

Here, A is a fitting constant, t is the measurement time (the frame time), and r is the step size.

In contrast, anomalous diffusion occurring by a desorption-mediated mechanism produces a population distribution characterized by a Lorentz function (in two dimensions).¹⁷⁵⁻¹⁷⁷

$$P(r, t) = \frac{Actr}{(r^2 + (ct)^2)^{3/2}} \quad \text{Eq. 6.8}$$

Here, $c = (D/\tau)1/2$, in which τ is the “retention time” of molecules on the surface, and A is again a fitting constant.

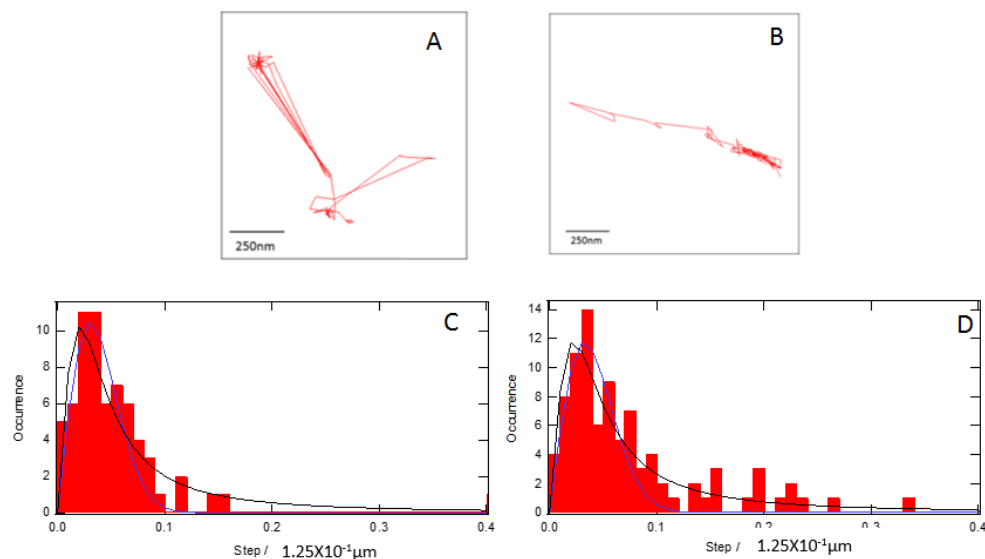


Figure 6.7 Representative single-molecule trajectories (A) and (B) and stepsize distributions obtained from these trajectories (C) and (D) respectively. Blue lines depict fits to Eq 6.7, and black line depicts to Eq. 6.8. Results are attributed to Fickian diffusion in (C) and anomalous diffusion in (D).

As shown in Figure 6.7 (C, D) each step size distribution was fitted to a Rayleigh-like distribution and a Lorentz distribution. The non-Fickian diffusion mechanism is expected to exhibit a characteristic tail to large step sizes that are absent for Fickian diffusion.¹⁷⁵⁻¹⁷⁷ Next, the best-fitted distribution was determined for each step size distribution. As shown in Figure 6.7, the results shown are attributed to Fickian diffusion in (C) and anomalous diffusion in (D).

Importantly, evidence for the participation of both Fickian and anomalous diffusion mechanisms was observed for all four PDI dyes. Unfortunately, it is not possible to unambiguously assign the mode of diffusion for most trajectories. Nevertheless, these data provide evidence that adsorption and desorption of the dye molecules very likely plays a role in governing their mobility.

6. 4 Conclusion

The present studies demonstrate that nanostructuring of the solvent and surfactant medium filling the cylindrical pores of spin-coated mesoporous silica films plays an important role in governing the diffusive translational and orientational motions of incorporated reagents or analytes. The charged and neutral PDI dyes and their electrostatic interactions with the micellar surface were used to understand and to collect more evidence on molecules location within the nanopore structure as well as evidence of nanoscale heterogeneity. The mobility population data and the diffusion coefficient values collected by the SMT method provide more evidence of the molecules dynamics such as electrostatic interaction and adsorption/desorptions. Also, SMEP measurements shown that all four dyes regardless of their size or charge exhibit tight confined within CTAB-filled mesopores. It was concluded that the surfactant micellar interface exhibits a positive charge due to the CTAB head group. Further, the micellar surface highly screens the negatively charged silica surface. The mobility data and mechanisms of mobility suggest that possible irregularity in the micellar structures such as the presence of spherical micelles, and possible solvent(water) islands may lead to substantial heterogeneity in the materials. This could be one of the primary reasons behind nanoscale heterogeneity. Also, the SMT results lead to the conclusion that the molecules move by a combination of Fickian and anomalous diffusion mechanisms within the solvent-filled surfactant-templated silica mesopores.

Chapter 7 - Probing the Local Dielectric Constant of Plasmid DNA in Solution and Adsorbed on Chemically Graded Aminosilane Surfaces

Reproduced with permission from American Chemical Society.

Published as Zi Li, Ruwandi Kumarasinghe, Maryanne M. Collinson and Daniel A. Higgins.

J. Phys. Chem. B, 2018, 22, 2307-2313.

Contributions of Authors

Zi Li was responsible for the DNA solution and chemical gradient preparations, AFM imaging of the DNA, and optical experiments. I helped calibrate the Nile red response to the dielectric constant of its microenvironment. Also, I helped with the alignment of the wide-field microscope and with spectroscopic imaging experiments. Zi Li and I worked together on the SMT data analysis and interpretation. Zi Li was responsible for analysis and interpretation of data from the surface gradients. Dr. Higgins guided the research patiently. He and Dr. Collinson provided indispensable help in preparing this work for publication.

7.1 Introduction

The dielectric constant, ϵ , in different microenvironments within double stranded DNA (dsDNA) is an important parameter that affects its interactions with other polyelectrolytes (e.g., proteins), with small organic and inorganic molecules (e.g., drugs), and with surfaces. Its value has been widely explored in both the computational¹⁹⁵⁻¹⁹⁷ and experimental literature.^{198,199} The values reported reflect a high degree of microheterogeneity. For example, the major groove of dsDNA is known to be very polar, giving $\epsilon \sim 55$.¹⁹⁹ The major groove is where proteins usually bind. Its high dielectric constant derives in part from the presence of water in the groove. The minor groove is substantially less polar, yielding $\epsilon \sim 20$.¹⁹⁸ Polar small molecules and some

proteins bind along the minor groove. Its smaller dielectric constant reflects closer proximity to the sugars and nucleobases and reduced contributions from water. Regions comprising the stacked nucleobases within dsDNA are expected to be the least polar of all. Nonpolar small molecules intercalate into these regions, usually inserting between the nucleobases. Computational studies give values of $\epsilon < 5$ for these microenvironments.¹⁹⁵⁻¹⁹⁷ Unfortunately, it appears that no direct measurements of the dielectric constant for the least polar environments in DNA have been reported to date. In depth knowledge of the dielectric properties of these environments is of importance to a full understanding of DNA polarity. Along with its dependence on location and composition, ϵ is also expected to vary with DNA conformation. It is well known that the flexibility of DNA increases (i.e., its persistence length decreases) with an increase in solution ionic strength.^{200,201} Increased flexibility of DNA is attributable to reduced repulsion between the negatively charged phosphate groups along its backbone. Condensation of DNA at high ionic strengths^{186,195} is likely to produce a decrease in the local dielectric constant as the organic regions of the DNA become more compact and the associated dipoles become less mobile. Similar effects may also arise when DNA is dissolved in a poor solvent,²²²⁻²⁰⁴ or upon binding to synthetic polycations^{186,195} or proteins, such as occurs in the cell nucleus. Few, if any, previous studies have looked at the impacts of these phenomena on the dielectric constant of the least polar microenvironments within DNA.

Probing the polarity of these microenvironments requires the use of a dye that intercalates into DNA. The dye must also be sufficiently solvatochromic to afford a good measure of the local dielectric constant. Nile Red (NR) is an ideal candidate for such studies because it is highly fluorescent, very sensitive to local polarity,^{32,206} and sufficiently hydrophobic to function as a DNA intercalator.¹⁹⁰ NR has been employed previously to examine the dielectric properties of liquids,³² organic polymers,^{34,42} proteins,²⁰⁶ zeolites,⁴⁹ nanotubes,¹⁸⁹ mesoporous silica,¹⁴⁶ and organically modified silica.⁴³ It is nonfluorescent in aqueous environments and highly fluorescent

in nonpolar environments,⁴⁹ making it uniquely suited to studies of DNA polarity in aqueous solution.

For this report, the local dielectric constant within the least polar microenvironments in plasmid DNA were measured by fluorescence microspectroscopic methods. The dielectric constant of the plasmid was measured in both its supercoiled and relaxed forms in aqueous buffer solution, as a function of buffer concentration, and for DNA molecules adsorbed along aminosilane-derived chemical gradients. The latter serve as models for DNA bound to different proteins.⁴⁹ Chemically graded surfaces^{183,184,191,193} were employed because they allow for timeefficient investigations of how the density of amine groups impacts the dielectric properties of the DNA.

7.2 Experimental Section

7.2.1 Chemicals and Materials

Relaxed and supercoiled plasmid DNA (5386 base pairs) were purchased from New England Biolabs. These were obtained as 10 mM Tris-HCl solutions (pH 8.0 at 25 °C) with 1 mM EDTA. NR, phosphate buffered saline (PBS), tetramethylorthosilicate (TMOS, 98%) and (3-aminopropyl)trimethoxysilane (APTOS, 97%) were all purchased from Sigma-Aldrich and all were used as received. NR was dissolved in HPLC-grade ethanol to form a 200 nM stock solution. All buffers and DNA solutions were prepared using pure water of 18 MΩ·cm resistivity. Glass coverslips were obtained from Fisher Scientific (FisherFinest Premium, 25 × 25 mm). Silicon wafers were obtained from University Wafer and were cut into 25 mm x 25 mm pieces prior to use. Both types of substrate were thoroughly cleaned prior to use, as defined below.

7.2.2 Sample Preparation

DNA solutions. DNA solutions were prepared in 0.01 mM, 0.1 mM, 1 mM, 2.5 mM, 5 mM, and 10 mM PBS. These solutions were obtained by diluting 1×PBS with deionized water. 1×PBS (Sigma-Aldrich) contains 10 mM phosphate, 138 mM NaCl, and 2.7 mM KCl. Stock DNA solution was prepared by diluting 3.5 μL of 1000 $\mu\text{g}/\text{mL}$ relaxed or supercoiled plasmid DNA to 1 mL with 1×PBS. The concentration of the stock solution was 1 nM. The 40 pM relaxed and supercoiled plasmid DNA solutions used for optical measurements were prepared by mixing 40 μL of 1 nM stock of the selected plasmid and 72 μL of 200 nM stock NR solution with 890 μL of one of the PBS solutions. The NR-stained DNA solutions were stored in a refrigerator overnight prior to use. The final staining ratio was ~ 1 NR per 15 DNA base pairs.

TMOS sol. The coverslips employed as substrates were coated with a silica base layer prior to gradient deposition. The base layer served to enhance aminosilane adhesion. The silica base layers were derived from TMOS sols. Preparation of the TMOS sols involved mixing TMOS, ethanol (200 proof), and 0.1 M hydrochloric acid in a volume ratio of 1:99.6:5.4. The mixture was subsequently stirred for 1 h and then stored in a desiccator for 23 h prior to use.

Substrate pretreatment. Both glass coverslips and silicon wafers were employed as substrates and were cleaned by first rinsing with DI water and then drying under a stream of nitrogen gas. They were subsequently cleaned for 5 min in an air plasma. The TMOS base layer was deposited by spin coating (5000 rpm, 30 s) a 150 μL aliquot of the TMOS sol onto the substrate surface. The base-layer-coated substrates were stored in a desiccator overnight. They were subsequently treated in an air plasma for 2 min immediately prior to use. The latter step ensured that a sufficient density of silanol groups on the base-layer surface was obtained for gradient deposition.

Amine gradient deposition. Vapor phase deposition (VPD) was used for preparation of the aminosilane gradients.¹⁸⁵ While VPD methods are often employed directly to obtain gradients based on the natural vapor diffusion profile over a surface, a simple cell formed over the substrate was employed here instead.¹⁸² This cell was used to ensure the gradient was formed at a reproducible, predefined position in replicate depositions. For this purpose, two 1 mm-thick PDMS spacers were attached parallel to each other and parallel to the edges of the substrate. A clean glass coverslip was placed on top of the spacers to form a 1 mm gap between the substrate and coverslip. The coverslip only covered one half of the substrate surface, ending at a distance of 8 mm from its edge.

The VPD process was performed in a Plexiglas chamber to eliminate any air currents and to allow for control over the ambient humidity during gradient deposition. The deposition chamber was constructed in house and was shown in an earlier publication.¹⁸² Just prior to initiating VPD, the precursor reservoir and TMOS-coated substrate were placed on a horizontal platform inside the deposition chamber. The separation between the reservoir and substrate edges was 4 mm. The precursor reservoir was filled with a mixture of 25 μL of APTMOS and 0.2 g paraffin oil. This mixture was added through an inlet in the top of Plexiglas chamber. Each substrate was exposed to aminosilane vapor for 8 min to form the APTMOS gradient.

7.2.3 Gradient Characterization

Water contact angle. Sessile drop water contact angle measurements were used to verify that APTMOS gradients had been obtained. These measurements were made using a home-built apparatus. It includes a CCD camera with an attached zoom lens (Navitar), sample stage, and a light source. Droplet images were acquired on the CCD camera and were analyzed using a plugin available for the freely available ImageJ software package.¹⁹² For these measurements, 1 μL droplets of high purity (18 $\text{M}\Omega\cdot\text{cm}$) water were placed at \sim 3-6 mm intervals along the gradients

using a microliter syringe. Three replicate measurements were made at ~ 3 mm spacings across each gradient. All measurements were made under ambient laboratory conditions.

Film thickness. Spectroscopic ellipsometry was used to measure the thicknesses of both the TMOS-derived base layers and the aminosilane gradients. A commercial instrument (α -SE, J. A. Woollam) was used for this purpose and all measurements were made under a dry ($15 \pm 1\%$ RH) nitrogen atmosphere. To achieve enhanced sensitivity, all measurements were performed on base layers and gradients deposited on silicon substrates. Prior to gradient deposition, the base-layer thickness was first measured at a series of points 1 mm apart along the substrate and at three positions across the substrate, at 3 mm spacings. After gradient deposition, the full film thickness (gradient plus base layer) was measured in the same manner. The gradient thickness was determined by subtracting the base-layer thickness from the total film thickness.

7.2.4 AFM Imaging of DNA

Atomic force microscopy (AFM) images of supercoiled and relaxed plasmid DNA were collected using a Digital Instruments Multimode AFM with Nanoscope IIIa electronics. Tapping mode was employed to avoid damaging the features of the surface-adsorbed DNA molecules. Conical AFM tips (nanoscience Instruments, Phoenix, AZ) were used for imaging in air. The scan rate was 0.5 Hz. To obtain better images, freshly cleaved mica was used and aminosilane was deposited on it in the same manner as on TMOS coated glass coverslips. DNA solutions were prepared in 1 mM Tris-HCl buffer (pH ~ 7.1). MgCl_2 was added to the DNA solution to give a final concentration of 1 mM. The concentration of DNA was 1 $\mu\text{g}/\text{mL}$ for both supercoiled and relaxed plasmid. DNA solutions were shaken for 1 h using a vortex mixer (Fisher Scientific) prior to deposition. During DNA deposition, a 50 μL aliquot of DNA solution was placed onto the

APTMOs gradient modified mica and incubated for 10 min. Afterwards, the samples were rinsed with DI water and blown dry with nitrogen.

7.2.5 Single Molecule Tracking

All optical imaging experiments were performed on aminosilane gradients prepared on glass coverslips. Each was immersed in one of the DNA/PBS solutions described above during imaging. For this purpose, a cell was constructed to hold the DNA solution. This cell comprised a 2 cm x 1 cm x 0.5 cm polydimethylsiloxane (PDMS) monolith. The PDMS cell was attached to the glass coverslip using uncured PDMS. Once cured, the latter helped avoid leakage of the solution from the cell. All samples were imaged on a wide-field epi-fluorescence microscope. The microscope employed has been described previously, in detail.⁴¹ In each experiment, the PDMS cell and substrate were first mounted atop the microscope. A ~ 350 μ L volume of NR-doped DNA solution was then added to the cell. Imaging of the NR-doped DNA was accomplished by exciting NR fluorescence with 514 nm laser light. Prior to illumination of the sample, the excitation light was first passed through a spinning optical diffuser, reflected from a dichroic beam splitter (Chroma 555 DCLP), and then focused into the back aperture of an oil immersion objective (1.49 numerical aperture, Nikon APO TIRF, 100 \times). Fluorescence emitted by the dye was collected in reflection, using the same objective. It was subsequently directed back through the dichroic beam splitter and through a 570 nm colored glass long-pass filter (Schott Glass). The fluorescence was then directed into an image splitter (Cairn Research OptoSplit II) incorporating a second dichroic mirror (Chroma 605 DCLP) and two bandpass filters. The image splitter divided the fluorescence into two image channels centered at ~ 580 and ~ 625 nm, respectively, each having a ~ 40 nm passband. Fluorescence in these image channels was detected simultaneously using an electronmultiplying CCD camera (Andor iXon DU-897). Fluorescence videos depicting DNA motion in solution and molecules adsorbed to the gradient surface were acquired as movies 100–500 frames in length.

7.2.6 Calibration of Nile Red Response

Measurement of ϵ for microenvironments within DNA requires the careful calibration of the NR response. Calibration of the response was accomplished by dissolving NR in a series of bulk ethanol/hexane mixtures. These solutions were used to fill a specially designed cell that was mounted atop the microscope. The background-subtracted average signals in the 580 and 625 nm image channels were determined from the collected fluorescence videos of each solution. The emission ratio, E , for each solution was then calculated, as defined in eq.7.1. Figure 7.1 plots the E values obtained from the solution mixtures as a function of their CM factors.

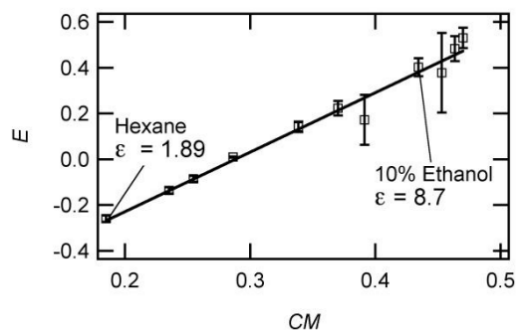


Figure 7.1 Calibration of the NR spectroscopic response to environments having different dielectric constants. The plot shows the NR emission ratio E in bulk solution for a series of hexane-ethanol mixtures. The polarity of each solution is defined by its Clausius-Mossotti (CM) factor $(\epsilon-1)/(2\epsilon+1)$. From the left, the solution compositions are 0, 2, 3, 5, 10, 15, 20, 40, 60, 80 and 100% ethanol. The NR concentration was 2 μM in each case. The solid line shows a linear fit to the data; the slope and intercept were used to interpret the imaging results obtained from NR doped single plasmid DNA molecules. Reprinted with permission from Ref (211). Copyright © 2018, American Chemical Society.

$$E = \frac{I_{625} - I_{580}}{I_{625} + I_{580}} \quad \text{Eq.7.1}$$

7.3 Results and Discussion

7.3.1 Gradient Preparation and Characterization

Amine gradients were prepared on silica base-layer-coated coverslips by a vapor diffusion method that has been described previously.^{182,185} Gradient formation was verified by sessile drop water contact angle (WCA) measurements. Figure 7.2.A shows representative results. An abrupt transition from high WCAs at the high amine end to low values at the low amine (high silica) end is observed at ~ 10 mm. While WCAs could be measured at both ends of the gradient, it was not possible to obtain values in the steepest part of the gradient. In this region, water droplets placed on the surface moved spontaneously towards the low amine end.¹⁸⁵ The WCAs measured at the high and low amine ends are consistent with fully amine-modified and unmodified silica surfaces, respectively.^{187,207}

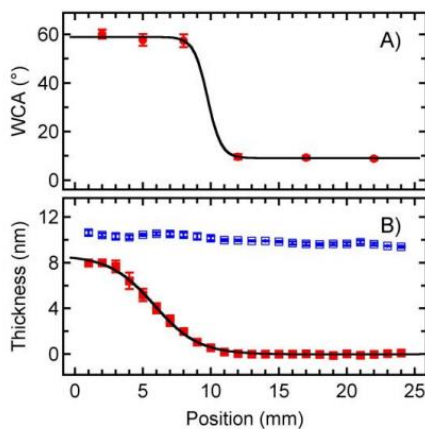


Figure 7.2 A) Sessile drop water contact angle along the amine gradient surface. No contact angle data could be obtained from the steepest region because the water droplets spontaneously moved towards the low amine end of the gradient. B) Spectroscopic ellipsometry data showing the thickness of the TMOS-derived base layer (blue symbols) and the aminosilane gradient (red symbols). Gradient thickness was obtained by subtracting the base layer thickness from the full film thickness. The positions along the X-axis in the two panels are not identical but indicate similar positions to ± 1 mm. The solid lines are fits to

sigmoidal functions and have been added only to better show the trends in the data. Reprinted with permission from Ref (211). Copyright © 2018, American Chemical Society.

The thicknesses of the silica base-layer coating and the amine gradient were determined by spectroscopic ellipsometry. The results are shown in Figure 7.2B. The base layer was nominally 10 nm thick. The gradient thickness was ~ 8 nm at the high amine end, indicating a multilayer aminosilane film had been formed.¹⁹⁰ The amine layer thickness quickly dropped to values near zero by the 11 mm position. The experiments described below focus on positions between 6 and 12 mm along the gradients.

7.3.2 AFM Imaging of Surface-Adsorbed Plasmid DNA

AFM was employed to verify the conformational differences between the relaxed and supercoiled forms of plasmid DNA adsorbed to the amine surface. For this purpose, DNA was adsorbed on aminosilane coated mica substrates by incubating them for a period of 10 min in 1 mM pH ~ 7.1 Tris-HCl buffer containing 1 mM MgCl₂ and 1 μg/mL (286 pM) plasmid DNA. The substrates were subsequently rinsed with DI water and blown dry with nitrogen.

The topographic heights of the DNA molecules were measured to be ~ 1 nm or less, consistent with previous observations of dsDNA.⁹⁴ The primary differences between the two forms of the plasmid are in their conformations, with the supercoiled DNA exhibiting significant superhelical twisting. The use of supercoiled and relaxed plasmid allowed for conclusions to be drawn on the relationship between DNA conformation, as observed by AFM, and the local dielectric constant in the least polar DNA microenvironments (see below).

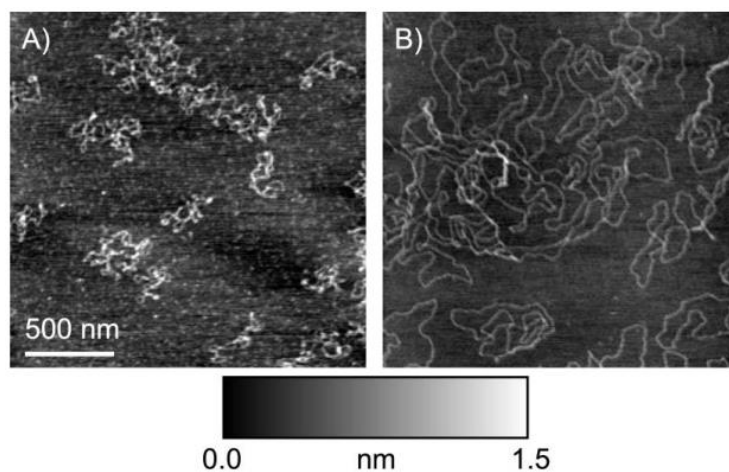


Figure 7.3 AFM images of A) supercoiled and B) relaxed plasmid DNA on APTMOS-coated mica. Plasmid DNA was deposited from 1 mM Tris-HCl solutions also containing 1 mM MgCl₂. Reprinted with permission from Ref (211). Copyright © 2018, American Chemical Society.

7.3.3 Dielectric Constant Measurements for Plasmid DNA in Solution

The dielectric constant within the least polar microenvironments of both solution-phase and surface-bound plasmid DNA was determined by using NR as a spectroscopic probe. It is well known that the fluorescence emission of NR shifts to the red with increasing ϵ .^{32,206} When its emission is recorded simultaneously in two spectral bands (i.e., 580 ± 20 nm and 625 ± 20 nm), the environment-dependent spectral shift of NR emission can be used to quantitatively determine ϵ .^{41,42,146} Here, the emission ratio, E , defined as $E = (I_{625} - I_{580}) / (I_{625} + I_{580})$ was employed, where I_{580} and I_{625} represent the measured fluorescence signal in each of the two spectral bands. As has been shown previously,^{41,146} E scales approximately linearly with the Clausius-Mossotti (CM) factor (Figure 7.1) of the local environment, where $CM = (\epsilon - 1) / (2\epsilon + 1)$. The CM factor comprises the dominant contribution⁴² to the orientation polarizability by the dipoles surrounding NR within the DNA. The results of the solution-phase fluorescence experiments will be described first. Phosphate buffered saline (PBS) solutions (0.01, 0.1, 1.0, 2.5, 5, and 10 mM phosphate

concentrations, pH ~ 7.2 at all but 0.01 mM) containing 40 pM plasmid DNA and 14.4 nM NR were employed. Under these conditions, the level of dye loading in the DNA was ~ 1 NR for every 15 base pairs. The relatively dilute loading of the DNA by the uncharged NR dye is not expected to cause changes in its conformation.¹⁹⁰ Changes to the DNA structure induced by a higher staining ratio could alter the local dielectric properties. A higher staining ratio could also lead to increased intercalation of NR into more polar (less favorable) microenvironments. The small NR concentration precludes such effects and also helps avoid the formation of dye aggregates. Furthermore, NR aggregates have been reported to be non-fluorescent,³⁷ and should make no contribution to the measured signal.

All fluorescence imaging experiments were performed on an inverted wide-field microscope operated in the total internal reflection fluorescence (TIRF) mode. A solution filled cell fabricated from PDMS was employed and was positioned atop the microscope. A plasma-cleaned cover glass having no base layer or gradient coating was used to form the optical window of the cell in solution-phase experiments. The microscope was set to focus on DNA molecules diffusing in solution.¹⁸⁸ Representative two-color fluorescence videos show bright fluorescent spots that move rapidly from frame to frame within the area imaged. NR is known to be non-fluorescent in aqueous solution,⁴⁹ and control experiments performed in the absence of DNA were consistent with this expectation. Therefore, the bright spots observed in the videos are attributable to detection of individual NR-doped plasmid DNA molecules. Each molecule appears twice in the individual frames, once in each of the two channels (580 nm and 625 nm).

Solution-phase E values and the corresponding CM factors were obtained by measuring the background-subtracted signal level for each fluorescent spot. The results from a series of samples prepared at different buffer concentrations are plotted in Figure 7.4 for both supercoiled and relaxed forms of the plasmid DNA. The CM factors all fall between 0.397 and 0.286, consistent with ϵ values ranging from 6.75 to 3.00, respectively. Taken together with theoretical predications

of ϵ in the least polar regions of DNA,¹⁹⁵⁻¹⁹⁷ these results provide conclusive evidence that NR behaves as an intercalator. The values obtained also provide experimental confirmation of the low ϵ values predicted for regions internal to the dsDNA double helix.¹⁹⁵⁻¹⁹⁷

The data shown in Figure 7.4 depict a clear relationship between the CM factor and buffer concentration (proportional to ionic strength at constant pH in PBS buffer, see Experimental Considerations). The CM factor gradually increases as the buffer concentration decreases from 10 mM. It becomes relatively invariant at concentrations < 1 mM, although measurement error becomes significant at such low concentrations. The large error bars at 0.01 mM are attributable to the increased variability in ionic strength caused by reduced buffer capacity and increased variability in pH. The level of error also reflects the relatively weaker fluorescence observed from NR intercalated into DNA at lower buffer concentrations. Weaker NR fluorescence under these conditions is consistent with the observed increase in ϵ . NR is known to be less fluorescent in more polar environments.⁴⁹

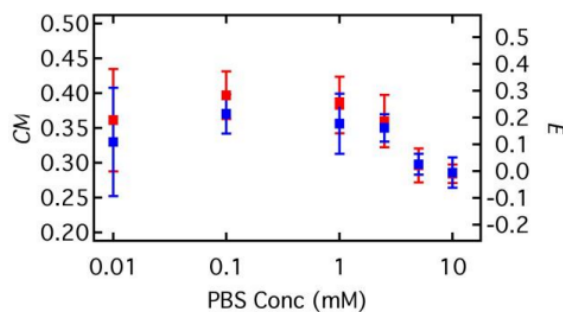


Figure 7.4 Solution phase E values (right axis) and CM factors (left axis) obtained from Nile Red in supercoiled (red symbols) and relaxed (blue symbols) plasmid DNA. The error bars depict the 95% confidence intervals for each value. Reprinted with permission from Ref (211). Copyright © 2018, American Chemical Society.

The decrease in ϵ with increasing buffer concentration correlates well with the known dependence of DNA persistence length on solution ionic strength.^{200,201} Extensive data reported in the literature show that the DNA persistence length is ~ 100 nm for ionic strengths of ~ 1 mM.²⁰¹ As the ionic strength increases, the persistence length decreases to ~ 50 nm.²⁰¹ This correlation suggests there might be a direct link between DNA conformation and local polarity. While it is tempting to conclude that increased bending of the DNA at higher ionic strengths leads to a decrease in ϵ , the computational literature demonstrates that the dielectric constant depends most strongly on the composition and molecular structure within ~ 0.5 nm of the microenvironment being probed.¹⁹⁶ Changes in DNA conformation associated with changes in persistence length are manifested on longer (i.e., tens of nanometers) length scales. Furthermore, comparison of the data from relaxed and supercoiled plasmid reveals no measurable difference in ϵ despite their significant differences in conformation. It is concluded that the observed conformational differences are not the cause of changes in the local polarity. Rather, it is believed that the same factors that lead to increased flexibility of the DNA at higher ionic strengths also lead to changes in the DNA structure on much shorter length scales. These, in turn, cause a decrease in ϵ . Based on these observations, the lower dielectric constant sensed by NR at higher buffer concentrations is attributed to condensation of the DNA due to decreased repulsion between the negatively charged phosphate groups.¹⁹⁷ A contraction of the DNA structure occurs upon condensation, driving water molecules from the structure and also leading to reduced mobility of the dipoles comprising the DNA microenvironment.

7.3.4 Dielectric Constant Measurements for Surface-Adsorbed Plasmid DNA

The binding of DNA to surfaces can also cause a contraction of its structure²⁰⁸ and may lead to a similar decrease in the local dielectric constant. To explore such effects, measurements of ϵ were undertaken for DNA bound to aminosilane gradients exhibiting a spatially varying density of amine groups. As with the solution-phase experiments, these studies were performed under 0.01

mM to 10 mM pH ~ 7.2 PBS buffers incorporating 40 pM plasmid DNA and 14.4 nM NR. These solutions were left in contact with the amine gradients for a minimum of 5 min prior to imaging and remained in contact with the gradients for the duration of each experiment. The pKa of surface-bound ammonium groups has been reported to be ~ 7,¹⁹⁴ and our earlier studies show that the high amine end of similar gradients carries a positive charge under the present conditions.⁶³ Binding of DNA to the high amine end is therefore expected to involve a combination of coulombic and hydrophobic interactions. Similarly, the negative charge carried by the low amine (high silica) end of the gradient under the same conditions⁶³ likely prevents binding of DNA at low ionic strengths.

Figure 7.5 shows representative two-color fluorescence images of surface-adsorbed, NRdoped DNA molecules. Surface-adsorbed DNA molecules appeared as bright, immobile fluorescent spots that remained at the same location over several video frames. The individual fluorescent spots are attributed to adsorption of single DNA molecules. While DNA can form aggregates in the presence of polyamines,^{209,210} their formation is usually observed at much higher DNA concentrations. Neither the video data obtained here nor in our previous studies¹⁸² provide clear evidence of aggregate formation on the amine gradient surface. The vast majority of DNA molecules were observed to adsorb onto the surface in a single event. The fluorescence from each molecule remained approximately constant or slowly decreased after adsorption. Little if any evidence for stepwise increases in fluorescence from these same spots was observed, as might be expected if aggregation of the DNA occurred on the gradient surface. Control experiments performed in the absence of DNA yielded fluorescent spots that were ~ 20-50-fold weaker, consistent with the assignment of the bright spots to NR-doped DNA. The E value for each spot was again obtained from the background-subtracted fluorescence signals in each of the two imaging channels.

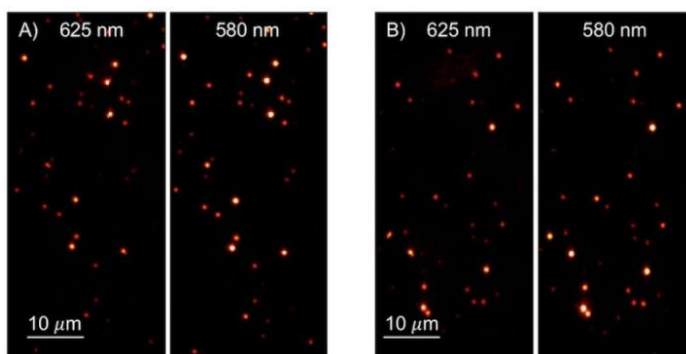


Figure 7.5 Two-color fluorescence images of NR-doped A) supercoiled and B) relaxed plasmid DNA adsorbed at the high amine end (6 mm position) of an APTMOS-derived gradient. These images were acquired under 2.5 mM pH ~ 7.2 PBS buffer. The color scale for both images is the same and depicts photon counts up to 1000 counts/pixel. Reprinted with permission from Ref (211). Copyright © 2018, American Chemical Society.

Figure 7.5 plots the average CM factors and dielectric constants (ϵ) for surface-adsorbed DNA molecules as a function of gradient position and buffer concentration. The reproducibility of the data was verified by repeating the experiments on several different gradients prepared on different days. Data from the lowest buffer concentrations (0.01 mM and 0.1 mM) were discarded because they produced very few detectable DNA adsorption events. The CM factors and ϵ for the supercoiled and relaxed forms of the DNA were again found to be statistically indistinguishable from each other, confirming that conformational changes associated with superhelical twisting have little impact on ϵ for the least polar environments.

The polarity of the microenvironments was once again observed to vary as a function of buffer concentration, and also as a function of position along each gradient. At low PBS concentration, ϵ was measured to be ~ 1.90 and ~ 2.84 in DNA adsorbed at the high and low amine ends of the gradient, respectively. Similar to the solution-phase experiments, the ϵ value at the low amine (high silica) end also decreased as the PBS concentration increased. At the high amine end, ϵ remained approximately constant across the buffer concentrations employed. It is concluded that

binding of the DNA to the amine groups at the high amine end of the gradient causes a condensation of the DNA structure and a corresponding decrease in ϵ as the microenvironments take on greater organic character and the associated dipoles become less mobile. Condensation of the DNA is again attributed to screening of the negatively charged phosphate groups by the ions on the surface and in solution. Increased ionic strength may also lead to closer approach of the DNA to the silica surface. However, the latter would likely cause an increase in ϵ at the low amine end with increasing ionic strength, and is discounted as a possible explanation.

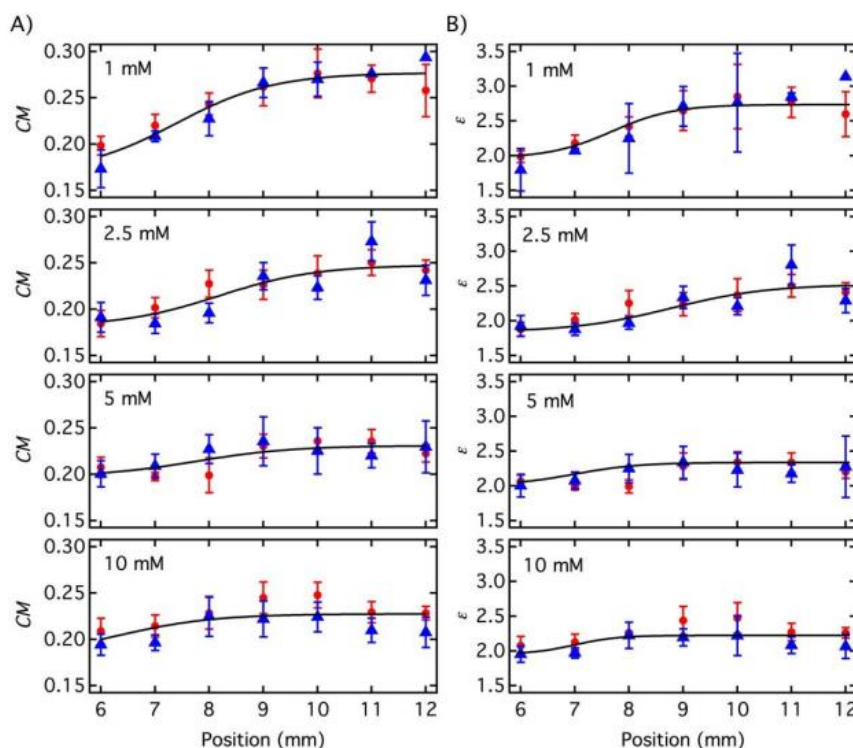


Figure 7.6 A) CM factor and B) dielectric constant for Nile Red doped supercoiled (red points) and relaxed (blue triangles) plasmid DNA as a function of position along APTMOS-derived gradients, and as a function of buffer concentration. All DNA molecules analyzed were adsorbed on the gradient surface. The 6 mm position represents the high amine end, with decreasing amine coverage towards the 12 mm position. The error bars show the 95%

confidence intervals for each value. Reprinted with permission from Ref (211). Copyright © 2018, American Chemical Society.

7.4 Conclusion

In summary, the present studies provide experimental confirmation that NR behaves as an intercalator when binding to DNA, and that the dielectric constant of the microenvironments in which it binds is small and similar to that predicted in computational studies. More importantly, the results obtained provide new knowledge on how the local dielectric constant within dsDNA is impacted by changes in the solution ionic strength and binding to amine-modified surfaces. The results showed that there is no measureable difference in ϵ for the least polar microenvironments in relaxed and supercoiled forms of plasmid DNA. In contrast, a clear decrease in ϵ was observed with increasing ionic strength and for higher amine density along chemically graded surfaces. These results provide an enhanced understanding of the least polar microenvironments in DNA and the factors that determine their dielectric constants.

Chapter 8 - General Conclusions and Future Directions

8.1 General Conclusions

This dissertation presents the qualitative and quantitative characterization of mass-transport phenomena in the nanoscale structures formed by surfactant templated mesoporous silica materials using SMT. SMT methods provide several significant advantages over more conventional microscopic methods (e.g., SEM/TEM, and AFM) and those that probe materials at the ensemble level (e.g., SAXS and XRD). Since SMT offers the capability to observe dynamics at the single molecule and single event levels, SMT provides quantitative information on the temporal and nanoscale spatial heterogeneity of many samples under various environments (e.g., in ambient air, under controlled environments, and in solution).⁵³ The conventional ensemble methods do not provide single molecule and single event level information due to data averaging. The advantages of SMT methods include capabilities to detect, observe and visualize nanoscale domains and nanopore morphologies with high spatial resolution.^{9,53}

By locating individual molecules confined within the pores of a nanoporous material, and tracking the motions of these molecules, information on materials structure and organization can be obtained, along with its ability to support mass transport of the molecules. The properties of nanostructured materials were quantitatively assessed by monitoring the diffusive motions of individual fluorescence probe molecules incorporated in the mesoporous silica materials which yield the trajectories of their confined molecular pathways. These observed fluorescence spots can be further analyzed to quantitatively characterize the mass-transport characteristics and nanoscale structures in surfactant templated mesoporous silica materials. The parameters associated with mass-transport and structural characteristics of mesoporous silica materials were obtained by employing the orthogonal regression analysis. By fitting the single-molecule trajectories to linear functions, the analysis yields important parameters such as trajectory angle, the angle error, and the variances of single-molecule positions along and across the trajectory direction. The trajectory

angle is a quantitative measure of the in-plane orientation of the 1D nanostructures. The orientational order can be quantified via a 2D order parameter and relates the deviation of individual trajectories from the mean trajectory orientation. The angular and positional error afforded useful means to distinguish mobile and immobile population as well as to determine the dimensionalities of the motions exhibited by mobile molecules.

The work described in the three experimental chapters presented in this dissertation used single-molecule methods to 1) identify the specific location (i.e., the environment) of probe molecules diffusing through surfactant- and solvent-filled silica mesopores (Chapter 5), 2) determine how the charge of the probe molecules affect mass transport and orientational confinement within surfactant- and solvent-filled silica mesopores (Chapter 5), and 3) characterize the nanoscale polarity properties of DNA (Chapter 7).

In Chapter 5, SMT imaging afforded a direct visualization of the structural and mass transport characteristics of solvent-filled surfactant-templated mesoporous silica materials. The modified SMT method sSMT was used to quantitatively assess the local dielectric constant of the nanoscale domains within surfactant- and solvent-filled silica mesopores. The solvatochromic and hydrophobic NR dye was used as a model probe. The sSMT studies and solvatochromatic character of NR were employed to determine its mobility and location in the mesoporous silica materials. The obtained relationship between emission ratio $(I_{625} - I_{580})/(I_{625} + I_{580})$ of the probe molecules and CM factor was used for the quantitative determination of the polarity environment of the NR molecules. The SMEP technique was used to demonstrate that the NR molecules diffuse with their long axes aligned parallel to the long axis of the pores and that they were orientationally confined within the pores. The sSMT and SMEP techniques demonstrated that NR molecules were tightly confined to regions having polarities similar to that of n-hexane in the CTAB-filled mesopores. It was concluded that the dye molecules were largely restricted to the hydrophobic core regions of the micelles filled pores, rather than locating near the silica/surfactant interface.

The sSMT results suggested that some polar solvent molecules (i.e., ethanol) may have also been incorporated within the micelles. Importantly, the regions to which the molecules were confined were shown to be much smaller than the physical diameter of the pores. The diameter of these pathways was found to be ~ 0.6 nm for the NR dye, a value that is similar to the ~ 1 nm pathway diameter obtained in previous studies of PDI dyes.^{27,28} These results suggest that the micelles filling the pores limit the interactions between the probe molecules and the silica pore walls. This study provided better evidence to assess the nanoscale structure inside the solvent and surfactant filled pores of mesoporous silica materials. It was concluded that the silica pores consist of nanoscale regions with different polarities and analytes selectively locate in specific polarity regions. Knowledge of such phenomena is of critical importance to understanding the mechanisms governing mass transport and molecule–matrix interactions within such nanostructural materials. This will further facilitate the development and optimization of solution-phase applications (e.g., solution-phase catalysis³⁻⁵ and chemical separations⁶⁻⁸ of mesoporous silica and other nanoporous materials.

Both Chapters 5 and 6 present studies demonstrating that nanostructuring of the solvent and surfactant medium filling the cylindrical pores of spin-coated mesoporous silica films plays an important role in governing the diffusive translational and orientational motions of incorporated reagents and analytes. The work presented in Chapter 6 of this dissertation used SMT methods to determine how the charge of the probe molecules affect mass transport and orientational confinement within surfactant- and solvent-filled silica mesopores. The charged and neutral PDI dyes employed were used to understand the location of the probe molecules within the pores, and their electrostatic interactions with the micelle and pore surfaces. By employing neutral and charge PDI molecules, more evidence of nanoscale heterogeneity within the pore structure was also obtained. The mobility population data reveal a charge dependence to dye molecule mobility that provides evidence the probe molecules are more affected by the positive charge of the surfactant

head groups of the micelle structures than the negative charges of the silica surface. The SMEP measurements again showed that all four dyes exhibited tight orientational confinement within the CTAB-filled mesopores, regardless of their size or charge. It was concluded that the probe molecules were located within the micelle cores and were more affected by the positive charge of the micelle surface than the negatively charged silica surface outside the micelles. The absence of evidence for any effects of the negative charge on the silica surface suggests the molecules are screened from interacting with the silica surface by the cationic CTAB head groups. The SMT results also provided evidence that mass transport of the dyes occurred by both Fickian diffusion and anomalous diffusion mechanisms within the solvent-filled surfactant-templated mesoporous silica nanostructures. The observed molecular mobility data and mechanisms of mobility provide evidence of nanoscale heterogeneity within the pore structure. The heterogeneity could be a result of the solvent island (e.g., water) or irregularity in the formed micellar structures such as the presence of spherical micelles.

In Chapter 7, sSMT data were employed to determine the local dielectric constant of the least polar environments in plasmid DNA both in solution and for DNA molecules absorbed to aminosilane gradient surfaces. This work provided important knowledge of the factors governing the polarity of DNA microenvironments to which intercalators bind. The solvatochromic NR dye was used to probe the plasmid DNA in these studies. The results obtained showed that NR was present in very low polarity environments, providing conclusive evidence that NR behaves as an intercalator, rather than binding to the more polar minor groove. It can be concluded from our results that the NR dye intercalates into the DNA by inserting between the stacked base pairs. The NR data also reveal that the local dielectric constant inside the DNA decreased with increasing solution ionic strength and with increasing amine coverage on amine-modified silica gradient surfaces. An increase in the buffer concentration again led to a decrease in ϵ , but only at the low amine end of the gradient. It was concluded that high buffer concentrations and binding to an

amine surface cause condensation of the DNA, forming less polar microenvironments within its structure. This study provided, to our knowledge, the first quantitative experimental evidence that NR behaves as an intercalator in DNA. This study also further demonstrated the successful application of sSMT and the NR dye for exploration of the local polarity properties in nanostructured materials.

This dissertation has described the application of SMT methods for characterization of the nanoscale structures and mass-transport characteristics of surfactant templated mesoporous silica materials. Importantly, the SMT studies revealed that the probe molecules employed were confined within the cylindrical pores of mesoporous silica materials. Furthermore, the sSMT technique provided evidence of the location of the probe molecules inside the pore structure. The sSMT and SMEP measurements performed using NR revealed that the molecules were confined to the hydrophobic cores of the micelles filling the silica mesopores. The studies employing charged PDI probe molecules in solvent- and surfactant-filled mesoporous silica provided more evidence of analyte location. The results again indicated the molecules were confined within the micelles and interacted more strongly with the positively charge micellar surface, rather than the negatively charged silica pore walls. Also, SMT measurements revealed more evidence of nanoscale surface heterogeneity within the pores. These studies afford an enhanced understanding of how nanostructuring of the pore-filling medium in solvent- and surfactant-filled mesoporous materials governs the mass transport and surface interactions of incorporated reagents and analytes.

Overall, this dissertation helps to demonstrate the significant advantages of SMT methods over more conventional tools in studying mass transport phenomena in solution-filled nanoporous materials. But there are several possible challenges associated with single-molecule methods. The limited brightness of probe molecules can decrease the signal-to-noise (S/N) ratio. Because the localization precision scales with the number of photons collected, brighter probes and higher S/N

ratio are important. Therefore, the brightness of the selected probe dyes needs to be in the detectable range under the experimental conditions. Increasing the laser power can increase the S/N ratio, but this can also result in heavy photobleaching. Therefore, probe molecules of higher photostability are important in increasing S/N. Also, highly photostable probe molecules facilitate the recording of sufficiently long videos with longer trajectories, which will help the mapping of longer nanostructures. The existence of fluorescent impurities is a long-standing obstacle in single-molecule imaging, where misidentification of fluorescent impurities as probe dye molecules can alter the final results. Therefore it is important to eliminate the possibility of impurities by taking specific care and steps in sample preparation.

8.2 Future Directions

Overall, this dissertation has investigated the nanoscale structural properties and mass transport of mesoporous silica materials. All measurements were conducted on a similar system by changing the probe dye molecules. In the solution-phase applications (e.g., solution-phase catalysis³⁻⁵ and chemical separations⁶⁻⁸) of mesoporous silica the knowledge of mobility of the entrapped dye, its location and strength of its interactions with the pore surfaces are important. The above-stated facts play a profound role in governing ultimate application performance characteristics.

To collect more evidence, similar SMT measurements can be conducted on different mesoporous systems. The different mesoporous systems can exhibit different properties that can result in different mass transport properties. For example, mesoporous silica materials incorporating different surfactants (eg. FI27 and P123) as structural templates can offer different sized nanopore structures. This would facilitate studies of the effects of pore size on mass transport and orientational confinement of analytes within surfactant- and solvent-filled silica mesopores. Such studies could also demonstrate the tunable pore size of mesoporous silica materials. The

different pore size may cause a major effect on interactions between the pore surface and analyte molecule, which could ultimately effect the application performance. Also, a change in the surfactant template could lead to changes in the charge distribution inside the pore structure. So far we were able to study the effect of positively charge surfactant head groups on analyte molecules and on the silica surface. In this dissertation, Chapter 6 provided evidence of silica surface screening by the micelle surface. By changing the surfactant, we would be able to observe the effect of different surfactant micelles to assist or limit interactions between the probe molecules and the silica pore walls. This may also change the location of the molecules and their confinement due to different polarity environments and interactions.

Furthermore, removing the surfactant templates from the mesoporous silica structures can offer valuable information on the interactions between pore surfaces and analyte molecules. Even though we have been unsuccessful in removing the surfactant template from mesoporous silica structures to date, SMT measurements of mesoporous silica structures with the surfactant removed could offer valuable information to understand the nanoscale structural properties and mass transport within mesoporous silica materials. The absence of the surfactant template could provide the analyte and solvent molecules the capability to reach much closer to the silica surface and to experience stronger interactions with the surface charge. Once the analyte molecule gains direct contact with the negatively charged silica surface, properties such as mobility of the entrapped dye, its location, its confinement and strength of its interactions with the pore surfaces are certain to change. The additional knowledge gained would allow users of these materials to change and optimize application performance.

References

- (1) Beck, J. S.; Vartuli, J. C.; Roth, W. J.; Leonowicz, M. E.; Kresge, C. T.; Schmitt, K. D.; Chu, C. T.-W.; Olson, D. H.; Sheppard, E. W.; McCullen, S. B.; Higgins, J. B.; Schlenker, J. L. A New Family of Mesoporous Molecular Sieves Prepared with Liquid Crystal Templates. *J. Am. Chem. Soc.* **1992**, *114*, 10834-10843.
- (2) Mütter, D.; Shin, T.; Deme, D.; Fratzl, P.; Paris, O.; Findenegg, G. H. Surfactant Self-Assembly in Cylindrical Silica Nanopores. *J. Phys. Chem. Lett.* **2010**, *1*, 1442-1446.
- (3) Corma, A. From Microporous to Mesoporous Molecular Sieve Materials and Their Use in Catalysis. *Chem. Rev.* **1997**, *97*, 2373-2419.
- (4) Hoffmann, F.; Cornelius, M.; Morell, J.; Fröba, M. Silica-Based Mesoporous Organic-Inorganic Hybrid Materials. *Angew. Chem. Int. Ed.* **2006**, *45*, 3216-3251.
- (5) Ren, Y.; Yue, B.; Gu, M.; He, H. Progress of the Application of Mesoporous Silica-Supported Heteropolyacids in Heterogeneous Catalysis and Preparation of Nanostructured Metal Oxides. *Materials* **2010**, *3*, 764-785.
- (6) Urbanski, R.; Goralska, E.; Bart, H.-J.; Szymanowski. Ultrafiltration of Surfactant Solutions. *J. Collid. Interface Sci.* **2002**, *253*, 419.
- (7) Schmuhl, R.; van den Berg, A.; Blank, D. H. A.; ten Elshof, J. E. Surfactant-Modulated Switching of Molecular Transport in Nanometer-Sized Pores of Membrane Gates. *Angew. Chem. Int. Ed.* **2006**, *45*, 3341-3345.
- (8) Deen, W. M. Hindered Transport of Large Molecules in Liquid-Filled Pores. *AIChE J.* **1987**, *33*, 1409-1425.
- (9) Higgins, D. A.; Park, S. C.; Tran-Ba, K.-H.; Ito, T. Single-Molecule Investigations of Morphology and Mass Transport Dynamics in Nanostructured Materials. *Annu. Rev. Anal. Chem.* **2015**, *8*, 193-216.
- (10) Gelb, L. D.; Gubbins, K. E.; Radhakrishnan, R.; Sliwinska-Bartkowiak, M. Phase Separation in Confined Systems. *Rep. Prog. Phys.* **1999**, 1573-1659.
- (11) Farrer, R. A.; Fourkas, J. T. Orientational Dynamics in Nanoporous Sol-Gel Glasses Studied by Optical Kerr Effect Spectroscopy. *Acc. Chem. Res.* **2003**, *36*, 605-612.
- (12) Alba-Simionesco, C.; Coasne, B.; Dosseh, G.; Dudziak, G.; Gubbins, K. E.; Radhakrishnan, R.; Sliwinska-Bartkowiak, M. Effects of Confinement on Freezing and Melting. *J. Phys.: Condens. Matter* **2006**, *18*, R15-R68.

- (13) Fayer, M. D.; Levinger, N. E. Analysis of Water in Confined Geometries and at Interfaces. *Annu. Rev. Anal. Chem.* **2010**, *3*, 89-107.
- (14) Thompson, W. H. Solvation Dynamics and Proton Transfer in Nanoconfined Liquids. *Annu. Rev. Phys. Chem.* **2011**, *62*, 599-619.
- (15) Stallmach, F.; Gräser, A.; Kärger, J.; Krause, C.; Jeschke, M.; Oberhagemann, U.; Spange, S. Pulsed Field Gradient NMR Studies of Diffusion in MCM-41 Mesoporous Solids. *Microporous and Mesoporous Materials* **2001**, *44-45*, 745-753.
- (16) Wessig, M.; Spitzbarth, M.; Drescher, M.; Winter, R.; Polarz, S. Multiple Scale Investigation of Molecular Diffusion Inside Functionalized Porous Hosts Using a Combination of Magnetic Resonance Methods. *Phys. Chem. Chem. Phys.* **2015**, *17*, 15976-15988.
- (17) Okazaki, M.; Toriyama, K. Inhomogeneous Distribution and Collective Diffusion of Solution Molecules in the Nanochannel of Mesoporous Silica. *J. Phys. Chem. B* **2003**, *107*, 7654-7658.
- (18) Okazaki, M.; Toriyama, K. Spin-Probe ESR Study on the Dynamics of Liquid Molecules in the MCM-41 Nanochannel: Temperature Dependence on 2-Propanol and Water. *J. Phys. Chem. B* **2005**, *109*, 13180-13185.
- (19) Kirstein, J.; Platschek, B.; Jung, C.; Brown, R.; Bein, T.; Bräuchle, C. Exploration of Nanostructured Channel Systems with Single-Molecule Probes. *Nature Materials* **2007**, *6*, 303-310.
- (20) Sanabria, H.; Kubota, Y.; Waxham, M. N. Multiple Diffusion Mechanisms Due to Nanostructuring in Crowded Environments. *Biophys. J.* **2007**, *92*, 313-322.
- (21) Ye, F.; Higgins, D. A.; Collinson, M. M. Probing Chemical Interactions at the Single-Molecule Level in Mesoporous Silica Thin Films. *J. Phys. Chem. C* **2007**, *111*, 6772-6780.
- (22) Ghosh, S.; Mandal, U.; Adhikari, A.; Bhattacharyya, K. Study of Diffusion of Organic Dyes in a Triblock Copolymer Micell and Gel by Fluorescence Correlation Spectroscopy. *Chem. Asian J.* **2009**, *4*, 948-954.
- (23) Davies, M.; Rühle, B.; Li, C.; Müllen, K.; Bein, T.; Bräuchle, C. Insights into Nanoscale Electrophoresis of Single Dye Molecules in Highly Oriented Mesoporous Silica Channels. *J. Phys. Chem. C* **2014**, *118*, 24013-24024.
- (24) Park, S. C.; Ito, T.; Higgins, D. A. On the Dimensionality of Diffusion in Flow-Aligned Surfactant-Templated Mesoporous Silica: A Single Molecule Tracking Study of Pore Wall Permeability. *J. Phys. Chem. C* **2015**, *119*, 26101-26110.

- (25) Harvey, J. A.; Thompson, W. H. Solute Location in a Nanoconfined Liquid Depends on Charge Distribution. *J. Chem. Phys.* **2015**, *143*, 044701.
- (26) Harvey, J. A.; Thompson, W. H. Thermodynamic Driving Forces for Dye Molecule Position and Orientation in Nanoconfined Solvents. *J. Phys. Chem. B* **2015**, *119*, 9150-9159.
- (27) Pramanik, R.; Ito, T.; Higgins, D. A. Single Molecule Wobbling in Cylindrical Mesopores. *J. Phys. Chem. C* **2013**, *117*, 3668-3673.
- (28) Pramanik, R.; Ito, T.; Higgins, D. A. Molecular Length Dependence of Single Molecule Wobbling within Surfactant- and Solvent-Filled Silica Mesopores. *J. Phys. Chem. C* **2013**, *117*, 15438-15446.
- (29) Beck, R. E.; Schultz, J. S. Hindered Diffusion in Microporous Membranes with Known Pore Geometry. *Science* **1970**, *170*, 1302-1305.
- (30) Jung, C.; Kirstein, J.; Platschek, B.; Bein, T.; Budde, M.; Frank, I.; Müllen, K.; Michaelis, J.; Bräuchle, C. Diffusion of Oriented Single Molecules with Switchable Mobility in Networks of Long Unidimensional Nanochannels. *J. Am. Chem. Soc.* **2008**, *130*, 1638-1648.
- (31) Maiti, N. C.; Krishna, M. M. G.; Britto, P. J.; Periasamy, N. Fluorescence Dynamics of Dye Probes in Micelles. *J. Phys. Chem. B* **1997**, *101*, 11051-11060.
- (32) Deye, J. F.; Berger, T. A.; Anderson, A. G. Nile Red as a Solvatochromic Dye for Measuring Solvent Strength in Normal Liquids and Mixtures of Normal Liquids with Supercritical and Near Critical Fluids. *Anal. Chem.* **1990**, *62*, 615-622.
- (33) Dickson, R. M.; Norris, D. J.; Tzeng, Y.-L.; Sakowicz, R.; Goldstein, L. S. B.; Moerner, W. E. Single Molecules Solvated in Pores of Polyacrylamide Gels. *Mol. Cryst. Liq. Cryst.* **1996**, *291*, 31-39.
- (34) Hou, Y.; Bardo, A. M.; Martinez, C.; Higgins, D. A. Characterization of Molecular Scale Environments in Polymer Films by Single Molecule Spectroscopy. *J. Phys. Chem. B* **2000**, *104*, 212-219.
- (35) Datta, A.; Mandal, D.; Pal, S. K.; Bhattacharyya, K. Intramolecular Charge Transfer Processes in Confined Systems. Nile Red in Reverse Micelles. *J. Phys. Chem. B* **1997**, *101*, 10221-10225.
- (36) Hungerford, G.; Castanheira, E. M. S.; Real Oliveira, M. E. C. D.; da Graca Miguel, M.; Durrows, H. D. Monitoring Ternary Systems of C12E5/Water/Tetradecane via the Fluorescence of Solvatochromic Probes. *J. Phys. Chem. B* **2002**, *106*, 4061-4069.
- (37) Kurniasih, I. N.; Liang, H.; Mohr, P. C.; Khot, G.; Rabe, J. P.; Mohr, A. Nile Red Dye in Aqueous Surfactant and Micellar Solution. *Langmuir* **2015**, *31*, 2639-2648.

- (38) Tran Ba, K. H.; Everett, T. A.; Ito, T.; Higgins, D. A. Trajectory Angle Determination in One Dimensional Single Molecule Tracking Data by Orthogonal Regression Analysis. *Phys. Chem. Chem. Phys.* **2011**, *13*, 1827-1835.
- (39) Jung, C.; Schwaderer, P.; Dethlefsen, M.; Köhn, R.; Michaelis, J.; Bräuchle, C. Visualization of the Self-Assembly of Silica Nanochannels Reveals Growth Mechanism. *Nature Nanotechnology* **2011**, *6*, 87-92.
- (40) Sbalzarini, I. F.; Koumoutsakos, P. Feature Point Tracking and Trajectory Analysis for Video Imaging in Cell Biology. *J. Struct. Biol.* **2005**, *151*, 182-195.
- (41) Giri, D.; Hanks, C. N.; Collinson, M. M.; Higgins, D. A. Single-Molecule Spectroscopic Imaging Studies of Polarity Gradients Prepared by Infusion-Withdrawal Dip-Coating. *J. Phys. Chem. C* **2014**, *118*, 6423-6432.
- (42) Hess, C. M.; Riley, E. A.; Palos-Chavez, J.; Reid, P. J. Measuring the Spatial Distribution of Dielectric Constants in Polymers through Quasi-Single Molecule Microscopy. *J. Phys. Chem. B* **2013**, *117*, 7106-7112.
- (43) Bardo, A. M.; Collinson, M. M.; Higgins, D. A. Nanoscale Properties and Matrix-Dopant Interactions in Dye-Doped Organically Modified Silicate Thin Films. *Chem. Mater.* **2001**, *13*, 2713-2721.
- (44) Cser, A.; Nagy, K.; Biczok, L. Fluorescence Lifetime of Nile Red as a Probe for the Hydrogen Bonding Strength with its Microenvironment. *Chem. Phys. Lett.* **2002**, *360*, 473-478.
- (45) Schmidt, T.; Schütz, G. J.; Baumgartner, W.; Gruber, H. J.; Schindler, H. Imaging of Single Molecule Diffusion. *Proc. Natl. Acad. Sci. USA* **1996**, *93*, 2926-2929.
- (46) Martin-Brown, S. A.; Fu, Y.; Saroja, G.; Collinson, M. M.; Higgins, D. A. Single-Molecule Studies of Diffusion by Oligomer-Bound Dyes in Organically Modified Sol-Gel-Derived Silicate Films. *Anal. Chem.* **2005**, *77*, 486-494.
- (47) Greenspan, P.; Fowler, S. D. Spectrofluorometric Studies of the Lipid Probe, Nile Red. *J. Lipid Res.* **1985**, *26*, 781-789.
- (48) Dutta, A. K.; Kamada, K.; Ohta, K. Spectroscopic Studies of Nile Red in Organic Solvents and Polymers. *J. Photochem. Photobiol. A* **1996**, *93*, 57-64.
- (49) Sarkar, N.; Das, K.; Nath, D. N.; Bhattacharyya, K. Twisted Charge Transfer Process of Nile Red in Homogeneous Solution and in Fauhasite Zeolite. *Langmuir* **1994**, *10*, 326-329.
- (50) Dias, L. C.; Custodio, R.; Pessine, F. B. T. Theoretical Studies of Nile Red by Ab Initio and Semiempirical Methods. *Chem. Phys. Lett.* **1999**, *302*, 505-510.

- (51) Freidzon, A. Y.; Safonov, A. A.; Bagaturyants, A. A.; Alfimov, M. V. Solvatofluorochromism and Twisted Intramolecular Charge-Transfer State of the Nile Red Dye. *Quantum Chem.* **2012**, *112*, 3059-3067.
- (52) Lipari, G.; Szabo, A. Effect of Librational Motion on Fluorescence Depolarization and Nuclear Magnetic Resonance Relaxation in Macromolecules and Membranes. *Biophys. J.* **1980**, *30*, 489-506.
- (53) Higgins, D. A.; Tran-Ba, K.-H.; Ito, T. Following Single Molecules to a Better Understanding of Self-Assembled One-Dimensional Nanostructures. *J. Phys. Chem. Lett.* **2013**, *4*, 3095-3103.
- (54) Frenkel, D.; Smit, B.: *Understanding Molecular Simulation: From Algorithms to Applications*; Academic Press: San Diego, **1996**.
- (55) Schmidt, M. W.; Baldrige, K. K.; Boatz, J. A.; Elbert, S. T.; Gordon, M. S.; Jensen, J. H.; Koseki, S.; Matsunaga, N.; Nguyen, K. A.; Su, S. J.; et al. General Atomic and Molecular Electronic Structure System. *J. Comput. Chem.* **1993**, *14*, 1347-1363.
- (56) Hanwell, M. D.; Curtis, D. E.; Lonie, D. C.; Vandermeersch, T.; Zurek, E.; Hutchison, G. R. Avogadro: An Advanced Semantic Chemical Editor, Visualization and Analysis Platform. *J. Cheminformatics* **2012**, *4*, 1-17.
- (57) Dutt, G. B.; Doraiswamy, S.; Periasamy, N. Molecular Reorientation Dynamics of Polar Dye Probes in Tertiary-Butyl Alcohol-Water Mixtures. *J. Chem. Phys.* **1991**, *94*, 5360- 5368.
- (58) Adcock, R. J. *A Problem in Least Squares*. *The Analyst* **1878**, *5*, 53-54.
- (59) Deming, W. E.: *Statistical Adjustment of Data*; Wiley: New York, **1943**.
- (60) Dunn, G.: *Statistical Evaluation of Measurement Errors: Design and Analysis of Reliability Studies*; Arnold: London, **2004**.
- (61) Thompson, R. E.; Larson, D. R.; Webb, W. W. Precise Nanometer Localization Analysis for Individual Fluorescent Probes. *Biophys. J.* **2002**, *82*, 2775-2783.
- (62) Bernreuther, M.; Buchholz, M.; Bungartz, H.-J.: *Aspects of a Parallel Molecular Dynamics Software for Nano-FLuidics*. In *Parallel Computing: Architectures, Algorithms and Applications*; Bischof, C., Brückner, M., Gibbon, P., Joubert, G. R., Lippert, T., Mohr, B., Peteres, F., Eds.; IOS Press: Amsterdam, **2008**; 53-60.
- (63) Ashraf, K. M.; Giri, D.; Wynne, K. J.; Higgins, D. A.; Collinson, M. M., Cooperative Effects in Aligned and Opposed Multicomponent Charge Gradients Containing Strongly Acidic, Weakly Acidic, and Basic Functional Groups. *Langmuir* **2016**, *32*, 3836-3847.

- (64) Kresge, C. T.; Leonowicz, M. E.; Roth, W. J.; Vartuli, J. C.; Beck, J. S. Ordered Mesoporous Molecular-Sieves Synthesized by a Liquid-Crystal Template Mechanism. *Nature* **1992**, *359*, 710-712.
- (65) Polarz, S.; Kuschel, A. Chemistry in Confining Reaction Fields with Special Emphasis on Nanoporous Materials. *Chem. - Eur. J.* **2008**, *14*, 9816-9829.
- (66) Wu, C. G.; Bein, T. Conducting Polyaniline Filaments in a Mesoporous Channel Host. *Science* **1994**, *264*, 1757-1759.
- (67) Llewellyn, P. L.; Ciesla, U.; Decher, H.; Stadler, R.; Schuth, F.; Unger, K. K. In Mcm-41 and Related Materials as Media for Controlled Polymerization Processes; Weitkamp, J Karge, HG Pfeifer, H Holderich, W., Ed.; Studies in Surface Science and Catalysis; **1994**, *84*, 2020.
- (68) Cardin, D. J.; Constantine, S. P.; Gilbert, A.; Lay, A. K.; Alvaro, M.; Galletero, M. S.; Garcia, H.; Marquez, F. Polymerization of Alkynes in the Channels of Mesoporous Materials Containing Ni and Zn Cations: Almost Complete Filling of the Voids. *J. Am. Chem. Soc.* **2001**, *123*, 3141-3142.
- (69) Lin, V. S. Y.; Radu, D. R.; Han, M. K.; Deng, W. H.; Kuroki, S.; Shanks, B. H.; Pruski, M. Oxidative Polymerization of 1,4-Diethynylbenzene into Highly Conjugated Poly(Phenylene Butadiynylene) within the Channels of Surface-Functionalized Mesoporous Silica and Alumina Materials. *J. Am. Chem. Soc.* **2002**, *124*, 9040-9041.
- (70) Wu, C. G.; Bein, T. Conducting Carbon Wires in Ordered, Nanometer-Sized Channels. *Science* **1994**, *266*, 1013-1015.
- (71) Xia, Y. N.; Yang, P. D.; Sun, Y. G.; Wu, Y. Y.; Mayers, B.; Gates, B.; Yin, Y. D.; Kim, F.; Yan, Y. Q. One-Dimensional Nanostructures: Synthesis, Characterization, and Applications. *Adv Mater* **2003**, *15*, 353-389.
- (72) Su, B.; Wu, Y.; Jiang, L. The Art of Aligning One-Dimensional (1D) Nanostructures. *Chem. Soc. Rev.* **2012**, *41*, 7832-7856.
- (73) Walcarius, A.; Sibottier, E.; Etienne, M.; Ghanbaja, J. Electrochemically Assisted Self Assembly of Mesoporous Silica Thin Films. *Nat. Mater.* **2007**, *6*, 602-608.
- (74) Goux, A.; Etienne, M.; Aubert, E.; Lecomte, C.; Ghanbaja, J.; Walcarius, A. Oriented Mesoporous Silica Films obtained by Electro-Assisted Self-Assembly (EASA). *Chem. Mater.* **2009**, *21*, 731-741.
- (75) Miyata, H. Epitaxial Growth of a Surfactant-Silica Mesostructure on Oriented Polyimide Films. *Microporous Mesoporous Mater.* **2007**, *101*, 296-302.

- (76) Miyata, H.; Kuroda, K. Preferred Alignment of Mesochannels in a Mesoporous Silica Film Grown on a Silicon (110) Surface. *J. Am. Chem. Soc.* **1999**, *121*, 7618-7624.
- (77) Yamaguchi, A.; Teramae, N. Fabrication and Analytical Applications of Hybrid Mesoporous Membranes. *Anal. Sci.* **2008**, *24*, 25-30.
- (78) Yamaguchi, A.; Kaneda, H.; Fu, W.; Teramae, N. Structural Control of Surfactant-Templated Mesoporous Silica Formed Inside Columnar Alumina Pores. *Adv Mater* **2008**, *20*, 1034-1037
- (79) Melosh, N. A.; Davidson, P.; Feng, P.; Pine, D. J.; Chmelka, B. F. Macroscopic Shear Alignment of Bulk Transparent Mesoporous Silica. *J. Am. Chem. Soc.* **2001**, *123*, 1240-1241.
- (80) Tolbert, S. H.; Firouzi, A.; Stucky, G. D.; Chmelka, B. F. Magnetic Field Alignment of Ordered Silicate-Surfactant Composites and Mesoporous Silica. *Science* **1997**, *278*, 264-268.
- (81) Stallmach, F.; Karger, J.; Krause, C.; Jeschke, M.; Oberhagemann, U. Evidence of Anisotropic Self-Diffusion of Guest Molecules in Nanoporous Materials of MCM-41 Type. *J. Am. Chem. Soc.* **2000**, *122*, 9237-9242.
- (82) Tran-Ba, K. H.; Higgins, D. A.; Ito, T. Single-Molecule Tracking Studies of Flow-Induced Microdomain Alignment in Cylinder-Forming Polystyrene-Poly(Ethylene Oxide) Diblock Copolymer Films. *J. Phys. Chem. B* **2014**, *118*, 11406-11415.
- (83) Ito, S.; Fukuya, S.; Kusumi, T.; Ishibashi, Y.; Miyasaka, H.; Goto, Y.; Ikai, M.; Tani, T.; Inagaki, S. Microscopic Structure and Mobility of Guest Molecules in Mesoporous Hybrid Organosilica: Evaluation with Single-Molecule Tracking. *J. Phys. Chem. C* **2009**, *113*, 11884-11891.
- (84) Yorulmaz, M.; Kiraz, A.; Demirel, A. L. Motion of Single Terrylene Molecules in Confined Channels of Poly(Butadiene)-Poly(Ethylene Oxide) Diblock Copolymer. *J. Phys. Chem. B* **2009**, *113*, 9640-9643.
- (85) Liao, Y.; Yang, S. K.; Koh, K.; Matzger, A. J.; Biteen, J. S. Heterogeneous Single-Molecule Diffusion in One-, Two-, and Three-Dimensional Microporous Coordination Polymers: Directional, Trapped, and Immobile Guests. *Nano Lett.* **2012**, *12*, 3080-3085.
- (86) Tran-Ba, K. H.; Finley, J. J.; Higgins, D. A.; Ito, T. Single-Molecule Tracking Studies of Millimeter-Scale Cylindrical Domain Alignment in Polystyrene-Poly(Ethylene Oxide) Diblock Copolymer Films Induced by Solvent Vapor Penetration. *J. Phys. Chem. Lett.* **2012**, *3*, 1968-1973.
- (87) Holmqvist, P.; Alexandridis, P.; Lindman, B. Phase Behavior and Structure of Ternary Amphiphilic Block Copolymer-Alkanol-Water Systems: Comparison of Poly(Ethylene

- Oxide) Poly(Propylene Oxide) to Poly(Ethylene Oxide) Poly(Tetrahydrofuran) Copolymers. *Langmuir* **1997**, *13*, 2471-2479.
- (88) Mann, S.; Burkett, S. L.; Davis, S. A.; Fowler, C. E.; Mendelson, N. H.; Sims, S. D.; Walsh, D.; Whilton, N. T. Sol-Gel Synthesis of Organized Matter. *Chem. Mater.* **1997**, *9*, 2300-2310.
- (89) Bagshaw, S. A.; Prouzet, E.; Pinnavaia, T. J. Templating of Mesoporous Molecular-Sieves by Nonionic Polyethylene Oxide Surfactants. *Science* **1995**, *269*, 1242-1244.
- (90) Walcarius, A.; Collinson, M. M. Analytical Chemistry with Silica Sol-Gels: Traditional Routes to New Materials for Chemical Analysis. *Annu. Rev. Anal. Chem.* **2009**, *2*, 121-143.
- (91) Brinker, C.; Scherer, G. In *Sol-Gel Science: The Physics and Chemistry of Sol-Gel Processing*. Section Title: Ceramics; Academic: New York, **1990**.
- (92) Hench, L. L.; West, J. K. The Sol-Gel Process. *Chem. Rev.* **1990**, *90*, 33-72.
- (93) Lofgreen, J. E.; Ozin, G. A. Controlling Morphology and Porosity to Improve Performance of Molecularly Imprinted Sol-Gel Silica. *Chem. Soc. Rev.* **2014**, *43*, 911-933.
- (94) Ito, S.; Kusumi, T.; Takei, S.; Miyasaka, H. Diffusion Processes of Single Fluorescent Molecules in a Polymer-Based Thin Material with Three-Dimensional Network. *Chem. Commun.* **2009**, 6165-6167.
- (95) Ye, F.; Collinson, M. M.; Higgins, D. A. What can be Learned from Single Molecule Spectroscopy? Applications to Sol-Gel-Derived Silica Materials. *Phys. Chem. Chem. Phys.* **2009**, *11*, 66-82.
- (96) Attard, G. S.; Glyde, J. C.; Goltner, C. G. Liquid-Crystalline Phases as Templates for the Synthesis of Mesoporous Silica. *Nature* **1995**, *378*, 366-368.
- (97) Goltner, C.; Antonietti, M. Mesoporous Materials by Templating of Liquid Crystalline Phases. *Adv Mater* **1997**, *9*, 431-436.
- (98) Monnier, A.; Schuth, F.; Huo, Q.; Kumar, D.; Margolese, D.; Maxwell, R. S.; Stucky, G. D.; Krishnamurty, M.; Petroff, P.; Firouzi, A.; Janicke, M.; Chmelka, B. F. Cooperative Formation of Inorganic-Organic Interfaces in the Synthesis of Silicate Mesostructures. *Science* **1993**, *261*, 1299-1303.
- (99) Boissiere, C.; Larbot, A.; van der Lee, A.; Kooyman, P. J.; Prouzet, E. A New Synthesis of Mesoporous MSU-X Silica Controlled by a Two-Step Pathway. *Chem. Mater.* **2000**, *12*, 2902-2913.

- (100) Firouzi, A.; Kumar, D.; Bull, L. M.; Besier, T.; Sieger, P.; Huo, Q.; Walker, S. A.; Zasadzinski, J. A.; Glinka, C.; Nicol, J.; Margolese, D.; Stucky, G. D.; Chmelka, B. F. Cooperative Organization of Inorganic-Surfactant and Biomimetic Assemblies. *Science* **1995**, *267*, 1138-1143.
- (101) Doshi, D. A.; Gibaud, A.; Goletto, V.; Lu, M. C.; Gerung, H.; Ocko, B.; Han, S. M.; Brinker, C. J. Peering into the Self-Assembly of Surfactant Templated Thin-Film Silica Mesophases. *J. Am. Chem. Soc.* **2003**, *125*, 11646-11655.
- (102) Weitzel, C. R.; Everett, T. A.; Higgins, D. A. Aggregation and its Influence on Macroscopic in-Plane Organization in Thin Films of Electrostatically Self-Assembled Perylene-Diimide/Polyelectrolyte Nanofibers. *Langmuir* **2009**, *25*, 1188-1195.
- (103) Ito, T. Block Copolymer-Derived Monolithic Polymer Films and Membranes Comprising Self-Organized Cylindrical Nanopores for Chemical Sensing and Separations. *Chem. - Asian J.* **2014**, *9*, 2708-2718.
- (104) Long, J. W.; Dunn, B.; Rolison, D. R.; White, H. S. Three-dimensional battery architectures. *ChTran-Baem. Rev.* **2004**, *104*, 4463-4492.
- (105) Baker, L. A.; Jin, P.; Martin, C. R. Biomaterials and biotechnologies based on nanotube membranes. *Crit. Rev. Solid State Mater. Sci.* **2005**, *30*, 183-205.
- (106) Davis, M. E. Ordered porous materials for emerging applications. *Nature* **2002**, *417*, 813-821.
- (107) Lu, Y. F.; Ganguli, R.; Drewien, C. A.; Anderson, M. T.; Brinker, C. J.; Gong, W. L.; Guo, Y. X.; Soye, H.; Dunn, B.; Huang, M. H.; Zink, J. I. Continuous formation of supported cubic and hexagonal mesoporous films by sol-gel dip-coating. *Nature* **1997**, *389*, 364-368.
- (108) Ogawa, M. Formation of Novel Oriented Transparent Films of Layered Silica-Surfactant Nanocomposites. *J. Am. Chem. Soc.* **1994**, *116*, 7941-7942.
- (109) Kandimalla, V. B.; Tripathi, V. S.; Ju, H. X. Immobilization of biomolecules in sol-gels: Biological and analytical applications. *Crit. Rev. Anal. Chem.* **2006**, *36*, 73-106.
- (110) Huo, Q. S.; Feng, J. L.; Schuth, F.; Stucky, G. D. Preparation of hard mesoporous silica spheres. *Chem. Mater.* **1997**, *9*, 14-17.
- (111) Wirnsberger, G.; Scott, B. J.; Stucky, G. D. pH Sensing with mesoporous thin films. *Chem. Comm.* **2001**, 119-120.
- (112) Scott, B. J.; Wirnsberger, G.; Stucky, G. D. Mesoporous and mesostructured materials for optical applications. *Chem. Mater.* **2001**, *13*, 3140-3150.

- (113) Ruhle, B.; Davies, M.; Lebold, T.; Brauchle, C.; Bein, T. Highly Oriented Mesoporous Silica Channels Synthesized in Microgrooves and Visualized with Single-Molecule Diffusion. *ACS Nano* **2012**, *6*, 1948-1960.
- (114) Kim, S. H.; Misner, M. J.; Xu, T.; Kimura, M.; Russell, T. P. Highly Oriented and Ordered Arrays from Block Copolymers via Solvent Evaporation. *Adv. Mater.* **2004**, *16*, 226-231.
- (115) Bang, J.; Kim, B. J.; Stein, G. E.; Russell, T. P.; Li, X.; Wang, J.; Kramer, E. J.; Hawker, C. J. Effect of Humidity on the Ordering of PEO-Based Copolymer Thin Films. *Macromolecules* **2007**, *40*, 7019-7025.
- (116) Keller, A.; Pedemonte, E.; Willmouth, F. M. Macro-lattice from Segregated Amorphous Phases of a Three Block Copolymer. *Nature* **1970**, *225*, 538-540.
- (117) Albalak, R. J.; Thomas, E. L. Microphase Separation of Block Copolymer Solutions in a Flow Field. *J. Polym. Sci., Part B Pol. Phys.* **1993**, *31*, 37-46.
- (118) Lodge, T. P.; Pudil, B.; Hanley, K. J. The Full Phase Behavior for Block Copolymers in Solvents of Varying Selectivity. *Macromolecules* **2002**, *35*, 4707-4717.
- (119) Pople, J. A.; Hamley, I. W.; Terrill, N. J.; Fairclough, J. P. A.; Ryan, A. J.; Yu, G.-E.; Booth, C. Shear-Induced Orientational Order in the Hexagonal Phase of Oxyethylene/Oxybutylene Diblock Copolymer Gels. *Polymer* **1998**, *39*, 4891-4896.
- (120) Pople, J. A.; Hamley, I. W.; Fairclough, J. P. A.; Ryan, A. J.; Booth, C. Orientational Ordering of a Poly(oxyethylene)-Poly(oxybutylene) Diblock Copolymer Gel under Steady Shear Flow. *Macromolecules* **1998**, *31*, 2952-2956.
- (121) Jain, A.; Hall, L. M.; Garcia, C. B. W.; Gruner, S. M.; Wiesner, U. Flow-Induced Alignment of Block Copolymer-Sol Nanoparticle Coassemblies toward Oriented Bulk Polymer-Silica Hybrids. *Macromolecules* **2005**, *38*, 10095-10100.
- (122) Shimizu, K.; Yasuda, T.; Saito, H. Perpendicular Orientation of Cylindrical Microdomains in Extruded Triblock Copolymer. *Macromolecules* **2010**, *43*, 2088-2091.
- (123) Moerner, W. E.; Fromm, D. P. Methods of Single-Molecule Fluorescence Spectroscopy and Microscopy. *Rev. Sci. Instrum.* **2003**, *74*, 3597-3619.
- (124) Axelrod, D.; Koppel, D. E.; Schlessinger, J.; Elson, E.; Webb, W. W. Mobility Measurement By Analysis Of Fluorescence Photobleaching Recovery Kinetics. *Biophys. J.* **1976**, 1055-1069.
- (125) Zuerner, A.; Kirstein, J.; Doblinger, M.; Brauchle, C.; Bein, T. Visualizing single-molecule diffusion in mesoporous materials. *Nature* **2007**, *450*, 705-709.

- (126) Hou, Y.; Higgins, D. A. Single Molecule Studies of Dynamics in Polymer Thin Films and at Surfaces: Effect of Ambient Relative Humidity. *J. Phys. Chem. B* **2002**, *106*, 10306-10315.
- (127) Dickson, R. M.; Norris, D. J.; Tzeng, Y.-L.; Moerner, W. E. Three-Dimensional Imaging of Single Molecules Solvated in Pores of Poly(acrylamide) Gels. *Science* **1996**, *274*, 966-969.
- (128) Sonnleitner, A.; Schutz, G. J.; Schmidt, T. Free Brownian Motion of Individual Lipid Molecules in Biomembranes. *Biophys. J.* **1999**, *77*, 2638-2642.
- (129) Ke, P. C.; Naumann, C. A. Single-Molecule Fluorescence Imaging of Phospholipid Monolayers at the Air-Water Interface. *Langmuir* **2001**, *17*, 3727-3733.
- (130) Ke, P. C.; Naumann, C. A. Hindered Diffusion in Polymer-Tethered Phospholipid Monolayers at the Air-Water Interface: A Single-Molecule Fluorescence Imaging Study. *Langmuir* **2001**, *17*, 5076-5081.
- (131) McCain, K. S.; Hanley, D. C.; Harris, J. M. Single-Molecule Fluorescence Trajectories for Investigating Molecular Transport in Thin Silica Sol-Gel Films. *Anal. Chem.* **2003**, *75*, 4351-4359.
- (132) Harms, G. S.; Cognet, L.; Lommerse, P. H. M.; Blab, G. A.; Schmidt, T. Autofluorescent Proteins in Single-Molecule Research: Applications to Live Cell Imaging Microscopy. *Biophys. J.* **2001**, *80*, 2396-2408.
- (133) Nishimura, S. Y.; Lord, S. J.; Klein, L. O.; Willets, K. A.; He, M.; Lu, Z.; Tweig, R. J.; Moerner, W. E. Diffusion of Lipid-Like Single-Molecule Fluorophores in the Cell Membrane. *J. Phys. Chem. B* **2006**, *110*, 8151-8157.
- (134) Werley, C. A.; Moerner, W. E. Single-molecule nanoprobe explores defects in spin-grown crystals. *J. Phys. Chem. B* **2006**, *110*, 18939-18944.
- (135) Hood, K.; Nix, B. A. J.; Iles, T. C. Asymptotic Information and Variance-Covariance Matrices for the Linear Structural Model. *The Statistician* **1999**, *48*, 477-493.
- (136) Jackson, C. L.; McKenna, G. B. The Melting Behavior of Organic Materials Confined in Porous Solids. *J. Chem. Phys.* **1990**, *93*, 9002-9011.
- (137) Jackson, C. L.; McKenna, G. B. The Glass Transition of Organic Liquids Confined to Small Pores. *J. Non Cryst. Solids* **1991**, *131*, 221-224.
- (138) Jackson, C. L.; McKenna, G. B. Vitrification and Crystallization of Organic Liquids Confined to Nanoscale Pores. *Chem. Mater.* **1996**, *8*, 2128-2137.

- (139) Takahara, S.; Kittaka, S.; Mori, T.; Kuroda, Y.; Takamuku, T.; Yamaguchi, T. Neutron Scattering and Dielectric Studies on Dynamics of Methanol and Ethanol Confined in MCM-41. *J. Phys. Chem. C* **2008**, *112*, 14385–14393.
- (140) Gupta, N. M.; Kumar, D.; Kamble, V. S.; Mitra, S.; Mukhopadhyay, R.; Kartha, V. B. Fourier Transform Infrared and Quasielectron Neutron Scattering Studies on the Binding Modes of Methanol Molecules in the Confined Spaces of HMCM-41 and HZSM-5: Role of Pore Structure and Surface Acid Sites. *J. Phys. Chem. B* **2006**, *110*, 4815–4823.
- (141) Kittaka, S.; Iwashita, T.; Serizawa, A.; Kranishi, M.; Takahara, S.; Kuroda, Y.; Mori, T.; Yamaguchi, T. Low Temperature Properties of Acetonitrile Confined in MCM-41. *J. Phys. Chem. B* **2005**, *109*, 23162–23169.
- (142) Morales, C. M.; Thompson, W. H. Simulations of Infrared Spectra of Nanoconfined Liquids: Acetonitrile Confined in Nanoscale, Hydrophilic Silica Pores. *J. Phys. Chem. A* **2009**, *113*, 1922–1933.
- (143) Harms, G. S.; Sonnleitner, M.; Schütz, G. J.; Gruber, H. J.; Schmidt, T. Single-Molecule Anisotropy Imaging. *Biophys. J.* **1999**, *77*, 2864–2870.
- (144) Fu, Y.; Ye, F.; Sanders, W. G.; Collinson, M. M.; Higgins, D. A. Single Molecule Spectroscopy Studies of Diffusion in Mesoporous Silica Thin Films. *J. Phys. Chem. B* **2006**, *110*, 9164–9170.
- (145) Martins, P.; Serrado Nunes, J.; Hungerford, G.; Miranda, D.; Ferreira, A.; Sencadas, V.; Lanceros-Méndez, S.; Local variation of the dielectric properties of poly(vinylidene fluoride) during the α - to β -phase transformation, *Phys. Lett. A* **2009**, *373*, 177–180.
- (146) Kumarasinghe, R.; Higgins, E.D.; Ito, T.; Higgins, D.A.; Spectroscopic and polarization-dependent Single-Molecule Tracking Reveal the One-Dimensional Diffusion Pathways in Surfactant-Templated Mesoporous Silica. *J. Phys. Chem. C*, **2016**, *120*, 715–723.
- (147) Martin CR, Nishizawa M, Jirage K, Kang M. Investigations of the transport properties of gold nanotubule membranes. *J. Phys. Chem. B* **2001**, *105*, 1925–1934.
- (148) Cussler EL. *Diffusion: Mass Transfer in Fluid Systems*. New York: Cambridge Univ. Press. **2009**
- (149) Axelrod D, Koppel DE, Schlessinger J, Elson E, Webb WW. Mobility measurement by analysis of fluorescence photobleaching recovery kinetics. *Biophys. J.* **1976**, *16*, 1055–1069.
- (150) Okamoto K, Shook CJ, Bivona L, Lee SB, English DS. 2004. Direct observation of wetting and diffusion in the hydrophobic interior of silica nanotubes. *Nano Lett.* **2004**, *4*, 233–239.

- (151) Moerner WE, Kador L. Optical detection and spectroscopy of single molecules in a solid. *Phys. Rev. Lett.* **1989**, *6*, 2535–2538.
- (152) Orrit M, Bernard J. Single pentacene molecules detected by fluorescence excitation in a p-terphenyl crystal. *Phys. Rev. Lett.* **1990**, *65*, 2716–2719.
- (153) Shera EB, Seitzinger NK, Davis LM, Keller RA, Soper SA. Detection of single fluorescent molecules. *Chem. Phys. Lett.* **1990**, *174*, 553–557.
- (154) Betzig E, Chichester RJ. Single molecules observed by near-field scanning optical microscopy. *Science* **1993**, *262*, 1422–1425.
- (155) Nie S, Chiu DT, Zare RN. Probing individual molecules with confocal fluorescence microscopy. *Science* **1994**, *266*, 1018–1021.
- (156) Eigen M, Rigler R. Sorting single molecules: applications to diagnostics and evolutionary biotechnology. *PNAS* **1994**, *91*, 5740–5747.
- (157) Higgins DA, Collinson MM. Gaining insight into the nanoscale properties of sol-gel-derived silicate thin films by single-molecule spectroscopy. *Langmuir* **2005**, *21*, 9023–9031.
- (158) Lebold T, Michaelis J, Brauchle C. The complexity of mesoporous silica nanomaterials unravelled “ by single-molecule microscopy. *Phys. Chem. Chem. Phys.* **2011**, *13*, 5017–5033.
- (159) Wirth MJ, Legg MA. Single-molecule probing of adsorption and diffusion on silica surfaces. *Annu. Rev. Phys. Chem.* **2007**, *58*, 489–510.
- (160) Shuang B, Chen J, Kisley L, Landes CF. Troika of single particle tracking programming: SNR enhancement, particle identification, and mapping. *Phys. Chem. Chem. Phys.* **2013**, *16*, 624–634.
- (161) Rust MJ, Bates M, Zhuang X. Sub-diffraction-limit imaging by stochastic optical reconstruction microscopy (STORM). *Nat. Methods* **2006**, *3*, 793–795.
- (162) Betzig E, Patterson GH, Sougrat R, Lindwasser OW, Olenych S, et al. Imaging intracellular fluorescent proteins at nanometer resolution. *Science* **2006**, *313*, 1642–1645.
- (163) Hess ST, Girirajan TPK, Mason MD. Ultra-high resolution imaging by fluorescence photoactivation localization microscopy. *Biophys. J.* **2006**, *91*, 4258–4272.
- (164) Soper SA, Shera EB, Martin JC, Jett JH, Hahn JH, et al. Single-molecule detection of rhodamine 6G in ethanolic solutions using continuous wave laser excitation. *Anal. Chem.* **1991**, *63*, 432–437.

- (165) Elson EL, Magde D. Fluorescence correlation spectroscopy. I. Conceptual basis and theory. *Biopolymers* **1974**, *13*, 1–27.
- (166) Aragon SR, Pecora R. Fluorescence correlation spectroscopy as a probe of molecular dynamics. *J. Chem. Phys.* **1976**, *64*, 1791–1803.
- (167) Wirth MJ, Swinton DJ. Single-molecule probing of mixed-mode adsorption at a chromatographic interface. *Anal. Chem.* **1998**, *70*, 5264–5271.
- (168) Yildiz A, Selvin PR. Fluorescence imaging with one nanometer accuracy: application to molecular motors. *Acc. Chem. Res.* **2005**, *38*, 574–582.
- (169) Enderlein J, Toprak E, Selvin PR. Polarization effect on position accuracy of fluorophore localization. *Opt. Express* **2006**, *14*, 8111–8120.
- (170) Kastantin M, Walder R, Schwartz DK. Identifying mechanisms of interfacial dynamics using single-molecule tracking. *Langmuir* **2012**, *28*, 12443–12456.
- (171) Peterson EM, Harris JM. Quantitative detection of single molecules in fluorescence microscopy images. *Anal. Chem.* **2010**, *82*, 189–196.
- (172) Everett, T. A.; Higgins, D. A.; Electrostatic Self-Assembly of Ordered Perylene-Diimide/Polyelectrolyte Nanofibers in Fluidic Devices: from Nematic Domains to Macroscopic Alignment. *Langmuir*, **2009**, *25*, 13045–13051.
- (173) Fangmao, Ye.; Higgins, D.A.; Maryanne M. Collinson, M. M.; Probing Chemical Interactions at the Single-Molecule Level in Mesoporous Silica Thin Films. *J. Phys. Chem. C* **2007**, *111*, 6772–6780.
- (174) Walder, R.; Nelson, N.; Schwartz, D. K. Single Molecule Observations of Desorption-Mediated Diffusion at the Solid-Liquid Interface. *Phys. Rev. Lett.* **2011**, *107*, 156102.
- (175) Bychuk, O. V.; O’Shaughnessy, B. Anomalous Surface Diffusion: A Numerical Study. *J. Chem. Phys.* **1994**, *101*, 772–780.
- (176) Bychuk, O. V.; O’Shaughnessy, B. Anomalous Diffusion at Liquid Surfaces. *Phys. Rev. Lett.* **1995**, *74*, 1795–1798.
- (177) Chechkin, A. V.; Zaid, I. M.; Lomholt, M. A.; Sokolov, I. M.; Metzler, R. Bulk-Mediated Diffusion on a Planar Surface: Full Solution. *Phys. Rev. E* **2012**, *86*, 041101.
- (178) Wu, S.-H.; Mou, C.-Y.; and Hong-Ping Lin, H.-P.; Synthesis of mesoporous silica nanoparticles. *Rev. Chem. Soc.* **2013**, 3862–3875.

- (179) Singh, L.P.; Bhattacharyya, S.K.; Kumar, R.; Mishra, G.; Sharma, U.; Singh, G.; Ahalwat, S.; Sol-Gel processing of silica nanoparticles and their applications. *Adv Colloid Interface Sci.* **2014**, *214*, 17-37.
- (180) Ober, R. J.; Tahmasbi, A.; Ram S.; Lin Z.; Ward, E. S.; Quantitative Aspects of Single Molecule Microscopy. *IEEE Signal Process Mag.* **2015**, *32*, 58–69.
- (181) Podesta, A.; Indrieri, M.; Brogioli, D.; Manning, G. S.; Milani, P.; Guerra, R.; Finzi, L.; Dunlap, D., Positively charged surfaces increase the flexibility of DNA. *Biophysical Journal* **2005**, *89*, 2558-2563.
- (182) Li, Z.; Ashraf, K. M.; Collinson, M. M.; Higgins, D. A., Single Molecule Catch and Release: Potential-Dependent Plasmid DNA Adsorption along Chemically Graded Electrode Surfaces. *Langmuir* **2017**, *33*, 8651-8662.
- (183) Genzer, J.; Bhat, R. R., Surface-bound soft matter gradients. *Langmuir* **2008**, *24*, 2294- 2317.
- (184) Genzer, J., Surface-Bound Gradients for Studies of Soft Materials Behavior. *Annual Review of Materials Research*, **2012**, *42*, 435-468.
- (185) Chaudhury, M. K.; Whitesides, G. M., How To Make Water Run Uphill. *Science* **1992**, *256*, 1539-1541.
- (186) Bloomfield, V. A., DNA condensation. *Current Opinion in Structural Biology* **1996**, *6*, 334-341.
- (187) Fiorilli, S.; Rivolo, P.; Descrovi, E.; Ricciardi, C.; Pasquardini, L.; Lunelli, L.; Vanzetti, L.; Pederzoli, C.; Onida, B.; Garrone, E., Vapor-phase self-assembled monolayers of aminosilane on plasma-activated silicon substrates. *Journal of Colloid and Interface Science* **2008**, *321*, 235-241.
- (188) Peterson, E. M.; Harris, J. M., Single-Molecule Fluorescence Imaging of DNA at a Potential-Controlled Interface. *Langmuir* **2013**, *29*, 8292-8301.
- (189) Xu, H.; Nagasaka, S.; Kameta, N.; Masuda, M.; Ito, T.; Higgins, D. A., Spectroscopic imaging studies of nanoscale polarity and mass transport phenomena in self-assembled organic nanotubes. *Physical Chemistry Chemical Physics* **2017**, *19*, 20040-20048.
- (190) Gattuso, H.; Besancenot, V.; Grandemange, S.; Marazzi, M.; Monari, A., From noncovalent binding to irreversible DNA lesions: Nile blue and Nile red as photosensitizing agents. *Scientific Reports* **2016**, *6*.
- (191) Collinson, M. M.; Higgins, D. A., Organosilane Chemical Gradients: Progress, Properties, and Promise. *Langmuir* **2017**, *33*, 13719-13732.

- (192) Stalder, A. F.; Melchior, T.; Muller, M.; Sage, D.; Blu, T.; Unser, M., Low-bond axisymmetric drop shape analysis for surface tension and contact angle measurements of sessile drops. *Colloids and Surfaces a-Physicochemical and Engineering Aspects* **2010**, *364*, 72-81.
- (193) Morgenthaler, S.; Zink, C.; Spencer, N. D., Surface-chemical and -morphological gradients. *Soft Matter* **2008**, *4*, 419-434.
- (194) vanderVegte, E. W.; Hadziioannou, G., Acid-base properties and the chemical imaging of surface-bound functional groups studied with scanning force microscopy. *Journal of Physical Chemistry B* **1997**, *101*, 9563-9569.
- (195) Lamm, G.; Pack, G. R., Calculation of dielectric constants near polyelectrolytes in solution. *Journal of Physical Chemistry B* **1997**, *101*, 959-965.
- (196) Young, M. A.; Jayaram, B.; Beveridge, D. L., Local dielectric environment of B-DNA in solution: Results from a 14 ns molecular dynamics trajectory. *Journal of Physical Chemistry B* **1998**, *102*, 7666-7669.
- (197) Yang, L. Q.; Weerasinghe, S.; Smith, P. E.; Pettitt, B. M., Dielectric Response of Triplex DNA in Ionic Solution From Simulations. *Biophysical Journal* **1995**, *69*, 1519-1527.
- (198) Jin, R.; Breslauer, K. J., Characterization of the Minor Groove Environment in a Drug DNA Complex - Bisbenzimidazole Bound to the Poly D(AT). Poly D(AT) Duplex. *Proceedings of the National Academy of Sciences of the United States of America* **1988**, *85*, 8939-8942.
- (199) Barawkar, D. A.; Ganesh, K. N., Fluorescent D(CGCGAATTCGCG) - Characterization of Major Groove Polarity and Study of Minor-Groove Interactions Through a Major Groove Semantophore Conjugate. *Nucleic Acids Research* **1995**, *23*, 159-164.
- (200) Savelyev, A., Do monovalent mobile ions affect DNA's flexibility at high salt content? *Physical Chemistry Chemical Physics* **2012**, *14*, 2250-2254.
- (201) Baumann, C. G.; Smith, S. B.; Bloomfield, V. A.; Bustamante, C., Ionic effects on the elasticity of single DNA molecules. *Proceedings of the National Academy of Sciences of the United States of America* **1997**, *94*, 6185-6190.
- (202) Arscott, P. G.; Ma, C. L.; Wenner, J. R.; Bloomfield, V. A., DNA Condensation by Cobalt Hexamine(III) in Alcohol-Water Mixtures - Dielectric-Constant and Other Solvent Effects. *Biopolymers* **1995**, *36*, 345-364.
- (203) Mel'nikov, S. M.; Khan, M. O.; Lindman, B.; Jonsson, B., Phase behavior of single DNA in mixed solvents. *Journal of the American Chemical Society* **1999**, *121*, 1130-1136.

- (204) Wang, Y. W.; Ran, S. Y.; Man, B. Y.; Yang, G. C., Ethanol induces condensation of single DNA molecules. *Soft Matter* **2011**, *7*, 4425-4434.
- (205) Ainalem, M. L.; Carnerup, A. M.; Janiak, J.; Alfredsson, V.; Nylander, T.; Schillen, K., Condensing DNA with poly(amido amine) dendrimers of different generations: means of controlling aggregate morphology. *Soft Matter* **2009**, *5*, 2310-2320.
- (206) Sackett, D. L.; Wolff, J., Nile Red As a Polarity-Sensitive Fluorescent-Probe of Hydrophobic Protein Surfaces. *Analytical Biochemistry* **1987**, *167*, 228-234.
- (207) Yadav, A. R.; Sriram, R.; Carter, J. A.; Miller, B. L., Comparative study of solution-phase and vapor-phase deposition of aminosilanes on silicon dioxide surfaces. *Materials Science & Engineering C-Materials for Biological Applications* **2014**, *35*, 283-290.
- (208) Faas, F. G. A.; Rieger, B.; van Vliet, L. J.; Cherny, D. I., DNA Deformations near Charged Surfaces: Electron and Atomic Force Microscopy Views. *Biophysical Journal* **2009**, *97*, 1148- 1157.
- (209) Osland, A.; Kleppe, K., Polyamine Induced Aggregation of DNA. *Nucleic Acids Research* **1977**, *4*, 685-695.
- (210) Raspaud, E.; de la Cruz, M. O.; Sikorav, J. L.; Livolant, F., Precipitation of DNA by polyamines: A polyelectrolyte behavior. *Biophysical Journal* **1998**, *74*, 381-393.
- (211) Li, Z.; Kumarasinghe, R.; Collinson, M. M.; Higgins, D. A., Probing the Local Dielectric Constant of Plasmid DNA in Solution and Adsorbed on Chemically Graded Aminosilane Surfaces. *J. Phys. Chem. B* **2018**, *122*, 2307-2313.